

GRAVITY TESTS, DIFFERENTIAL ACCELEROMETRY AND
INTERLEAVED CLOCKS WITH COLD ATOM
INTERFEROMETERS

A DISSERTATION
SUBMITTED TO THE DEPARTMENT OF PHYSICS
AND THE COMMITTEE ON GRADUATE STUDIES
OF STANFORD UNIVERSITY
IN PARTIAL FULFILLMENT OF THE REQUIREMENTS
FOR THE DEGREE OF
DOCTOR OF PHILOSOPHY

Grant Biedermann
November 2007

© Copyright by Grant Biedermann 2008

All Rights Reserved

I certify that I have read this dissertation and that, in my opinion, it is fully adequate in scope and quality as a dissertation for the degree of Doctor of Philosophy.

(Mark Kasevich) Principal Adviser

I certify that I have read this dissertation and that, in my opinion, it is fully adequate in scope and quality as a dissertation for the degree of Doctor of Philosophy.

(Savas Dimopoulos)

I certify that I have read this dissertation and that, in my opinion, it is fully adequate in scope and quality as a dissertation for the degree of Doctor of Philosophy.

(Stephen Harris)

Approved for the University Committee on Graduate Studies.

For my family,
both near and far.

Abstract

The remarkable success of light-pulse atom interferometer techniques has motivated competitive research in precision metrology. Gravimeters, gyroscopes and gradiometers based on these techniques are all at the forefront of their respective measurement classes. We show here the progress toward a compact gravity gradiometer for precision gravitational tests. It is well known that these devices suffer from environmental perturbations. Spurious noise may enter through beam steering effects which cause uncommon coupling to gravity in the two accelerometers. The horizontal configuration used here is particularly sensitive to this effect. Additionally, laser frequency noise may significantly limit the interferometer sensitivity. In our device, we have overcome these obstacles to achieve a differential acceleration sensitivity of $4.2 \times 10^{-9} g/\sqrt{Hz}$ over a 70 cm baseline. This corresponds to a phase noise of 3.1 mrad/ \sqrt{Hz} inferred per interferometer which is the best performance achieved in such a system. Using this device, we demonstrate a proof-of-concept measurement of the gravitational constant with a precision of 3×10^{-4} , which is competitive with the present limit of 1×10^{-4} . I discuss improvements which can enable uncertainties falling below 10^{-5} . This experiment can also be interpreted as a test of the inverse square law which statistically constrains a putative Yukawa type fifth force to 8×10^{-3} near the poorly known length scale of 20 cm. Limits exceeding 10^{-4} appear to be feasible. We also perform an experiment which tests the atom interferometer in the context of a time-dependent gravity potential. Furthermore, we demonstrate a technique by which one may temporally link interferometer measurements together to provide continuous sampling. This can be used to eliminate the inertial sensor analog of the Dick effect and has important applications in the fields of optical and atomic clocks.

Acknowledgements

The success of this venture is the result of the remarkable effort of many people. Their concerted efforts clearly underpin my thesis and I therefore endeavor to acknowledge them here in an abridged chronology. This project began at Yale, where it remained for more than a year before migrating to Stanford in the Fall of 2002. At Yale, Kai Bongs initiated the design and development of the first incarnations of the laser systems and all-glass vacuum cell assemblies. Shortly thereafter, Jessie Petricka and I began contributing to the development of the first master and amplifier laser frames while Wei Li invested countless hours developing code for controlling the experiment with a digital signal processor. Later, Todd Kawakami began developing the platform control and ground vehicle for mobilizing the gradiometer. While still at Yale, Brent Young joined the team as project manager, focusing his expertise on the development of the electronic control systems, including the design of many custom PCB's.

Upon arrival at Stanford, we welcomed the addition of many new faces. Matt Cashen developed the inertial sensor units, including the final design of the Zero-dur vacuum assembly and sensor optomechanics. Todd Gustavson developed the gradiometer control software, an elegant graphical interface for the many system controls, settings and data extraction options. Ken Takase reworked the master laser frame to include new features creating a fountain and generating the Raman laser. Jie Deng and Xian Wu helped profusely with the design and fabrication of many circuit boards. Todd Kawakami was joined by Chetan Mahadeswaraswamy to create a fully operational, servo-controlled leveling platform. Larry Novak patiently lent his knowledge of assembly technique to both the laser frames as well as the ground vehicle system. Paul Bayer masterfully built over ten glass vacuum chambers as well

as innumerable odds and ends with the utmost precision. And throughout this effort, Karlheinz Merkle, John Kirk, Mehmet Solyali and Matthew Chuck of the Varian machine shop shared their good vibes and sage advice, always working with us to complete jobs on ridiculously short notice. Along the way, Matt Cashen and Jeff Fixler lead the synthesis and testing of the first prototype gradiometer system using our new designs. In parallel, Ken and Xianan labored with me to complete a duplicate gradiometer for independent testing and experiments. After this intense development cycle, I was joined by Xianan Wu and later Louis Deslauriers and Sean Roy to rework the gradiometer and ultimately improve the performance by a factor of 40.

I am undoubtedly grateful to my advisor Prof. Mark Kasevich for his can-do attitude, sense of humor and command of experimental physics. I am privileged to have worked closely with Kai Bongs, Brent Young, Matt Cashen, Jeff Fixler and Todd Gustavson early in my career. I am also indebted to Louis Deslauriers and Xianan Wu for endless hours of fascinating discussions and the shared thrill of investigation. This work was supported by NGA, DARPA, ONR and AFRL. And I was supported by great family and friends who mean the world: Glenn, Betty, Tracie, Anson, Dave, Ryan, Lailah, Josh, Mooney, Davidson, Paul, Clayton, Gonz, Lambert, Ron, MacCarthy and Jo.

Contents

Abstract	vi
Acknowledgements	vii
1 Introduction	1
1.1 Gravity gradiometry	1
1.1.1 Applications	4
1.1.2 Gradiometer instrumentation	5
1.1.3 Comparison with atom interferometry	7
1.2 Inertial sensors based on atom interferometry	9
1.2.1 Brief history of cold atoms	10
1.2.2 Scientific applications	11
2 Measurement overview	14
2.1 Cesium as a proof mass	15
2.2 Cold atom sample preparation	16
2.3 Accelerometer sequence	17
2.4 Detection	19
3 Atom interferometer theory	21
3.1 Stimulated Raman transitions	21
3.1.1 Raman transitions	22
3.1.2 Beam geometry	25
3.1.3 Light-pulse interferometry in a fountain	27

3.2	Interferometer phase shift	29
3.2.1	Laser phase	29
3.2.2	Path phase	30
3.2.3	Separation phase	31
3.3	Gravity gradients and rotations	31
3.3.1	Gradients in a gravimeter	33
3.3.2	Rotations and gradients in a gravimeter	34
3.3.3	Corrections for a gradiometer	35
3.4	Phase shift from a time-dependent potential	35
3.5	Raman beam steering	38
3.6	Enhanced sensitivity	39
4	Apparatus	42
4.1	Cold atom fountain	43
4.2	Portable atom interferometer system	47
4.2.1	Laser control system	48
4.2.2	Inertial sensor	54
4.2.3	Ground vehicle platform	61
4.3	Low-noise Raman interrogation system	62
4.3.1	Raman laser system	62
4.3.2	High contrast requirements	64
5	Data Extraction	67
5.1	Low-noise detection technique	67
5.1.1	Detection scheme	68
5.1.2	System performance	72
5.2	Gradiometer sensitivity	74
5.2.1	Current performance	75
5.2.2	Noise Discussion	77
6	Gravity tests	81
6.1	Testing gravity with an atom interferometer	81

6.1.1	The gravitational constant	81
6.1.2	Testing the inverse square law	89
6.2	Time-dependent potential	94
6.3	Baseline measurement	96
6.4	Tilt sensitivity	98
6.5	SNR discussion	99
7	Zero-dead-time technique	104
7.1	Dick effect	105
7.2	Interleaved clock	107
7.3	Demonstration	109
8	Conclusion	113
A	Characteristic data	114
B	Control system photographs	116
	Bibliography	120

List of Tables

3.1	Gravimeter phase shifts from gradients	33
3.2	Gravimeter phase shifts from gradients and rotations	34
3.3	Gradiometer phase shifts	35
3.4	Gradiometer phase shifts with an interior source mass	36
3.5	Gradiometer phase shifts from a time-dependent potential	37
A.1	Useful constants and relevant Cesium parameters	114

List of Figures

1.1	Gravity gradient approximation	1
1.2	Classical acceleration measurement analogy	8
1.3	Classical gradient measurement analogy	9
2.1	3-step cycle overview	15
2.2	Cesium energy level diagram	16
2.3	Raman transition energy level diagram	18
2.4	Interferometer recoil diagram	19
2.5	Detection diagram	20
3.1	Raman transition energy level diagram	22
3.2	Doppler sensitive Raman beam geometry	26
3.3	Spatial effect of Raman transitions	28
3.4	Fountain recoil diagram	30
3.5	Raman beam steering between sensors	38
3.6	Large momentum transfer scheme	40
4.1	Gradiometer system photo	42
4.2	Cesium energy level diagram	43
4.3	Hybrid optical pumping scheme	46
4.4	Portable atom interferometer system	48
4.5	Control system overview	49
4.6	Laser lock schematic	51
4.7	Laser trapping system schematic	52

4.8	Impact testing	53
4.9	Amplifier laser channel	54
4.10	Atom fountain diagram	55
4.11	Vacuum cell photograph	55
4.12	Vacuum cell window temperature profile	58
4.13	Comparison of drop and launch configuration	59
4.14	Raman laser system schematic	63
4.15	Frequency spectrum of Raman laser implementation	64
4.16	Raman laser delivery	64
4.17	Cloud expansion	65
4.18	Typical π -pulse frequency scan	66
5.1	Detection system setup	69
5.2	Microwave clock fringe	70
5.3	Separation beam size effect	71
5.4	Cloud CCD images during simultaneous detection	72
5.5	Differential detection noise	73
5.6	Shot-noise limited detection	74
5.7	Typical interferometer output	75
5.8	Example of ellipse-based phase determination	76
5.9	Optimal points per ellipse	77
5.10	Analysis of short term noise	78
5.11	Analysis of phase stability	79
5.12	Comparison of key noise sources	80
6.1	Mass-sensor configuration for gravity measurements	83
6.2	Mass chop gradiometer phase	84
6.3	Mass chop Allan deviation	85
6.4	Floor tilt with source mass position	86
6.5	Gradiometer phase versus source mass position	88
6.6	Statistical Yukawa constraint	91
6.7	Proposed mass-sensor configuration for an improved ISL test	93

6.8	Dynamic potential timing sequence	94
6.9	Gradiometer response to a time-dependent potential	95
6.10	Raman laser frequency chop timing	96
6.11	Result of Raman laser frequency chop	97
6.12	Gradiometer tilt sensitivity	99
6.13	Interferometer SNR versus atom number	100
6.14	Interferometer contrast envelope	101
6.15	Contrast envelope study	102
7.1	ZDT timing sequence	107
7.2	ZDT clock fringe	108
7.3	Cumulative phase with ZDT method	110
7.4	Allan deviation of ZDT method	111
A.1	Cs level diagram with relevant laser frequencies	115
B.1	DSP frame	117
B.2	Sensor frame	117
B.3	Master electronics frame	118
B.4	Master laser frame	118
B.5	Amplifier electronics frame	119
B.6	Amplifier laser frame	119

Chapter 1

Introduction

A gravity gradiometer is typically achieved by making two simultaneous acceleration measurements at two different locations. Such a measurement approximates the spatial rate of change in the gravity field or gravity gradient. Figure 1.1 depicts such a gradiometer measurement. This gravity gradient is given by the difference between the two accelerometer values $g_x^{(1)}$ and $g_x^{(2)}$ divided by the separation distance L . The remainder of this chapter discusses the gravity gradient measurement, several of the technologies applied to this task and the various technological and scientific applications.

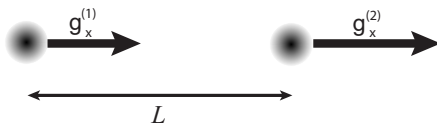


Figure 1.1: Gravity gradient approximation using two test masses separated by a distance L .

1.1 Gravity gradiometry

The following is an overview of the gravity gradient quantity along with technological applications and various instrumentation. In the Newtonian theory, gravity is a conservative force defined by the gradient of a scalar field. This scalar field can be

written as:

$$\Phi(\mathbf{r}) = -G \int \frac{\rho(\mathbf{r}')}{|\mathbf{r} - \mathbf{r}'|} dV \quad (1.1)$$

where G is the gravitational constant and ρ is the mass density. The gravitational acceleration is therefore written as:

$$\mathbf{g} = -\nabla\Phi(\mathbf{r}) \quad (1.2)$$

The gravity gradient tensor is the derivative of this vector and can be represented by a three-by-three matrix in Cartesian coordinates as follows:

$$T = \nabla\mathbf{g} = \begin{pmatrix} \partial_x g_x & \partial_y g_x & \partial_z g_x \\ \partial_x g_y & \partial_y g_y & \partial_z g_y \\ \partial_x g_z & \partial_y g_z & \partial_z g_z \end{pmatrix}. \quad (1.3)$$

This matrix has several interesting properties. At a source-free point, Laplace's equation, $\nabla^2\Phi = \rho = 0$, demands that the trace vanishes, $\sum T_{i,i} = 0$. Also, the conservative nature of the field results in symmetry among the components such that $T_{i,j} = T_{j,i}$. As a result, only five independent components exist which reduces the number of measurements required from the apparatus.

A related feature of this gradient tensor is the construction of rotationally invariant quantities. Such quantities are useful in the identification of source masses in the fields of mineral exploration and inertial navigation [1]. A common term related to our instrument is the differential curvature magnitude [2]:

$$T_c = \sqrt{4T_{x,y}^2 + (T_{y,y} - T_{x,x})^2} \quad (1.4)$$

where the azimuthal angle λ between the x-axis and the plane in which the curvature is a minimum is given by

$$\tan(2\lambda) = \frac{2T_{x,y}}{(T_{y,y} - T_{x,x})^2}. \quad (1.5)$$

This quantity tends to reverse its response between the upthrown and downthrown

sides of a fault and is therefore useful in locating them. Mathematically these quantities bear a relationship to the irreducible representations of spherical tensor components [3].

Our apparatus is constructed to measure inline gradients, $T_{i,i}$. This is advantageous as it suppresses sensitivity to angular accelerations of the platform [4] and enables cancellation of linear accelerations without loss of universality in the measurement. Several inline measurements may be combined to construct the off-diagonal quantities of the gravity gradient tensor in equation 1.3. For example, in its completed form our instrument will measure 3 planar inline quantities in a star configuration. The quantities mentioned above in equation 1.4 can be obtained according to:

$$\begin{pmatrix} T_{x,x} \\ T_{y,y} \\ T_{z,z} \end{pmatrix} = \begin{pmatrix} 1 & 0 & 0 \\ 0 & \frac{1}{\sqrt{3}} & -\frac{1}{\sqrt{3}} \\ -\frac{1}{3} & \frac{2}{3} & \frac{2}{3} \end{pmatrix} \begin{pmatrix} T_i(0) \\ T_i(\frac{\pi}{3}) \\ T_i(\frac{2\pi}{3}) \end{pmatrix} \quad (1.6)$$

where $T_i(\theta)$ is an inline measurement in the x-y plane at angle θ from the x-axis. A general expression can also be found for any arbitrary inline measurement along a direction in spherical coordinates defined by the polar angle ϕ and azimuthal angle θ according to:

$$\begin{aligned} T_{\theta,\phi}^{inline} = & T_{x,x} (\cos^2 \theta \sin^2 \phi - \cos^2 \phi) \\ & + T_{y,y} (\sin^2 \theta \sin^2 \phi - \cos^2 \phi) \\ & - T_{x,y} \sin 2\theta \sin^2 \phi \\ & + T_{x,z} \cos \theta \sin 2\phi \\ & - T_{y,z} \sin \theta \sin 2\phi. \end{aligned} \quad (1.7)$$

And one can then construct a combination of several measurements to arrive at the desired component. A tetrahedral configuration may be used to achieve this measurement with minimal sensors. In this case the sensors would be located at the vertices of a tetrahedron and be designed to have multiple sense-axes along the lines connecting the sensors. This would therefore create a gradiometer instrument with full-tensor measurement capability using only four multi-axis accelerometers.

1.1.1 Applications

Baron Roland von Eötvös, a Hungarian physicist, invented the first gradiometer in 1886. Based on a torsion balance design, this instrument was capable of a resolution of under 10^{-9} m/s² over a 1 m baseline¹. Although this sensitivity is comparable to the present state of the art, the instrument suffered from significant thermal drifts and required several hours to complete one measurement [5]. Nevertheless, this instrument found success in both fundamental research and geologic exploration.

Eötvös used the instrument to complete early tests comparing gravitational and inertial mass [6, 7, 8]. The results of this work were the first to indicate with appreciable accuracy the equivalence of the two quantities and lead to the modern understanding of the weak equivalence principle. Concurrently, early field tests of this device demonstrated its ability to accurately measure geologic gradients which inspired applications in locating salt domes associated with oil deposits [9]. This technology was introduced in the United States after World War I and is credited with the discovery of the Nash Dome in Texas in 1924, the first domestic oil discovery by geophysical means. Over the next ten years the instrument lead to the production of more than 1 billion barrels of oil [9], an average of 0.27 million barrels per day. It is interesting to compare this to the 2005 U.S. production trends of 7.61 million barrels per day and the 2004 consumption of 20.73 million barrels per day [10]. Eventually, this field use of early gradiometers was superseded by the readily interpretable and easy to use gravity meter or gravimeter [11]. This coupled with seismic methods became the industry standard over the course of the 1930's. A gradiometer's inherent immunity to platform accelerations ushered in a resurgence of interest in the 1960's. Current applications include airborne surveys for mineral exploration and precision inertial navigation.

In resource exploration, density variations in the subsurface materials cause localized gravitational anomalies. The curvature of these anomalies can be mapped using high-precision gravity gradiometers [12]. The inversion of this information is a challenging problem which is still the focus of research. Gradiometers have been used

¹In the field of gradiometry the common unit of measure is the Eötvös or E which is defined as $10^{-9}/\text{s}^2$

to detect the presence of Kimberlite pipes which are usually associated with diamond caches [13].

A closely related device, the gravimeter, finds widespread use in geodetic applications. For example, satellite based gravimeters on the GRACE project have successfully resolved high order spherical harmonic components of the earth's geoid or departure from a spherical shape. Temporal variations in this data over many months can detect changes in the water storage of large drainage basins such as the Mississippi.

Another area of intense applied interest is inertial navigation. Precision measurements of accelerations and rotations allow one to navigate without external input for limited periods of time. A hybrid solution is to combine GPS with an onboard inertial motion system which acts as a 'fly-wheel' in GPS dead zones. This is especially suited for urban situations where GPS is often shadowed. At the extreme, GPS has long been recognized to be easily susceptible to jamming, so efforts continue to focus on an all inertial sensor solution. Additionally, an all inertial solution would allow submarine navigation to be accomplished covertly by eliminating sonar readings. Developing a response to this problem is multifaceted, requiring collaborative efforts to design stabilized measurement platforms, provide advanced forward modeling and exceptional engineering of the inertial sensor systems. Recently, it has been shown that common gravity anomalies from geologic structures give rise to significant navigation errors undetectable by accelerometers [14]. It is therefore desirable to simultaneously supplement accelerometers with gravity gradient measurements which are intrinsically immune to platform accelerations and can determine the field through which one is navigating.

1.1.2 Gradiometer instrumentation

Currently, the most successful commercial gradiometer in this measurement class is the UGM developed by Bell and later by Lockheed Martin. It consists of mechanical accelerometers on a rotating disk with its angular velocity Ω_{disk} chosen in a section of frequency space having low measurement noise. The repetitive spatial interchange

allows corrections for the independent drifts of the two accelerometers.

Three such disks comprise a full-tensor measuring device and a host of sophisticated electronics effectively reduces noise due to bias instabilities and scale factor drifts [15]. Depending on the platform conditions, sensitivities in the range of 2-20 E/ \sqrt{Hz} have been achieved and the accuracy is reported to be 10 E. However, as is often the case, data collection techniques allow for improved performance by repeatedly returning the device to a reference location.

Ground based surveys with these devices are painfully slow averaging one point in about 30 minutes. This sensor has been used to map subsurface anomalies [12] as well as aid inertial navigation on board a Trident class submarine [16]. BHP Billiton has developed a small fleet of airborne sensors using this machine. These aircraft are used for expedited surveys to search for near-surface structures indicative of mineral deposits. Recent success has been reported with a helicopter version capable of 1.4 E in a 0.18 Hz bandwidth [13].

The most sensitive gradiometer technology by far is the superconducting gradiometer. With a reported sensitivity of 0.02 E/ \sqrt{Hz} this device is planned to be used as a test of Newton's inverse square law in space [17] and terrestrial tests have already been accomplished [18]. The superconducting accelerometer is a spring type accelerometer where the mechanical spring is replaced by magnetic levitation of a superconducting sphere. Persistent current coils create the magnetic field and displacements are measured with the induced changes in these currents which are output through a SQUID amplifier [19, 20]. A superconducting gradiometer is formed from this sensor by coupling the SQUID's of two masses, thereby rejecting common-mode accelerations. Aside from the necessity of cryogenic equipment, this technology suffers from 1/f noise which inhibits long term averaging [21].

Finally, it is interesting to consider the high-precision gravimeter based on the falling corner cube method [22]. In this device, an optical interferometer is used to measure the position of a falling reflector. This reflector is one arm of a Michelson interferometer and many fringes are witnessed as the reflector falls and therefore chirps this signal. The chirp is then proportional to the local acceleration. The laser used in this measurement is stabilized to an Iodine reference to set the absolute length scale.

The reference optics of these devices must be stabilized in order to avoid spurious signals due to background seismic vibrations. This is usually accomplished with an active, long period super spring. Test sites have been established in places such as the BIPM, which serve to compare devices in order to standardize gravimetry. This technique routinely demonstrates precisions at the $10^{-9}g$ level. However, a gradiometer based on this technique reports a sensitivity of only $400 \text{ E}/\sqrt{\text{Hz}}$ [23].

1.1.3 Comparison with atom interferometry

To compare atom interferometry with existing technology we consider first a simple model which encapsulates much of the behavior exhibited by the measurement process. In doing so, we neglect several important nuances such as the effect of magnetic fields, large local gradients in gravity, wavepacket overlap and rotations. A gravity gradient measurement is performed by making two simultaneous acceleration measurements with a distance separation between them. It is therefore sufficient for now to consider the process involved in only one accelerometer. In the case of a constant acceleration, one needs only to measure the position of a test mass at three points in time to arrive at the curvature in its path. For an atom probed by a coherent optical field, the three measurements can be accomplished using the optical phase fronts as the tick marks of a ruler by which these positions are measured (see Fig 1.2). If this optical phase is referenced to a stable frame, then the final quantity reveals the acceleration of the atom with respect to that frame along the direction defined by the light propagation. This measurement is made possible by the dynamics of the light-atom interaction, by which the phase of the atom's wavefunction is defined by the phase of the light field. To complete the model, one must allow the algebra of the atomic phase accrual to proceed as follows: $\Delta\phi = \phi_1 - 2\phi_2 + \phi_3$. Where ϕ_i indicates the phase of the i^{th} pulse. The acceleration is then defined by: $\Delta\phi = \mathbf{a} \cdot \mathbf{k}_{eff} T^2$ where \mathbf{k}_{eff} is the wavevector of the optical field and T is the time between evenly spaced successive pulses. For modest values of these parameters one can easily obtain sensitivities at the level of $1 \times 10^{-9} \text{ g}$ within one second of measurement time [24].

However, all acceleration measurements must obey the Equivalence Principle,

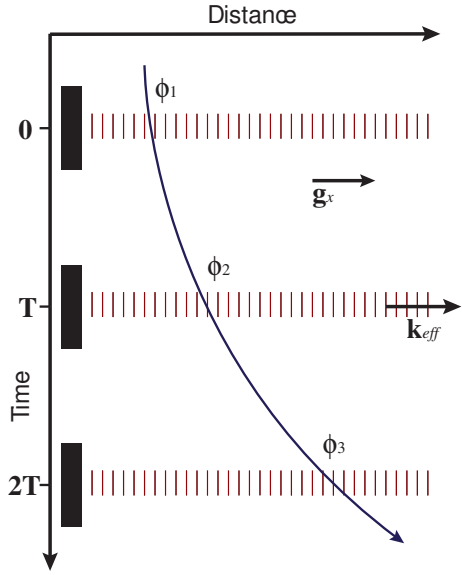


Figure 1.2: Three-pulse stroboscopic acceleration measurement. The object's position is measured along the direction defined by \mathbf{k}_{eff} as a function of time. Three points define the curvature of the path which is proportional to the acceleration. In this analogy, the ruler marks are represented by optical wavefronts of the light resonant with the atom.

where it is impossible to distinguish platform accelerations from the local gravity field. A common technique for combating this error is differencing two coupled accelerometers to arrive at a gravity gradient as is the case in our instrument (See Fig 1.3). The figure of merit for these devices is the degree of rejection of common accelerations between the two accelerometers which depends on the rigidity of their coupling. Extending the model described above to the gravity gradient case simply involves two such accelerometers sharing the same optical field (or “laser ruler”). It is clear that optically coupled accelerometers are intrinsically superior to their mechanically coupled relatives. It is simple to remove perturbations to the optical field between the sensors by evacuating the path and banning the presence of optical elements whereas mechanical systems rely on well-designed structures and material properties. In this way, gravity gradiometers based on atom interferometry offer a compelling advantage over existing technology.

Finally, the development of the laser in the early 1960’s has enabled significant

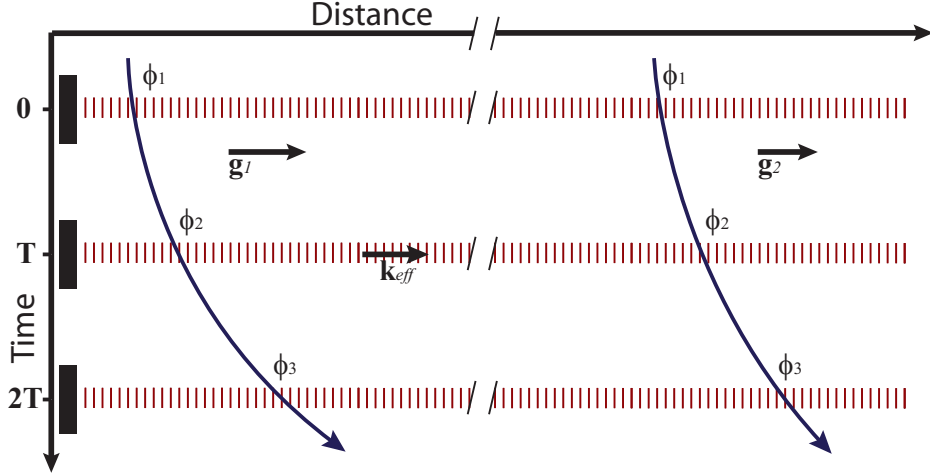


Figure 1.3: Three-pulse gravity gradient measurement analogy. Two falling atoms are simultaneously interrogated with a common beam. The optical link between the two gravimeters enables large common-mode rejection of platform accelerations.

improvements in measurement capabilities. One beneficiary of this relatively new technology is the falling corner cube gravimeter. It is notable that the measurement technique of the falling corner cube gravimeter is strikingly similar to atom interferometers in that the wavelength of the optical field sets the sensitivity scale for the displacement measurements. Despite the similarities, techniques for enhanced atom interferometer sensitivity are being actively pursued. These techniques include large momentum transfer as well as sub shot-noise limited detection using atomic entangled states.

1.2 Inertial sensors based on atom interferometry

Inertial sensors based on atom interferometry continue to demonstrate outstanding performance which competes favorably with current technology [25, 26]. The gradiometer presented herein is an improvement over previous devices and shows promise for competitive measurements of G and post-Newtonian quantities [27]. It is therefore interesting to consider recent accomplishments of atom interferometer technology as well as to anchor its brisk development in the context of growth in the general field

of cold atom physics. In this section I will briefly discuss a historical perspective of the field of cold atom physics as well as scientific applications targeted by light pulse atom interferometry.

1.2.1 Brief history of cold atoms

As a starting point, the building blocks of cold atom physics are traceable back to the scientific revolution at the beginning of the 20th century [28]. In addition to Einstein's theories of relativity, quantum mechanics was developed. Within the larger developments of quantum mechanics, Einstein pointed out that light itself is quantized and carries a unit of energy and momentum proportional to its frequency. Along with the quantized description of the atom, this idea is the basic component of modern laser cooling and trapping. Essentially, the atom is cooled and spatially confined by momentum transfer from a well defined electromagnetic field.

Other key developments followed. Townes' invention of the maser in 1954 has had an unmistakable impact as the basis for the modern laser [29]. And Ramsey's seminal experiments in 1950 with separated oscillating fields codified the main ideas of light-pulse atom interferometry [30]. Nevertheless, modern cold atom physics would have to again wait for a sequence of rapid developments which began in the 1970's with the work of A. Ashkin, V. S. Letokhov and V. G. Minogin who performed the first demonstrations of laser manipulation of atom velocities [28]. A powerful result of these developments is the magneto-optical trap (MOT) technique demonstrated by Pritchard *et al* in 1987 [31]. The MOT is an oft-employed work-horse, used as an experimental building block to achieve large ensembles cold atoms (typically $\sim 10^9$ atoms at a few μK). This system is ideal for metrology since generally, the atom trap is dilute such that minimal collisions with other atoms occur and Doppler frequency shifts are highly reduced due to the cold temperature.

Laser-atom manipulation techniques are applied to many concurrent fields of research such as Bose-Einstein condensation research [32], atom clocks [33] and atom interferometers [24] to name a few. The rich fields of atom optics and cavity QED

[34] also spring from cold atom developments. The high concentration of skilled professionals and the availability of technology have contributed to the rapid expansion of these fields and the related techniques allow for cross pollination. Therefore, more than a century after the beginnings of quantum mechanics, inertial sensors based on atom interferometry find themselves at the forefront of precision measurement technology and poised for growth due to firm roots in a variety of developing fields.

1.2.2 Scientific applications

By the nature of their measured quantities, inertial sensors based atom interferometry find scientific applications primarily in gravitational physics. This includes tests of Newtonian physics, the equivalence principle and eventually general relativity. In the near term, significant contributions will be seen in measurements of the gravitational constant. The 2006 CODATA values G at $6.674\ 28(67) \times 10^{-11} m^3 kg^{-1} s^{-2}$, meager 10^{-4} [35]. This represents an increase in precision of only one order of magnitude per 100 years since the first measurements of G by Cavendish in 1798 [36]. The slow rate of progress is representative of the weakness of the gravitational coupling and the lack of screening possibilities available with other forces. These experiments have proved to be quite difficult. High accuracy measurements following the first CODATA adjustment in 1986 disagreed with each other at the 10^{-3} level though their accuracies exceeded the 100 ppm level [37]. As a result, the CODATA precision for G was readjusted to 1500 ppm in 1998 [38] or twelve times larger than the 1986 value [39]. New understandings of systematic shifts in these measurements [40] and subsequent precision measurements have lead to the improved precision on G in 2006. Atom interferometry offers a compelling contribution to these measurements with a forecast precision near 10^{-5} . This independent evaluation of G should prove useful in determining the true value of G with greater accuracy.

There are questions as to the dependence of G on various parameters such as time, composition, temperature and distance. Work is underway to test the Weak Equivalence Principle by measuring the different acceleration of the atoms in a dual atomic species fountain [27]. There also exist a myriad of theories which predict

departures from the Inverse Square Law (ISL) model just below the resolution of current experiments. If this putative new force is mediated by a massive particle, it will exhibit a characteristic range of $\lambda = \hbar/m_\gamma c$ and follow a Yukawa potential of the form:

$$U(r) = \frac{Gm}{r^2} \left(1 + \alpha e^{-r/\lambda} \right), \quad (1.8)$$

where α is indicative of the coupling strength. Of course, not all theories for ISL breakdown result in a potential of this form, but for historical reasons, it is common to compare all experimental ISL data according to this metric [41]. If a departure is found, it then becomes a question of the actual functional form. The recent status on the constraints of these parameters can be found in [42, 43]. The work presented here indicates that atom interferometry offers the possibility to constrain α near the 10 ppm level for $\lambda > 10$ cm which represents a potential improvement of 10^2 over current limits.

Another interesting application of this type of gravity gradiometer is tests of General Relativity. Future experiments may employ large baseline gradiometers to detect gravity waves with a particular sensitivity to frequencies of $\sim \frac{1}{T}$ [44], where T is the interrogation time of the interferometer. In space, T may be quite large such that this frequency is outside the bandwidth of major detection projects such as LIGO. This therefore represents a compelling research direction. In fact, gravity wave generating collisions between astrophysical bodies exhibit a frequency chirp as they spiral inward. Therefore, a low frequency detector would represent an early warning system for gravity wave events.

Corrections to the phase shift due to General Relativity, however, are extremely small and fall below the current noise floor of our apparatus. Nevertheless, theoretical studies exploring these signals can be found in the works of [27, 45, 46]. In summary of [27], the motion of the atoms and photons are governed by a Schwarzschild space-time. In the parametrized post-Newtonian expansion the force on the atom can be represented by

$$\frac{d\mathbf{v}}{dt} = -\nabla \left[\phi + (\beta + \gamma)\phi^2 \right] + \gamma \left[3(\mathbf{v} \cdot \hat{\mathbf{r}})^2 - 2\mathbf{v}^2 \right] \nabla \phi + 2\mathbf{v}(\mathbf{v} \cdot \nabla \phi), \quad (1.9)$$

where $\phi = -\frac{Gm}{r}$. The $\nabla\phi^2$ term represents a source of gravitation in the curvature of the field itself and therefore has a nonzero divergence. The velocity-dependent $v^2\nabla\phi$ terms represent gravitation of the atom's kinetic energy. These two classes of terms are the leading General Relativity corrections and both are calculated to be at the $10^{-15}g$ level or 4 orders of magnitude below the demonstrated resolution of the gradiometer presented in this thesis. However, the current noise floor is not fundamental and the addition of long interrogation times and large momentum transfer atom optics could pave the way for this class of measurement.

Chapter 2

Measurement overview

This chapter presents an overview of a measurement cycle to give the reader a high-level perspective for the type of atom interferometer used in this work. The cycle consists of three main parts which include the (1) state preparation, the (2) acceleration measurement sequence and the (3) detection of the acceleration (Fig. 2.1). The state preparation collects and launches a small 4 mm diameter cloud of Cesium atoms ($\sim 10^8$ atoms) into a vertical 6 cm parabolic trajectory known as an atomic fountain. During this free fall, the atom trajectory is interrogated stroboscopically with a resonant laser field to determine the curvature in the atom's trajectory. Following this interrogation, the atom cloud returns to the launch position, where the acceleration information (now encoded in each atom's wavefunction) is detected. This sequence is repeated at a rate of several times per second. In the following section, a description of the Cesium states relevant to this measurement are given. Each of the subsequent sections then expands on the individual steps of the aforementioned measurement sequence.

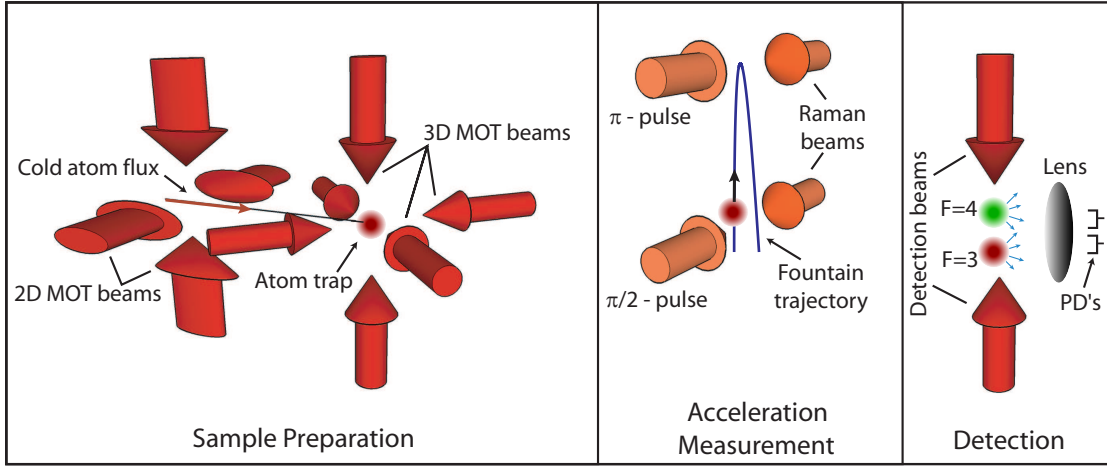


Figure 2.1: 3-Step Cycle overview. A two-dimensional magneto-optical trap (2D-MOT) loads a 3D-MOT. The atoms are then launched vertically into free-fall during which the trajectory is interrogated optically with the Raman beams. Following the interrogation, the acceleration information (now encoded in the atom’s wavefunction) is detected. This process repeats several times per second.

2.1 Cesium as a proof mass

Cesium is chosen partly due to the availability of cost-effective lasers at the required wavelength of 852 nm. Also, the mass of this atom is well defined and known to 10^{-7} [47]. In general, alkali atoms are preferred for such experiments since Hydrogen-like atoms have easily accessible dipole transitions used in laser cooling and trapping. It is interesting to note that the optimal atom for an experiment such as this would have a very short wavelength transition for high sensitivity (i.e. fine laser ruler) with a large mass to control the translations from the resultant velocity recoil.

In our apparatus we use a collection of 100 million ultra-cold Cesium (Cs) atoms in free fall. These atoms are manipulated with resonant light interactions in order to trap them, interrogate their accelerations and detect their final atomic state. A diagram of the energy level structure of the valence electron of the Cs atom is shown in figure 2.2. Two hyperfine ground states $F = 3$ and $F = 4$ are split in frequency by 9.192 GHz due to the magnetic moment interaction of the electron (\mathbf{S}) and the nucleus (\mathbf{I}). This energy splitting from this magnetic dipole-dipole interaction is proportional

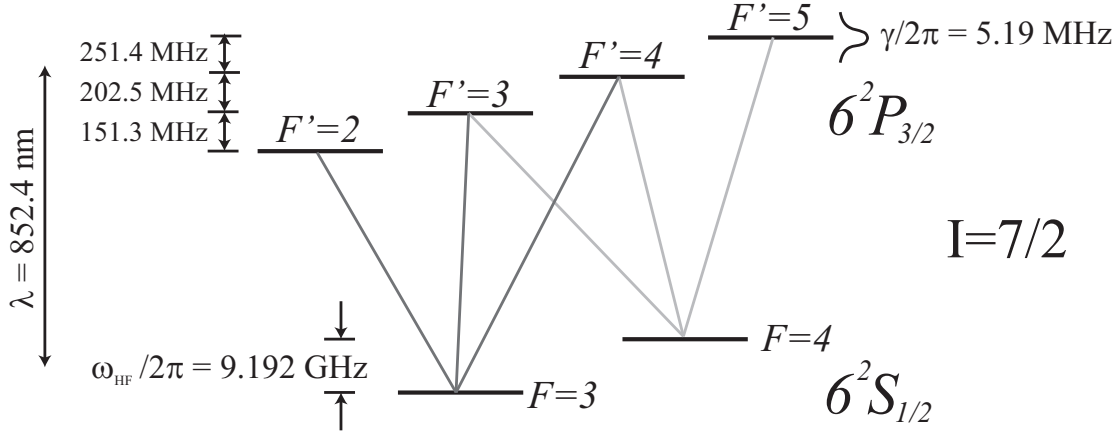


Figure 2.2: Energy level diagram for Cesium. The hyperfine structure arises largely from magnetic interactions of the electron's angular momentum with the nuclear spin, giving rise to ω_{HF} and the splitting of the $6^2P_{3/2}$ manifold. The linewidth of the 852 nm optical transition to the $F' = 5$ excited state is 5.19 MHz.

to $\mathbf{I} \cdot \mathbf{J}$, where $\mathbf{J} = \mathbf{L} + \mathbf{S}$, \mathbf{I} , \mathbf{L} and \mathbf{S} are the electron's total angular momentum, the nuclear spin, the electron's orbital angular momentum and the electron's spin respectively.

The energy splitting between the hyperfine ground states, or clock transition, is used in time keeping to define the second. Clocks using Cs, routinely employ atomic fountain techniques to launch a cold cloud of Cs atoms into a ballistic path to measure this frequency while the atom is in free fall. Our measurement process is analogous to this standard technique with the exception that the clock interrogation is replaced with optical processes effectively 7×10^4 times larger in frequency which are used to measure the curvature of each atom's path (i.e. acceleration).

2.2 Cold atom sample preparation

The sample preparation phase employs standard laser cooling and trapping techniques to produce a highly controlled atomic fountain. This fountain is the workhorse of our gradiometer measurement and the mechanics of the ubiquitous techniques involved

are presented in a subsequent chapter. Briefly, transfer of momentum from the electromagnetic field to the atom is used to trap and launch the Cs. Tuning a laser to below resonance of the $F = 4 \rightarrow F' = 5$ transition imposes a damping force which slows the atom's motion via velocity-dependent Doppler shifts, in the direction against the light. This resonance is the cycling transition, as an atom following these dynamics will continually cycle between these two states, enabling trapping and detection techniques which rely on many successive photon scattering events. However, small rates of off-resonant excitation of the atom to the $F' = 4$ state eventually depump the atom to the $F = 3$ state. Therefore a second laser tuned to the $F = 3 \rightarrow F' = 4$ resonance is present to put these atoms back in play.

Using these forces a 3D-MOT is formed, which earns its name from the combination of magnetic and optical fields used to trap the atoms to form a 3-dimensional cloud. Figure 2.1 shows the sample preparation phase of our apparatus. In our scheme, a 2D-MOT loads the 3D trap by forming a cold, pencil beam of atoms aimed at the trap using cooling in the transverse directions. This loading phase lasts for approximately 100 ms before the trapped atoms are launched upward at ≈ 1 m/s.

After the launch, the velocity distribution of the atoms in the cloud is such that the ensemble expands by less than 2 millimeters radially during the fountain time of 170 milliseconds. This is essential so that the atoms remain within the measurement laser beam and that the laser interaction is not Doppler-shifted off resonance. Another notable feature is that the cloud is dilute in the sense that very few coherence-spoiling collisions occur between the Cesium atoms during the fountain.

2.3 Accelerometer sequence

The atoms are in darkness during the fountain except for three temporally separated pulses of resonant light which interrogate the atom trajectory. In our experiment, the dominant effect of this light is to imprint the optical phase of the laser on the atomic wavefunction. The atoms can be thought of possessing a memory for the laser phase, which is stored in the phase of the atoms internal or electronic wavefunction. Therefore, the optical wavefronts can accurately be considered to be tick marks spaced by $\lambda/2$, on a ruler oriented along the light propagation direction defined by $|\mathbf{k}_{eff}| = 4\pi/\lambda$

(see Fig 1.2). In this analogy, the curvature of the atom trajectory or acceleration is given by $\mathbf{a} = (x_1 - 2x_2 + x_3) / T^2$, or in terms of the optical phase,

$$\mathbf{a} = \frac{\Delta\phi}{k_{eff}T^2} \quad (2.1)$$

where $\Delta\phi = \phi_1 - 2\phi_2 + \phi_3$.

It is clear that one desires k_{eff} to be as large as possible to maximize the measurement sensitivity. As a result, optical transitions are appealing. But if the atomic state should undergo a spontaneous decay event during the interferometer, the phase of the atom is randomized and the atom ceases to participate in the interferometer signal. In the case of Cs, the lifetime of the excited $P_{3/2}$ state is only 30.7 ns, therefore eliminating it as a possible candidate. On the other hand, the hyperfine ground states are long lived and one may use a 2-photon stimulated Raman transition between these states which meets both demands (See Fig.2.3).

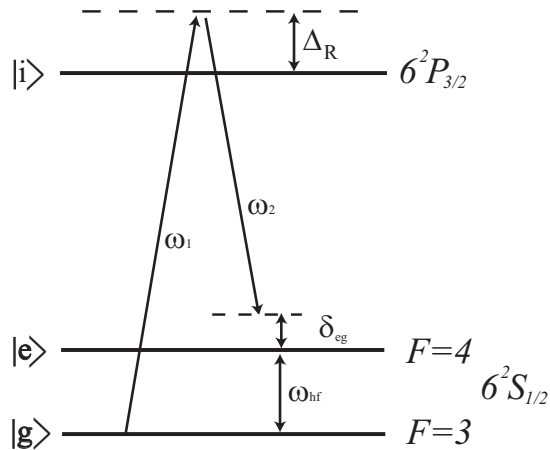


Figure 2.3: Cesium energy level diagram of relevant transitions showing the frequencies used for a 2-photon stimulated Raman transition. This transition is used to create the atom optic elements for the interferometer.

In this case, two lasers with a well defined frequency difference matching the hyperfine splitting are used to excite this transition. The optical frequencies of the two lasers are tuned far from the excited $P_{3/2}$ state resonance in order to avoid rapid spontaneous emission coupling associated with populating the excited state levels. With

a field tuned to this resonance in the prescribed way, the atom “Rabi flops” between the $F = 3$ and $F = 4$ ground states. That is to say that the probability function oscillates sinusoidally with time between these two states according to the solution to Shrödinger’s equation for a 2-level system. This behavior is used to produce beam splitters ($\pi/2$ -pulse), and mirrors (π -pulse) to construct the atom interferometer.

However, the short wavelength comes with a side effect, that of a substantial photon momentum recoil. In fact the induced velocity shift of ≈ 7 mm/s results in a path perturbation much larger than the lateral accelerations we seek to measure (See Fig. 2.4). As a result, the atomic wavepackets separate far outside their coherence length (or potential to interfere) within $7 \mu s$. Nevertheless, the measurement can be performed by 3-pulses, equally separated in time. Similar to a Mach-Zehnder interferometer configuration, these pulses serve to split, redirect and recombine the atomic wavepackets

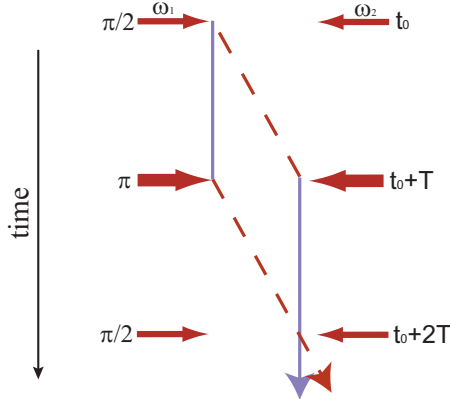


Figure 2.4: Interferometer recoil diagram showing the optical pulse sequence used to create our atom interferometer. Following the initial beam-splitter pulse, the wavepackets separate well outside their coherence length. The following pulses then redirect and recombine the wavepackets.

2.4 Detection

Following the interferometer the atoms return back to approximately the same location from which they were launched. However, now the acceleration information is

encoded in each atom's internal wavefunction phase which gives the probability of finding each atom in either of the two ground states. When considering the ensemble as a whole, this phase is revealed by the population ratio of the two ground states. In order to determine these two populations, we spatially separate the atoms according to their state and measure their numbers (see Fig. 2.5). To count the atoms, we simply count the number of photons scattered from them with resonant light as this is proportional to the population. By counting the number of atoms in both states one can construct a normalized population ratio which immunizes the result to atom number fluctuations between shots. During this thesis work, we have refined the detection technique to achieve nearly quantum projection noise limited signal-to-noise ratios of $1/\delta\phi = 3800 : 1$ [48].

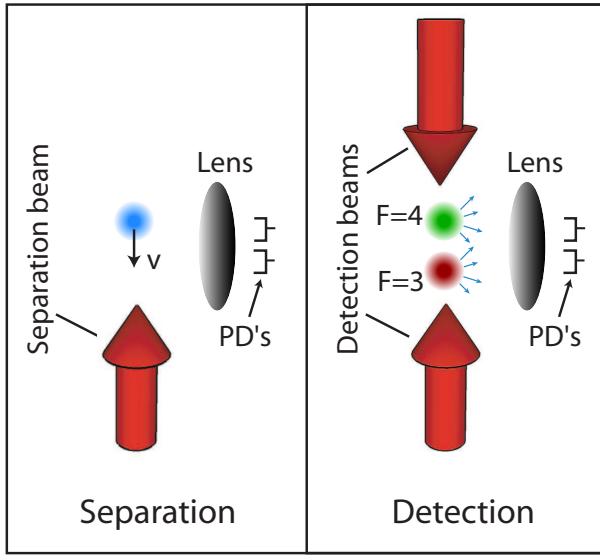


Figure 2.5: Detection sequence. A light pulse resonant with $F = 4$ atoms spatially separates the two states. Fluorescence from both states is then measured to count the atoms and determine the phase encoded in the ground state populations. This phase is proportional to the acceleration during the interrogation and emerges in the population ratio of the two hyperfine ground states $F = 3$ and $F = 4$.

Chapter 3

Atom interferometer theory

This chapter describes in more detail the atomic processes involved in the acceleration measurement. In particular, the beginning of the chapter details the Raman transition and its role in the atom interferometer. Latter sections discuss atom interferometer phase shifts in a variety of situations including large gravity gradient fields, rotations and time-dependent gravity fields. Finally, methods to enhance the interferometer sensitivity are discussed.

3.1 Stimulated Raman transitions

A two-photon, stimulated Raman transition comprises the atom optic elements in our interferometer. Briefly, the atom is irradiated by two optical frequencies with a frequency difference equal to the ground state hyperfine splitting. To avoid spontaneous emission, the single frequency detuning from the optical excited state manifold is $\approx 10^2$ larger than $1/\tau$ where τ is the excited state radiative lifetime for spontaneous emission. The following sections describe the dynamics of the Raman transition, the effects of relative beam orientation and their application to interferometry in an atomic fountain.

3.1.1 Raman transitions

There are several excellent references for the theory of 2-photon stimulated Raman transitions [49, 50, 51]. We give an overview here to arrive at the transition probability, Rabi frequency and resonance condition. The relevant spectroscopic energy levels are shown in figure 3.1. The Hamiltonian for the three level system is given by:

$$\hat{H} = \frac{\hat{p}^2}{2m} + \hbar\omega_g^A |g\rangle\langle g| + \hbar\omega_e^A |e\rangle\langle e| + \hbar\omega_i^A |i\rangle\langle i| + \hat{V}. \quad (3.1)$$

In this equation \hat{V} describes the atom-field interaction and $\hbar\omega_e^A$ is the internal energy of state $|e\rangle$. In the electric dipole approximation $\hat{V} = -e\mathbf{r} \cdot \mathbf{E}$ where:

$$\mathbf{E} = \mathbf{E}_g \cos(\mathbf{k}_g \cdot \mathbf{x} - \omega_g t + \phi_g) + \mathbf{E}_e \cos(\mathbf{k}_e \cdot \mathbf{x} - \omega_e t + \phi_e). \quad (3.2)$$

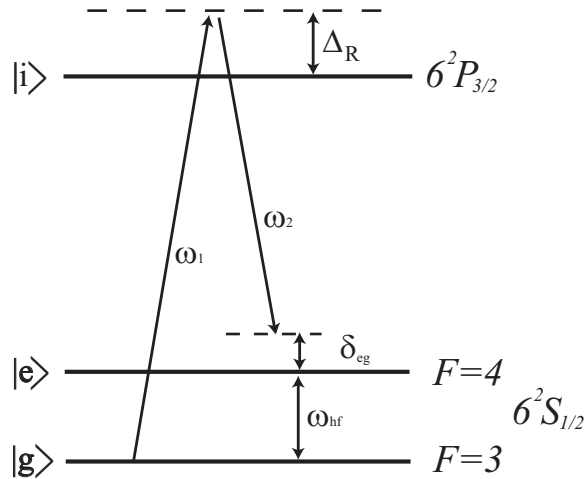


Figure 3.1: Cesium energy level diagram showing the two frequencies used to drive the Raman transition. The single-photon frequencies ω_i are detuned far from the excited state $|i\rangle$ to reduce spontaneous emission losses. The difference frequency is tuned to match the hyperfine splitting between levels $|g\rangle$ and $|e\rangle$

It is instructive to explicitly consider this system of equations. Ignoring momentum, the Schrödinger equation becomes:

$$\begin{aligned} i\hbar\dot{a}_g &= -\langle g|\mathbf{d}_{gi} \cdot \mathbf{E}_g|i\rangle a_3 \\ i\hbar\dot{a}_e &= -\langle e|\mathbf{d}_{ei} \cdot \mathbf{E}_e|i\rangle a_3 + \hbar\omega_{ge}a_e \\ i\hbar\dot{a}_i &= -\langle i|\mathbf{d}_{ig} \cdot \mathbf{E}_g|g\rangle a_g - \langle i|\mathbf{d}_{ie} \cdot \mathbf{E}_e|e\rangle a_e + \hbar\omega_{gi}a_i. \end{aligned} \quad (3.3)$$

Making the substitutions:

$$\begin{aligned} a_g &= \tilde{a}_g \\ a_e &= \tilde{a}_e e^{-i\omega_{ge}t} \\ a_i &= \tilde{a}_i e^{-i\omega_g t}, \end{aligned} \quad (3.4)$$

equation 3.3 becomes

$$i\dot{\tilde{a}}_g = -\langle g|\mathbf{d}_{gi} \cdot \mathbf{E}_g/\hbar|i\rangle \tilde{a}_3 e^{-i\omega_g t} \quad (3.5)$$

$$i\dot{\tilde{a}}_e = -\langle e|\mathbf{d}_{ei} \cdot \mathbf{E}_e/\hbar|i\rangle \tilde{a}_3 e^{-i(\omega_g - \omega_{ge})t} \quad (3.6)$$

$$i\dot{\tilde{a}}_i = -\langle i|\mathbf{d}_{ig} \cdot \mathbf{E}_g/\hbar|g\rangle \tilde{a}_g e^{i\omega_g t} - \langle i|\mathbf{d}_{ie} \cdot \mathbf{E}_e/\hbar|e\rangle \tilde{a}_e e^{-i(\omega_{ge} - \omega_g)t} + \Delta_R \tilde{a}_i, \quad (3.7)$$

where $\Delta_R \equiv \omega_{gi} - \omega_g$. Rearranging equation 3.7 we get:

$$\tilde{a}_i = \frac{\langle i|\mathbf{d}_{ig} \cdot \mathbf{E}_g/\hbar|g\rangle \tilde{a}_g e^{i\omega_g t} + \langle i|\mathbf{d}_{ie} \cdot \mathbf{E}_e/\hbar|e\rangle \tilde{a}_e e^{-i(\omega_{ge} - \omega_g)t}}{2\Delta_R}, \quad (3.8)$$

where we have made the approximation $\dot{\tilde{a}}_i \rightarrow 0$ due to the large detuning, which is commonly referred to as adiabatic elimination. Substituting equation 3.8 into equations 3.5 and 3.6 we find the dynamics reduce to that of a 2-level system with Rabi frequency inversely proportional to Δ_R given by:

$$\Omega_{eff} = \frac{\Omega_{gi}\Omega_{ie}}{2\Delta_R} \quad (3.9)$$

where, for example, Ω_{12} is the single photon Rabi frequency between state 1 and 2

defined as $\Omega_{12} = -\langle 2|\mathbf{d} \cdot \mathbf{E}|1\rangle/\hbar$. On resonance, the equations of motion have a simple solution. For a state $|\psi\rangle$ initially in the ground state $|g\rangle$,

$$|\psi(t_0 + \tau)\rangle = \cos\left(\frac{\Omega_{eff}\tau}{2}\right)|g\rangle - i\sin\left(\frac{\Omega_{eff}\tau}{2}\right)e^{i\phi}|e\rangle. \quad (3.10)$$

While for an atom initially in state $|e\rangle$,

$$|\psi(t_0 + \tau)\rangle = \cos\left(\frac{\Omega_{eff}\tau}{2}\right)|e\rangle - i\sin\left(\frac{\Omega_{eff}\tau}{2}\right)e^{-i\phi}|g\rangle. \quad (3.11)$$

In these equations, ϕ is the phase of the Raman laser field which arises from the coherent transfer of energy between the atom and the field. If the atom is initially in the ground state $|g\rangle$ then the component of the atom transferred to the excited state $|e\rangle$ picks up a phase factor $e^{i\phi}$, while the component that remains in the ground state is not affected. Similarly, if the atom is initially in the excited state, then the component that makes the transition to the ground state picks up a phase factor $e^{-i\phi}$, while the component that remains in the excited state is not affected. In this way, the atom can be thought of as having an optical phase memory of its interactions with the laser which is the source of the dominant interferometer phase shift as presented in chapter 2.

Stimulated Raman transitions then form the basic atom optic tools of the interferometer presented here. A coherent beam splitter can be formed by driving a $\pi/2$ -pulse of duration

$$\tau = \frac{\pi}{2} \frac{1}{\Omega_{eff}}, \quad (3.12)$$

while a mirror or π -pulse can be formed by doubling this time interval. In practice, single beam intensities of ~ 100 mW/cm² and $\Delta = -600$ MHz from $F' = 5$, result in a Rabi frequency of ≈ 100 kHz or π -pulse lengths of ≈ 5 μ sec. So, for a $\pi/2 - \pi - \pi/2$ interferometer pulse sequence:

$$a_e = \frac{1}{2} (e^{-i\Delta\phi} + 1), \quad (3.13)$$

where $\Delta\phi = \phi_1 - 2\phi_2 + \phi_3$ as in section 2.3.

The resonance condition is met when the difference frequency of the two fields equals the hyperfine splitting frequency ω_{hf} accounting for Doppler shifts. However, this resonance condition is sensitive to the AC Stark effect, which shifts the energy levels of the atom according to

$$U_{12}^{AC} \approx \frac{\hbar\Omega_{12}^2}{4\Delta} \quad (3.14)$$

Each of the two ground state levels is shifted in the same direction such that the differential AC Stark shift is the important quantity. Including the aforementioned effects the two-photon detuning is found to be

$$\delta_{eg} = \omega_1 - \omega_2 - \left[\omega_{hf} + \nu(k_1 - k_2) + \hbar \frac{(k_1 - k_2)^2}{2m} \right] + \Omega_{AC}. \quad (3.15)$$

This includes in order, the frequency difference of the two Raman laser beams, the hyperfine splitting, the Doppler shift of the two beams, the recoil shift from the momentum transfer of the two-photon transition and the AC Stark shift.

The AC Stark shift includes the sum of the light shifts from all frequencies that are present (in this case two).

$$\Omega_{AC} = \sum_{j=e,g} \frac{\Omega_{ji}^2}{4\Delta_{ji}} \quad (3.16)$$

A nonzero AC Stark shift can be problematic for non ideal implementations of an atom interferometer, such as those where the laser field intensity is not uniform over the spatial extent of the atom ensemble. It is therefore favorable to null the AC Stark shift by adjusting the relative intensities (Rabi frequencies) of the two beams.

3.1.2 Beam geometry

The relative orientation of the two Raman beams is important as shown below. Two typical cases are worth considering, that of copropagating and counterpropagating. In the copropagating case the interaction is considered to be “Doppler-free” in the sense that the atom’s velocity is negligible. This is due to the fact that as the atom absorbs a photon from one beam, while the other beam stimulates the emission of a photon in the same direction of absorption, leading to a negligible recoil. An advantage of

the Doppler-free configuration is that the atom sees both beams Doppler shifted by a similar amount, such that their difference frequency is unchanged regardless of the atom's velocity. However, with regard to inertial sensing, this is the least sensitive configuration of the beams. Consider an electric field of the form $\cos(\mathbf{k} \cdot \mathbf{x} - \omega t)$. The beatnote of the two fields is responsible for the interaction and is given by:

$$\mathbf{E}_{beat} \sim \cos\left(\frac{1}{2}(\Delta\mathbf{k} \cdot \mathbf{x} - \Delta\omega t)\right). \quad (3.17)$$

In this equation, $\Delta\mathbf{k} = \mathbf{k}_1 - \mathbf{k}_2$, $\Delta\omega = \omega_1 - \omega_2$ and $|\mathbf{k}_1| \approx |\mathbf{k}_2|$. The Doppler shift to the resonance condition is then given by $\Delta\mathbf{k} \cdot \mathbf{v}_{atom}$ which is at the Hz level for typical laser cooled Cs atoms with velocities of ~ 1 cm/s. For inertial sensing, this leads to a sensitivity proportional to $\Delta\mathbf{k}$ which is the same as a 9.192 GHz magnetic dipole transition between the hyperfine ground states.

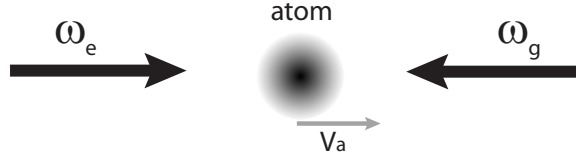


Figure 3.2: Counterpropagating beam geometry for a Doppler sensitive Raman transition. An atom in the ground state absorbs one photon from the ω_g beam and is then stimulated to emit a photon by the ω_e beam. This results in a two photon momentum recoil in the direction of ω_g leading to macroscopic spatial separations of the atom wavefunction. Doppler shifts due to the atom's velocity must be considered to meet the resonance condition.

In the counterpropagating configuration, the interaction is considered to be Doppler sensitive and the atom's velocity can no longer be ignored (see Fig. 3.2). In this case, the atom absorbs a photon from one direction and is then stimulated to emit a photon in the opposite direction, receiving a two-photon momentum kick. Therefore the atom's velocity directly influences the resonance condition. In this case $\mathbf{k}_{eff} \equiv \Delta\mathbf{k} \approx 2|\mathbf{k}|$ and the Doppler shift for the same atom with a velocity of ~ 1 cm/s would be ≈ 25 kHz. Physically, this beatnote is a traveling wave moving at $10^{-5} c$ with wavelength $\lambda/2$. This small wavelength allows high sensitivities in inertial sensing, 10^4 larger than the copropagating situation described above.

3.1.3 Light-pulse interferometry in a fountain

In a Doppler sensitive Raman transition there is an important interplay between the velocity distribution of the atoms and the Rabi frequency of the Raman pulses [50]. Simply put, the frequency spread of the Raman light seen by the atom is given by the Fourier transform of the temporal pulse envelope. In many cases, this spread is smaller than the associated Doppler profile due to the finite cloud temperature. If one considers the resonance condition of equation 3.15 coupled with the frequency distribution of the pulse it is clear that only a narrow velocity class of atoms will be resonant with the pulse when $\Omega_R \ll \Omega_D$, where Ω_D is the Doppler profile of the atom ensemble. The atoms making the transition will thus be defined by the convolution of these two envelopes.

This effect has been used in the past for generating an extremely narrow velocity profile of $270 \mu\text{m/sec}$ of atoms along one dimension [52]. In the case where the velocity of the atoms can lead to a velocity dependent phase shift such as that due to the Coriolis effect then it can be advantageous to control the atoms in this way for enhanced accuracy. Many light-pulse atom interferometer experiments use low intensity Raman beams which naturally limits the velocity range of atoms that are sensitive to the Raman pulses. This limits the interferometer fringe visibility of the atoms and adds additional noise due to the increased presence of background spectator atoms. In this case a velocity selection pulse is typically used to remove those atoms that would otherwise not participate in the interferometer due to their large velocities or Doppler shifts. In comparison, we use relatively high intensity Raman beams such that a majority of the atoms are addressed by the Raman transitions leading to fringe visibilities as high as 65% for 3-pulse interferometers. In this case, velocity selection is no longer advantageous.

Finally, it is interesting to qualitatively consider the spatial effect of a Raman pulse on an atom related to the finite pulse duration (see Fig. 3.3). Since the excited state is in a moving frame $\mathbf{p}_0 + \hbar\mathbf{k}_{eff}$, the probability distribution is spread out as the pulse proceeds by an amount $\delta x \approx \tau_p \frac{\hbar k}{m}$. In the case of $\Omega_R \ll \Omega_D$ this tends to enlarge the coherence length whereas when $\Omega_R \gg \Omega_D$ nothing is changed. Testing for the presence of this effect is one way to characterize the performance of the Raman pulses as shown in section 6.5.

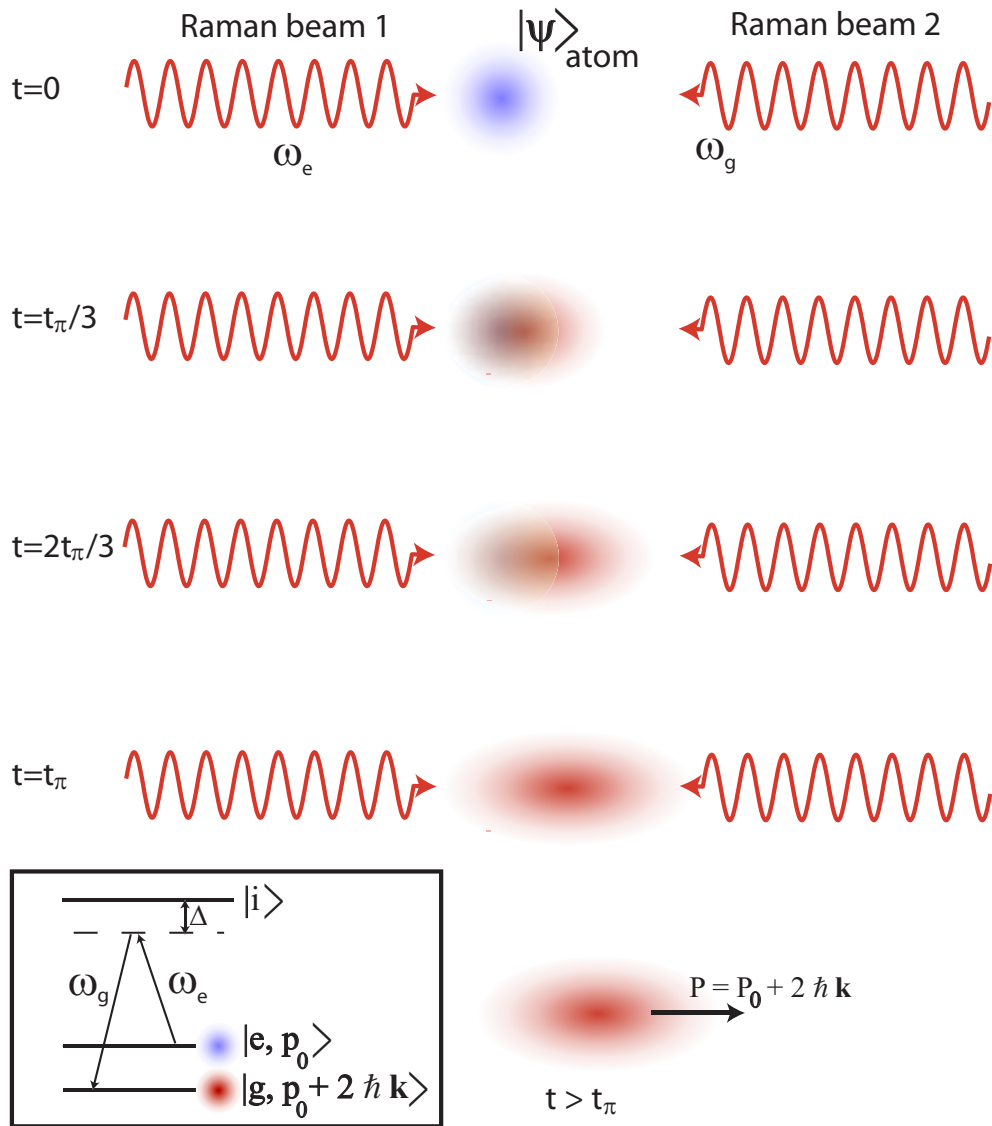


Figure 3.3: Spatial effect of a Raman transition. This qualitatively depicts the blurring of the atom probability distribution for $\Omega_R \ll \Omega_D$. The scale of this blurring is inversely related to the temperature or narrowness of the Raman velocity selection. The atom, initially in the excited state $|e, \mathbf{p}_0\rangle$, gradually absorbs energy from the ω_e -field and channels this energy through the virtual state $|i\rangle$ into the ω_g -field (see inset). This results in a 2-photon kick to the atom wavepacket.

3.2 Interferometer phase shift

There are many excellent references useful for calculating the phase shift in an atom interferometer. Here we adapt where necessary, the treatments of [49, 53] to the case of a horizontally interrogated gravimeter and gradiometer. Using the Raman transitions described above, we construct a 3 pulse Mach-Zehnder interferometer in the time domain. A $\pi/2 - \pi - \pi/2$ sequence is used to split, redirect, and combine the wavepackets as shown in figure 3.4. The figure shows the wavepacket trajectories in a fountain configuration in the presence of a non-uniform horizontal acceleration g_x . In this case the wavepackets do not perfectly overlap at the end of the interferometer and furthermore the two paths do not explore identical potentials. Therefore, to arrive at the resulting phase shift for the interferometer one must consider three contributions: the laser phase at each pulse, the atom path phase which is due to the evolution of the wavepacket between pulses, and the spatial separation phase associated with incomplete closure of the interferometer path resulting in partial wavepacket overlap.

$$\Delta\phi_{total} = \Delta\phi_{laser} + \Delta\phi_{path} + \Delta\phi_{sep}. \quad (3.18)$$

3.2.1 Laser phase

For a static, uniform field, it is straight forward to calculate the phase shift contribution of the laser pulses. In the limit of short pulses, the transition amplitudes 3.10 and 3.11 take a particularly simple form:

$$|g\rangle \rightarrow ie^{i\mathbf{k}_{eff}\cdot\mathbf{x}(t_p)-\Delta\omega t_p}|e\rangle, \quad |e\rangle \rightarrow ie^{-i\mathbf{k}_{eff}\cdot\mathbf{x}(t_p)-\Delta\omega t_p}|g\rangle, \quad (3.19)$$

where $\mathbf{x}(t_p)$ is the mean position of the wavepacket at the pulse time t_p . The phase acquired with the light interaction is as follows,

$$\Delta\phi_{total} = \phi_R(\mathbf{x}_1^1, t_1) - \phi_R(\mathbf{x}_1^2, t_2) - \phi_R(\mathbf{x}_2^2, t_2) + \phi_R(\mathbf{x}_1^3, t_3) \quad (3.20)$$

where,

$$\phi_R(\mathbf{x}, t) = \mathbf{k}_{eff} \cdot \mathbf{x}(t) - \Delta\omega t. \quad (3.21)$$

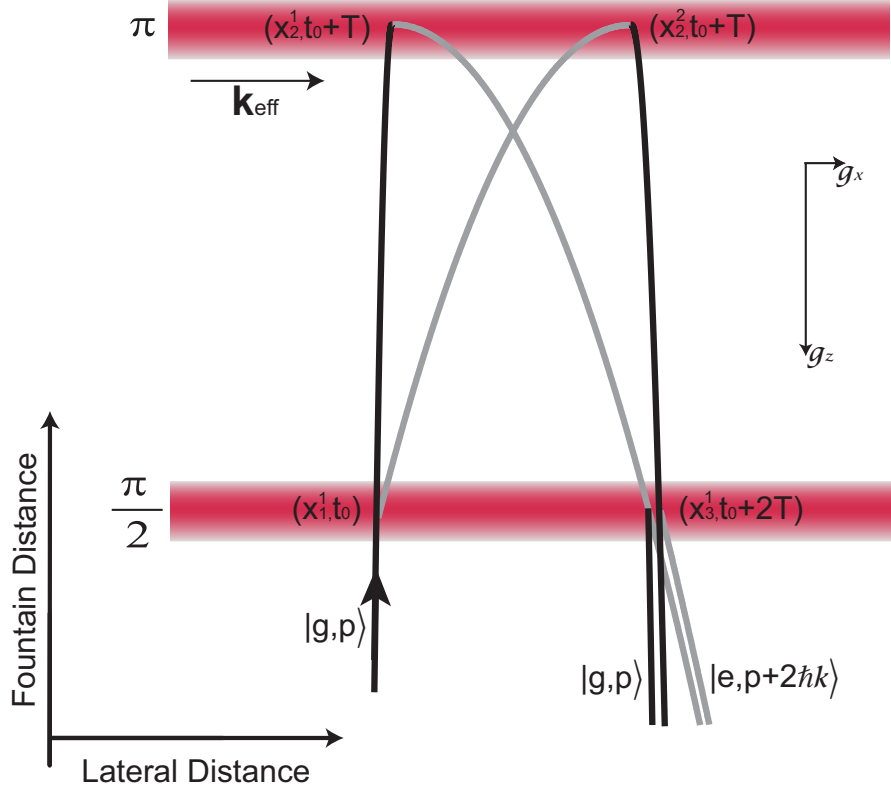


Figure 3.4: Interferometer recoil diagram in an atomic fountain with a gravity gradient.

For equally spaced pulses, the contribution from $\Delta\omega$ vanishes in the summation which simplifies to the core phase shift equation

$$\Delta\phi_{laser} = \mathbf{k}_{eff} \cdot \mathbf{a}T^2 \quad (3.22)$$

3.2.2 Path phase

The path phase comes from the free evolution of the atomic wavepackets between the pulses while in the presence of the gravitational potential. This term is obtained using the Feynman path integral approach [54]. This approach involves a calculation of the difference in the action along the two interfering paths. The classical paths are illustrated in figure 3.4. In this case the action is given by $S = \oint Ldt$ where

the Lagrangian, $L = T - V$. The integrand can be rewritten in terms of the atom wavevector and total energy to arrive at phase shift according to

$$\Delta\phi_{path} = \oint \mathbf{k}_a \cdot d\mathbf{x} - \omega_a dt \quad (3.23)$$

where \mathbf{k}_a is the atomic wavevector and ω_a is the total energy (kinetic plus potential) of the atom. For a constant and uniform gravitational field, the phase accrued due to the atom's wavevector exactly cancels the phase evolution of the atom's total energy over the closed path of the interferometer. The path integral approach is valid so long as L is at most second order dependent on position and velocity.

3.2.3 Separation phase

Finally, the separation phase shift is considered which arises when the classical positions of the wavepackets at the end of the interferometer do not perfectly overlap. An extra phase shift of

$$\Delta\phi_{sep} = \mathbf{p} \cdot \Delta\mathbf{r}/\hbar \quad (3.24)$$

is acquired where \mathbf{p} is the mean wavepacket momentum and $\Delta\mathbf{r}$ is the spatial separation. In the absence of rotations and local gradients this term vanishes.

3.3 Gravity gradient and rotations

In this section I will discuss the impact of gravity gradients and rotations on a single gravimeter phase shift in the new context of a horizontally interrogated fountain. The apparent velocity of a particle in a rotating frame can be derived by applying the following operator which relates the velocity seen by observers fixed in either the inertial frame or rotating frame [55]:

$$\left(\frac{d}{dt} \right)_{inertial} = \left(\frac{d}{dt} \right)_{particle} + \boldsymbol{\Omega} \times \quad (3.25)$$

Applying 3.25 twice we can derive the apparent acceleration on the particle:

$$\left(\frac{d^2 \mathbf{r}}{dt^2} \right)_{inertial} = \left(\frac{d^2 \mathbf{r}}{dt^2} \right)_{particle} + 2\Omega \times \mathbf{v}_{particle} + \dot{\Omega} \times \mathbf{r} + \Omega \times (\Omega \times \mathbf{r}). \quad (3.26)$$

In the rotating frame, the Lagrangian can be written as:

$$L_R = \frac{1}{2}m(\mathbf{v} + \Omega \times \mathbf{r})^2 + \mathbf{g} \cdot \mathbf{r}. \quad (3.27)$$

Simplifying the terms and including the gravity gradient tensor \mathbf{T} , the Lagrangian is finally written as:

$$L(\mathbf{r}, \mathbf{v}) = m \left(\frac{\mathbf{v}^2}{2} + \mathbf{g} \cdot \mathbf{r} + \frac{1}{2}r_i T_{ij} r_j + \Omega \cdot ((\mathbf{r} + \mathbf{R}) \times \mathbf{v}) + \frac{1}{2}(\Omega \times (\mathbf{r} + \mathbf{R}))^2 \right). \quad (3.28)$$

A common approach to calculating high order corrections to the solutions in the previous section is to analyze the contribution of gravity gradients perturbatively [56]. This approach has been validated numerically to the μrad level¹ which is sufficient for the work presented here but potentially insufficient for subsequent plans to measure G with a resolution near 10^{-5} [53]. Nevertheless, we elucidate the dynamics of the gravimeter by borrowing this technique.

In summary, the equation of motion 3.26 is integrated to obtain analytic expressions in terms of the initial conditions \mathbf{x}_0 and \mathbf{v}_0 . These solutions are Taylor expanded to sixth order and used to determine the classical paths for the phase shift contributions. The perturbed Lagrangian 3.28 is then integrated along these paths to determine the path phase contribution. Then the laser phase and separation phase are calculated at the appropriate times on this path. These three terms are added together to arrive at the total phase shift from the interferometer.

¹For the experimental parameters typically used in this gradiometer, this corresponds to roughly 10^{-12}g

3.3.1 Gradients in a gravimeter

For clarity the effect of gradients with rotations is considered separately and here we consider only gradient corrections. The highest order contributions from a gravitational gradient are given in table 3.1 for the typical experimental parameters of $T=85$ ms, $T_{yy}=100$ ng/m, $g_y = 30$ ng, $v_{rec} \approx 7$ mm/s and $v_y \approx 40\mu\text{m}/\text{s}$. In this system of coordinates, y is parallel with the Raman wavevector and z is vertical. The first and second term are typical of signals from our source mass, v_{rec} is the recoil velocity of Cs from the 2-photon stimulated Raman transition and v_y is an experimentally constrained value for horizontal velocity jitter.

Phase term	Numeric value [Rad]
$k_y g_y T^2$	3.19×10^{-2}
$\frac{1}{2} v_{rec} k_y T^3 T_{yy}$	3.17×10^{-5}
$k_y v_y T^3 T_{yy}$	3.61×10^{-7}
$\frac{7}{12} k_y g_y T^4 T_{yy}$	1.34×10^{-10}

Table 3.1: Contributions to the phase from gravity gradients for a horizontally interrogated accelerometer. The accelerometer phase shift $k_y g_y T^2$ is given as a reference. Although the accuracy of the calculation is questionable below 10^{-6} , the values of the second and third gradient correction are given for comparison with the vertical gravimeter.

The corrections shown in table 3.1 are identical to those derived for the vertical gravimeter in [57],

$$\Delta\phi_{gg} = \gamma k_z T^2 \left(\frac{7}{12} g_z T^2 - \bar{v}_0 T \right) \quad (3.29)$$

where γ is the local gravity gradient in the direction of k_z and $\bar{v}_0 \equiv v_z + \frac{1}{2}v_{rec}$ is the initial velocity of the atoms plus $\frac{1}{2}$ the photon recoil velocity. In the case of a truly horizontal measurement, the first gradient correction arises entirely from the velocity recoil due to the Raman transition which causes the separate arms of the interferometer to explore different parts of the gravitational potential. It is interesting to note that this correction is not identically obtained if one only considers the laser phase and the classical path of a point particle in a gravitational field with the proper gradient. In the latter case, the recoil velocity is not considered and the gradient

correction vanishes. In a precision measurement of the gravitational constant with this apparatus, phase systematics at the μrad level are important. This effect must then be considered since the local gradient experienced by the atoms, is a large function of the mass position.

3.3.2 Rotations and gradients in a gravimeter

The addition of rotations reveals many large interferometer phase shifts. The above method is applied in this case with the numerical parameters $\Omega_x = \Omega_y = \Omega_z = 5 \times 10^{-5} \text{ rad/s}$ which are typical of earth rotation, $R_E=6.37 \times 10^6 \text{ m}$ or the earth's radius, $g_z = -9.81 \text{ m/s}^2$ and $v_z = -g_z T$. All other parameter values are identical to the previous calculation. The results of this calculation are shown in table 3.2.

Phase term	Numeric value [Rad]
$-k_y \Omega_y \Omega_z R_E T^2$	-1.602×10^3
$2k_y \Omega_x g_z T^3$	-8.91
$2k_y \Omega_x v_z T^2$	8.91
$k_y g_y T^2$	3.19×10^{-2}
$2k_y \Omega_x^3 R_E T^3$	1.36×10^{-2}
$2k_y \Omega_x \Omega_z^2 R_E T^3$	1.36×10^{-2}
$2k_y \Omega_x \Omega_y^2 R_E T^3$	1.36×10^{-2}
$3k_y \Omega_y \Omega_z v_z T^3$	5.69×10^{-5}
$\frac{7}{4} k_y \Omega_y \Omega_z g_z T^4$	-3.32×10^{-5}
$\frac{1}{2} v_{rec} k_y T^3 T_{yy}$	3.17×10^{-5}

Table 3.2: Contributions to the phase from gravity gradients with rotations for a horizontally interrogated accelerometer. The zeroth order phase shift is given as a reference. The exact cancellation of the second and third terms is a result of the symmetry of the fountain and pulse timings. However, the identical value of the fifth through seventh is an artifact of the identical Ω_i values used in the calculation.

3.3.3 Corrections for a gradiometer

The previous calculation is largely of pedagogic value. In the case of the gravity gradiometer, all of these terms are highly suppressed as they are common to both interferometers. All, that is, except for the differential acceleration. Additionally, the extended baseline results in a new centrifugal correction. The contributions down to the $10 \mu\text{rad}$ level are shown in table 3.3 for the differential phase of an $L=1 \text{ m}$ baseline gradiometer .

Phase term	Numeric value [Rad]
$k_y T_{yy} LT^2$	1.06×10^{-1}
$k_y \Omega_x^2 LT^2$	2.66×10^{-4}
$k_y \Omega_z^2 LT^2$	2.66×10^{-4}

Table 3.3: Contributions to the gradiometer phase shift in the presence of rotations. All terms above 10^{-6} Rad are shown. These results are contingent upon the degree of cancellation of the terms shown in table 3.2 in the differential measurement.

An important case to consider, where reduced cancellation occurs, is in the presence of a nonzero divergence of the gravitational field. Such a case is produced by the presence of the large source mass between the accelerometers in our gravitation studies. In this case, both the gravitational attraction and the gradient switch sign between the sensors. However, all of the rotation terms in table 3.2 are still suppressed. The corrections for this case in the presence of rotations are given in table 3.4.

3.4 Phase shift from a time-dependent potential

An unexplored aspect of light pulse atom interferometry is the response of the measurement to a time-dependent potential. This is similar to the analysis of an interferometer with atoms falling in a field with a significant gradient. In the case of an atomic fountain gravimeter, the atom explores a vertical distance larger than 10 cm in a gradient on the order of 300 ng/m. This is a spatial modulation of the potential. Our experiment differs in that the potential is modulated in time regardless of the

Phase term	Numeric value [Rad]
$2k_y g_y T^2$	6.38×10^{-2}
$k_y \Omega_x^2 L T^2$	2.66×10^{-4}
$k_y \Omega_z^2 L T^2$	2.66×10^{-4}
$v_{rec} k_y T^3 T_{yy}$	6.34×10^{-5}

Table 3.4: Contributions to the phase for a gradiometer in the presence of rotations with a source mass between the sensors. All terms above 10^{-6} Rad are shown. This is contingent upon the degree of cancellation of the terms highlighted in table 3.2 for the differential measurement. Here the assumptions are that $T_{yy}^a = -T_{yy}^b$ and $g_y^a = -g_y^b$ for sensors a and b .

atom's trajectory. We find that in our interferometer the phase response is largely dictated by the laser phase since no gravity potential asymmetry is imposed between the two interferometer arms.

Any impact of the dynamic potential on path and separation phase shift terms are below the 10^{-6} rad level for our gradiometer. We therefore only present the contribution of the laser phase. It is convenient to parameterize the time dependent field with a polynomial expansion:

$$\mathbf{a}(t) = \sum_n \alpha_n t^n. \quad (3.30)$$

The laser phase responds according to

$$\Delta\phi_{laser} = \mathbf{k}_{eff} \cdot (\mathbf{x}_1 - 2\mathbf{x}_2 + \mathbf{x}_3), \quad (3.31)$$

which safely ignores small corrections to the two interferometer paths from gradients. In the case of a dynamic field,

$$\mathbf{x}_i = \int_0^{t_i} \int_0^{t'} \mathbf{a}(t'') dt'' dt'. \quad (3.32)$$

Therefore equation 3.31 becomes

$$\Delta\phi_{laser} = \sum_n \mathbf{k}_{eff} \cdot \frac{(2\alpha_n (2^{n+1} - 1)) T^{n+2}}{(n + 1)(n + 2)}, \quad (3.33)$$

These results are shown in the context of a horizontal gravimeter with a gravity gradient in table 3.5 for the experimental values $\alpha_0 = 30\text{ng}$, $\alpha_1 = 24\text{ ng/s}$ and $\alpha_2 = 15\text{ ng/s}^2$.

Phase term	Numeric value [Rad]
$k_y\alpha_0 T^2$	3.19×10^{-2}
$k_y\alpha_1 T^3$	2.17×10^{-3}
$\frac{7}{6}k_y\alpha_2 T^4$	1.34×10^{-4}
$\frac{1}{2}v_{reck}k_y T^3 T_{yy}$	3.17×10^{-5}

Table 3.5: Contributions to the phase for a time-dependent potential. Shown here in the context of gravity gradients without rotations for a single horizontal gravimeter. T_{yy} is taken to be the mean value at the midpoint of the interferometer since it will change at a part in ten over the interrogation.

It seems plausible that the dynamic phase shift would simply be proportional to the mean value of the field during the interrogation according to

$$\Delta\phi_{mean} = \frac{1}{2T} \int_0^{2T} \mathbf{k}_{eff} \cdot \mathbf{a}(t) T^2 dt. \quad (3.34)$$

This is approximately true, but fails to properly account for any nonlinear field dynamics. This can easily be demonstrated by calculating the behavior of 3.34 for the field given in 3.30. In this case, 3.34 becomes

$$\Delta\phi_{mean} = \sum_n \mathbf{k}_{eff} \cdot \frac{2^n \alpha_n T^{n+2}}{n + 1}. \quad (3.35)$$

So an error is produced according to

$$\Delta\phi_{laser} - \Delta\phi_{meas} = \sum_n \mathbf{k}_{eff} \cdot \frac{2\alpha_n ((2^n - 1) - n2^n) T^{n+2}}{(n + 1)(n + 2)}. \quad (3.36)$$

The largest difference is given by $-k\alpha_n T^4/6$ for $n = 2$ which amounts to a maximum $-19 \mu\text{rad}$ for our parameters which is below the resolution of our current experiment and therefore currently negligible. Section 6.2 details the related experiment.

3.5 Raman beam steering

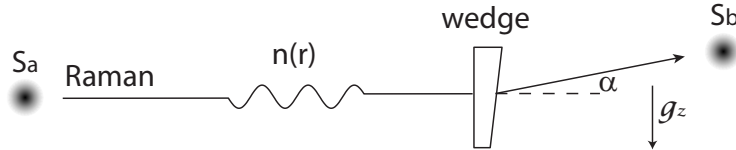


Figure 3.5: Index of refraction variations and wedges result in an angular deviation of the Raman beam between Sensors a and b . Wedging results in a differential projection of the measurement axis onto g_z giving a differential phase proportional to α . Index of refraction variations faster than T (the interrogation time) will cause shot-to-shot noise.

By design the gradiometer instrument is differential, therefore perturbations to the Raman beam between the sensors produces a differential projection onto \mathbf{g} (see Fig. 3.5). Considering the fact that $kg_z T^2 \approx 10^6$ rad is a very large signal, it is clear that beam steering at the nrad level will produce mrad interferometer phase shifts, commensurate with our noise floor. Whether these deviations can be classified as jitter or slow drifts is important for the performance of the device. Slow drifts may be corrected by monitoring the driver (usually thermal). However, jitter can limit the sensor resolution and potentially the long term averaging. As discussed in chapters 4 and 5, we have removed the dominant source of beam jitter, that being index of refraction noise between the sensors. This is accomplished by enclosing the entire system in a partial vacuum of ≈ 100 mTorr.

The slow drift terms may also be reduced by understanding the coupling mechanism. Since this horizontal gradiometer is implemented in a two-level Raman beam delivery scheme (see Fig. 4.16), it is important to distinguish here between deflections affecting only one beam or both. The leading phase shifts from a vertical deflection

of one beam in the presence of rotations are:

$$\Delta\phi \approx -\alpha k_y g_z T^2 + -2\alpha k_y v_z T + \dots \quad (3.37)$$

Additionally, this deflection reduces contrast by imprinting a phase gradient across the cloud. To achieve good contrast, the two tiers must be parallel to $\ll 10\mu\text{rad}$ which limits the magnitude of these terms ². In our system the most common cause of such a perturbation is a result of nonlinear thermal profiles across the vacuum cell windows which are discussed in section 4.2.3.

Deflecting both beams equally results in a phase shift identical to the first term in equation 3.37 yet does not reduce contrast. In our device, the dual beam deflection is due largely to the wedged windows of our vacuum cells. Deflections $\approx 100\mu\text{rad}$ have been measured, which also opens the possibility of a static sensitivity to the angular position about the Raman beam axis. This deflection also results in decreased suppression of the rotational couplings shown in table 3.2. Instead of perfectly canceling, the terms only diminish to the level of the beam steering or 10^{-4} in this case. Furthermore, on an unstable platform, this deflection can limit the gradiometer sensitivity. For example, a platform oscillating about \mathbf{k}_{eff} by $10\mu\text{rad}$ near 10 Hz would be large enough to limit the gradiometer resolution. It is therefore highly desirable to avoid these effects by proper design of the vacuum window interfaces or connecting the gravimeters in a single vacuum enclosure as in [58]. Effective methods for mitigating angular coupling in our device have been explored (see section 6.4 for example).

3.6 Enhanced sensitivity

At present, the sensitivity of atomic inertial sensors is competitive with state of the art technology. It is therefore compelling that options for significant improvement remain to be utilized. One possibility for enhanced sensitivity with atom interferometers is to make use of large momentum transfer techniques. A straightforward improvement

²This condition arises from the phase memory of the atoms. Therefore the angle between the beams must satisfy the condition of $k_{eff}ad \ll 1$, where d is the diameter of the atom cloud

to the gradiometer described here would utilize multiple Raman pulses which have been explored previously [59]. Figure 3.6 illustrates this technique which begins with a train of N π -pulses immediately following the first $\pi/2$ -pulse. The temporal spacing between these pulses is short compared with T and the atoms effectively separate with relative momentum $(4N + 2)\hbar k$. An additional $2N$ pulses then accompanies the middle π -pulse at $t=T$ to redirect the wavepackets. And the final string of pulses at $t=2T$ mirrors the first set. This has been shown to effectively multiply the sensitivity according to

$$\Delta\phi = (2N + 1) \mathbf{k}_{eff} \cdot \mathbf{a}T^2. \quad (3.38)$$

However, pulse efficiency plays a strong role here since the signal size quickly deteriorates as η^{4N+2} , where η is the single pulse efficiency. In our interferometer this efficiency is currently $\approx 80\%$, which leads to a quick degradation of signal.

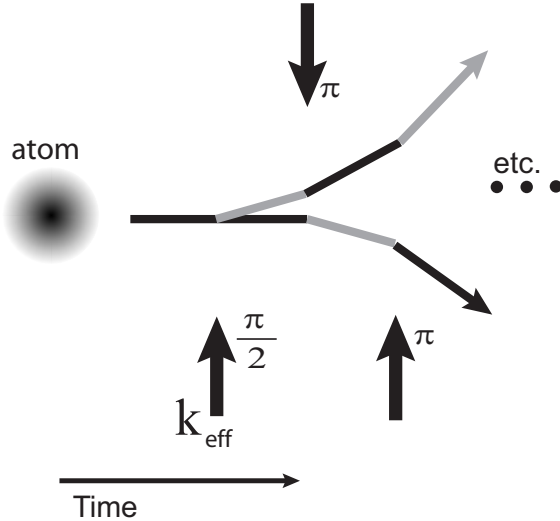


Figure 3.6: The initial sequence of pulses is used to achieve a large separation between the wavepackets. This is used to construct a large area interferometer. The interferometer sensitivity scales with $(2N+1)$ where N is the number of π -pulses following the beam splitter $\pi/2$ -pulse.

Other techniques exist such as adiabatic rapid passage (ARP) and scattering from optical standing waves. Using ARP, recoils as large as $100\hbar k$ have been demonstrated

[60]. With this method, the frequency detuning is slowly swept across the atomic resonance and the state vector adiabatically follows with high efficiency. The primary drawback of ARP is increased magnetic field sensitivity from populating $m_F \neq 0$ and increased spontaneous emission from the longer pulse lengths. In the case of Bragg scattering from an optical standing wave, the requirements of the velocity distribution of the atomic ensemble are strict. However, interferometers based on sub-recoil temperature atoms or even coherent atom sources such as Bose-Einstein condensates may prove to be a competitive choice [61].

Chapter 4

Apparatus

The development of this atom interferometer apparatus involved significant engineering accomplishments. Laboratory equipment and techniques were miniaturized to produce compact laser systems and sensors. This chapter describes the details of our atom fountain implementation followed by a presentation of the apparatus we constructed to create our gravity gradiometer shown in figure 4.1.

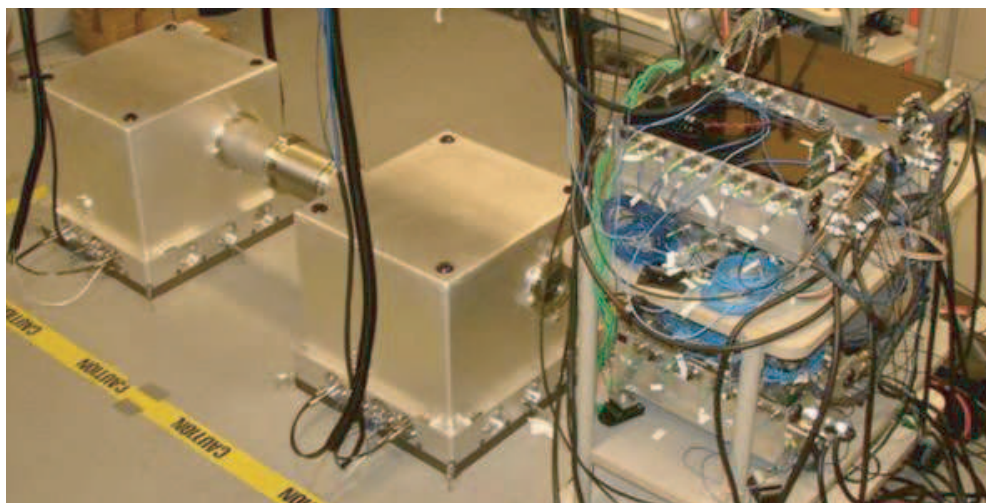


Figure 4.1: Photograph of the gradiometer system depicting the atom sensors housed within the cube-shaped vacuum enclosures along with the associated control lasers and electronics.

4.1 Cold atom fountain

The atom fountain is a common technique and used in renowned applications such as Cs fountain clocks which currently define the second at the 10^{-16} level [62]. All of the associated techniques are well-documented and are standard methods in the field of laser cooling and trapping. The following is an account of our cold atom fountain which is used to prepare a sample of atoms for the interferometer measurement. For detailed explanations, the reader is referred to *Laser Cooling and Trapping* by H. J. Metcalf and P. van der Straten [63] as well as the good overview in [64].

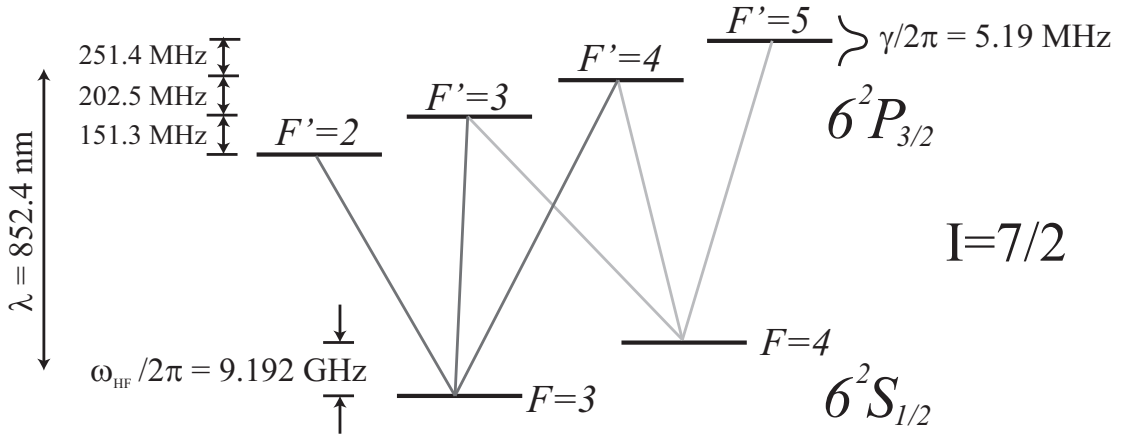


Figure 4.2: Energy level diagram for Cesium depicting the relevant transitions for laser cooling and trapping. The hyperfine structure arises largely from magnetic interactions of the electron's angular momentum with the nuclear spin, giving rise to ω_{HF} and the splitting of the $6^2P_{3/2}$ manifold. The linewidth of the 852 nm optical transition to the $F' = 5$ excited state is 5.19 MHz.

To begin the cycle, a two-dimensional magneto-optical trap (MOT) [65] feeds a 3D-MOT [66, 67] loading $\approx 10^9$ atoms in 100 ms. The magnetic field gradient is 2 G/cm in the 3D MOT and 10 G/cm in the 2D MOT region. The trapping beams are derived from the same master oscillator lasers which are locked to the $6^2S_{1/2} \rightarrow 6^2P_{3/2}$ transitions via fm-transfer saturated absorption spectroscopy [68] (see Fig. 4.2). The optical molasses beams are detuned $\delta = 11 \text{ MHz}$ red from the $|F = 4\rangle \rightarrow |F' = 5\rangle$ transition, a number which is optimized for signal¹. These beams have an intensity

¹See Appendix A for a detailed schematic of the laser frequencies used in this experiment

of $\approx 10 I_{sat}$ where $I_{sat} = 2.71 \text{ mW/cm}^2$ for mixed polarizations which is relevant in the context of the scattering rate formula for a 2-level atomic system given by

$$\gamma_p = \frac{s_0 \frac{\gamma}{2}}{1 + s_0 + \left(\frac{2\delta}{\gamma}\right)^2} \quad (4.1)$$

where $s_0 \equiv \frac{I}{I_{sat}}$ and $\gamma = 2\pi \times 5.18 \text{ MHz}$, the natural linewidth of the $P_{3/2}$ excited state in Cs. These beams are overlaid with a repump beam resonant with the $|F = 3\rangle \rightarrow |F' = 4\rangle$ transition to optically pump atoms back to the $|F = 4\rangle$ state. This is necessary should the atoms depump to the $|F = 3\rangle$ state through off-resonance excitation along $|F = 4\rangle \rightarrow |F' = 4\rangle$. A large number of atoms is desirable as the measurement is ideally atom shot noise limited in which case the signal-to-noise ratio (SNR) scales as $N^{1/2}$. However, a short loading time is also preferred since the sensitivity per unit time scales as $\sqrt{f_{rep}}$ assuming white noise, where f_{rep} is the repetition rate of the experiment. Beyond this, the 2D-MOT loading scheme also accomplishes the goal of separating the high-vapor pressure loading region from the science region which can be spoiled by the presence of a large background of thermal Cs atoms.

Following the loading phase, the 2D-MOT beams and magnetic fields are turned off to prepare for the fountain launch. During this time the atoms are confined in a 3D optical molasses while the eddy currents decay in the nearby optomechanics structure. The magnetic fields associated with a MOT have large gradients which can cause energy shifts in the Cs hyperfine structure and therefore systematic phase shifts. Furthermore, the polarization of the Raman fields are dictated by the local magnetic field and therefore are ill-defined in the context of large gradients over the fountain trajectory. These eddy currents are a significant problem and can be avoided in the future by replacing the Aluminum optomechanics structure with Stainless Steel possessing a resistivity of $\approx 200\times$ less than Al depending on the alloy. Although the fields are effectively extinguished, this 30 ms holding phase has the deleterious consequence that the atoms are now distributed within an optical molasses, losing some of the high compression or small size associated with a MOT.

After this holding phase, the atoms are launched upward with a moving molasses technique [69]. In this technique, the vertical molasses beams are ramped to detunings

opposite one another such that the atoms see an accelerating frame upwards. In our fountain, a detuning of ± 1.17 MHz is used to produce an upward velocity of ≈ 1 m/s. At this point, the temperature or velocity distribution of the atoms due to the trap dynamics is reduced with polarization gradient cooling [70]. This is vital since a typical optical molasses with Cs results in a Doppler limited temperature of:

$$T_D = \frac{\hbar\Gamma_N}{k_B}. \quad (4.2)$$

This corresponds to an average velocity of $\bar{v} \approx 9$ cm/s which leads to dramatic loss due to cloud spreading in the 200 ms fountain. On the other hand, polarization gradient (or sub-Doppler) cooling gives a final temperature of:

$$T_{PG} = \frac{\hbar\Omega_r^2}{k_B\Delta}, \quad (4.3)$$

which is limited by the photon recoil temperature.

$$T_{rec} = \frac{(\hbar k)^2}{2mk_B}. \quad (4.4)$$

Sub-Doppler cooling is achieved by detuning the MOT beams far from resonance (≈ 12 linewidths in our system) while the optical molasses intensity is reduced and finally extinguished. We reach a final temperature of $2 \mu\text{K}$ or $\bar{v} \approx 1$ cm/s measured with a velocity-selective Raman transition². A narrow velocity distribution is important to maximize the pulse efficiency of the velocity-sensitive Raman transition used to interrogate the atoms in the acceleration measurement.

Following the sub-Doppler cooling phase, the internal atomic states are distributed among all 9 magnetic sublevels of the $F=4$ ground state as a result of the MOT dynamics. The magnetic sensitivity of these states can be quite large considering that the first order Zeeman shift of Cs is $\delta\nu \approx m_F \times 0.35$ MHz/G. As an example, a magnetic field pulse during the interferometer leads to a phase shift of $\delta\phi = m_F \times 2\pi\delta\nu\delta t$ or $m_F \times 4$ mrad for a 1 mG, 1 ms pulse. This corresponds to a $\approx m_F \times 3.6$

²Recent experiments indicate the cloud temperature in our fountain is actually larger than what is measured using velocity-selective Raman transitions (See section 6.5)

ng signal which is comparable to our current noise floor. To drastically reduce the magnetic sensitivity, we remove all but the $m_F = 0$ sublevels using a combination of microwave and optical pulses. The remaining magnetic field sensitivity of the $m_F = 0$ state is a second order Zeeman shift according to $\delta\nu \approx 427 \text{ Hz/G}^2$.

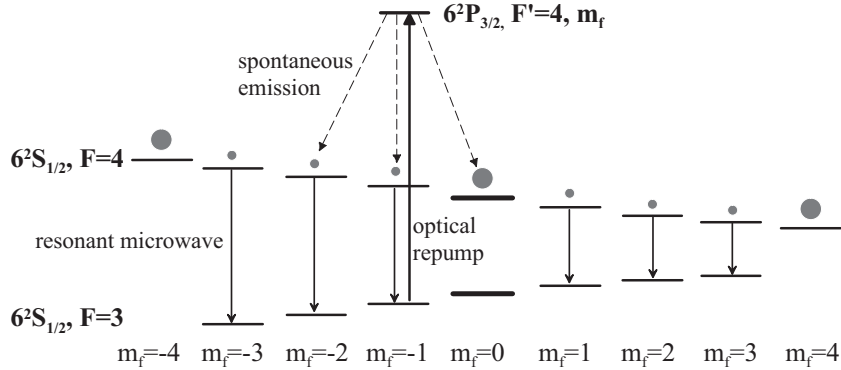


Figure 4.3: Diagram of the energy levels for the pulse sequence used to enhance the number of atoms in the $|F = 3, m_F = 0\rangle$ state. Resonant microwave transitions drive atoms to the $F = 3$ hyperfine state for all states except $m_F = 0$ and $m_F = \pm 4$. A repumper pulse redistributes atoms across the magnetic sublevels of the $F = 4$ state. After several cycles of microwave and repumper pulses, atoms will accumulate in the $m_F = 0$ and $m_F = \pm 4$ states.

To prepare a pure sample of atoms in the $6^2\text{S}_{1/2}$, $|F = 3, m_F = 0\rangle$ hyperfine state we use the following sequence of microwave and optical pulses. After the sub-Doppler cooling the repump light remains on for a few hundred microseconds to optically pump all atoms into the $F = 4$ state. A microwave π -pulse, tuned on resonance with the $|F = 3, m_F = 0\rangle \rightarrow |F = 4, m_F = 0\rangle$ hyperfine transition, at 9.192 GHz, transfers atoms to the $|F = 3, m_f = 0\rangle$ state with high efficiency. A magnetic field of 28.5 mG is used to break the degeneracy of the hyperfine microwave transitions such that the magnetic sublevels can be resolved in energy. To purify the sample, the remaining $F = 4$ atoms are cleared with radiation pressure from a 500 μs pulse of trapping light tuned 1 MHz above resonance. This sequence prepares about 1/9 of the original sample in the $|F = 3, m_F = 0\rangle$ state with high purity.

To improve the efficiency of the state selection we have developed a scheme using a sequence of microwave and repump pulses to enhance the number of atoms in

the $|F = 3, m_F = 0\rangle$ state. In this scheme the resonant microwave field is frequency modulated with a modulation index of $m = 2.40$ and a modulation frequency of 20 kHz. This creates a comb of microwave frequencies with sidebands separated by 20 kHz while the energy in the carrier frequency is nullified. The modulation frequency matches the spacings in the $\Delta m_F = 0$ microwave transition frequencies due to the 28.5 mG magnetic field as shown in figure 4.3. A 200 μs microwave pulse transfers atoms from $F = 4$ to $F = 3$, for magnetic sublevels $m_f = \pm 1, \pm 2$, and ± 3 , followed by a 10 μs repump pulse. The spontaneous emission from the $F' = 4$ then redistributes atoms across the $F = 4$ manifold. Throughout the process, the $|F = 3, m_F = 0\rangle$ sublevel remains dark which allows atoms to accumulate therein. The cycle of pulses is repeated up to 10 times. Afterward, the state selection sequence previously described is performed, resulting in approximately a factor of three gain in the number of atoms prepared in the $F = 3, m_f = 0$ sublevel. This Zeeman-state optical pumping enhancement is limited by accumulation of atoms in the $|F = 4, m_F = \pm 4\rangle$ states and by the presence of non-zero cross transitions due to a residual circular polarization of our RF field. The above sequence results in a 4 mm diameter cloud of $\approx 10^8$ cold atoms in the $|F = 4, m_F = 0\rangle$ hyperfine ground state moving upward at 1.1 m/s.

4.2 Portable atom interferometer system

This gradiometer system is designed as a prototype for a portable, three-axis gravity gradient measurement system. The portability of cold atom techniques is a necessary step for both science and technological applications. Space offers an advantageous environment for cold atom measurements and the stability that comes with a portable instrument will also quicken the pace of laboratory advancements. The possibility of employing atom interferometer sensors for gravity mapping and inertial navigation is also a strong motivator for this work.

The development of this system is the result of a remarkable effort by many scientists and engineers as noted in the acknowledgments. We designed and constructed a multipurpose laser system for the simultaneous operation of six inertial sensors. A host of custom designed control electronics is married with this system in a stackable

format. The inertial sensors consist of optical delivery hardware, a high-vacuum science chamber, and a state of the art atom detection system all housed in a dense, 30 cm cube. A conceptual layout is shown in figure 4.4. The laser system can be used to operate gradiometers, gravimeters or gyroscopes (see for example [58]).

4.2.1 Laser control system

The laser control system serves the function of providing the light and electronics necessary for atom trapping, launching and detection. The components are arranged in a stacking architecture controlled by a digital signal processor (DSP) as depicted in figure 4.4. The bottom DSP layer operates as the control center for the experiment, sending commands and receiving system information. The sensor layer directly interfaces electronically with the inertial sensors. The ascending layers are laser systems coupled with the appropriate electronics for controlling laser diodes and rf components. The master frame generates the seed light necessary for the experiment while the laser amplifier frame serves to provide independent gain channels for the master light resulting in frequency-controlled, switchable laser light. The following sections describe these layers in more detail.

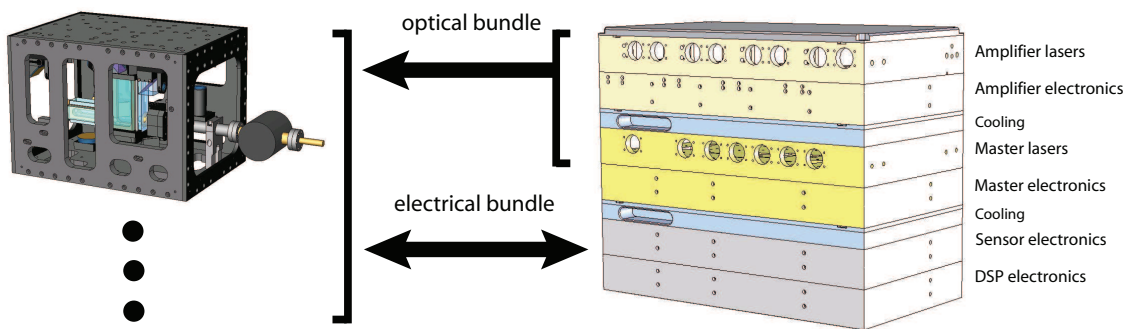


Figure 4.4: CAD representation of the portable laser control system (right) with the inertial sensors (left). The control system operates up to six inertial sensors. The upper layers provide the laser light (optical bundle) while the DSP and Sensor layers handle the signals for control and readout (electrical bundle).

DSP and sensor layers

The control electronics are designed around an SBC6711 DSP. This processor controls the experiment timing as well as all system set points (see Fig. 4.5). A remote terminal interfaces with the DSP via serial communications. This terminal executes a custom designed graphical user interface for system control. In this software, the user may define timing edges, adjust laser settings and frequency switching values as well as define sensor set points and monitor incoming data in graphical form. The DSP interfaces with the gradiometer system via a Servo16 I/O by Innovative Integrations. All digital signals are transmitted via a Low-Voltage-Differential-Signal protocol. Most system set points are controlled digitally with serially programmable resistors. The microwave frequency chain originates within the DSP layer and where a Wenzel 100 MHz oscillator is slaved to an SRS Rb time standard and multiplied 92 times to reach 9.2 GHz. Fine tuning is accomplished with a single sideband mixer. The sensor layer houses electronics dedicated to interfacing with the inertial sensors. Many functions for laser, RF and sensor control are performed by custom designed circuit boards which are fabricated in quantity. Pictures of the DSP and sensor layers are shown in Appendix B.

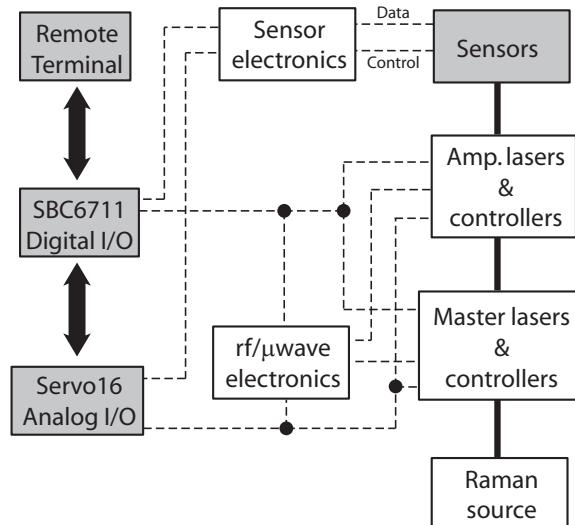


Figure 4.5: Schematic overview of the control system.

Master layer

The master laser frame produces the source light for all of the frequencies required to prepare, launch and detect the atoms. A photograph of the master laser system is shown in Appendix B. This frame is capable of seeding Raman beams, however the frequency noise of the Distributed Bragg Reflector (DBR) diode lasers is too large to achieve phase noise below 14 mrad per ellipse (see Fig. 5.12). An external cavity-locked laser now serves the purpose of seeding the Raman system as described in section 4.3. This frame houses two laser locks for trapping and cooling. A schematic illustration of this laser lock is shown in Fig. 4.6. The laser lock scheme relies on saturated-absorption fm-transfer techniques to derive an error signal for feedback to the diode laser. The lock is automated and controlled by a drop-down menu in the control software. After the user tunes this laser near to the desired atomic resonance, a DSP controlled routine scans the spectroscopic feature via the diode current to find the largest error signal. Once this setting is located, the routine activates the analog feedback electronics to lock the laser. The DSP monitors the lock status in between measurement cycles and relocks the laser if necessary. Additionally, the DSP will occasionally nullify the lock integrator by adjusting the laser current if the value is beyond a programmable set point. This feature maintains laser locks for months at a time without any user intervention. The two laser locks consist of an Eagleyard EYP-RWL-0870 DFB diode locked to the $|F = 4\rangle \rightarrow |F' = 5\rangle$ cooling transition and a Yokogawa YL85XNW DBR diode locked to the $|F = 3\rangle \rightarrow |F' = 2\rangle$ transition which provides repump light on the the $|F = 3\rangle \rightarrow |F' = 4\rangle$ transition after additional AOM frequency shifting (see Fig. 4.6 and Fig. A.1). The reduced 500 kHz linewidth of the Eagleyard DFB (compared to the 1 MHz linewidth of the Yokogawa DBR) enhances system performance by reducing the achievable sub-Doppler temperature which increases the detected atom number and eases requirements on the Raman laser intensity.

Double pass AOM's sweep the trapping light by 60 MHz for sub-Doppler cooling. Following this stage the light is fiber coupled and fed into amplifier channels as shown in Fig. 4.7. Additional frequency shifting for the fountain launch detuning occurs in these amplifier channels. Following the amplifier channels, the light is delivered to

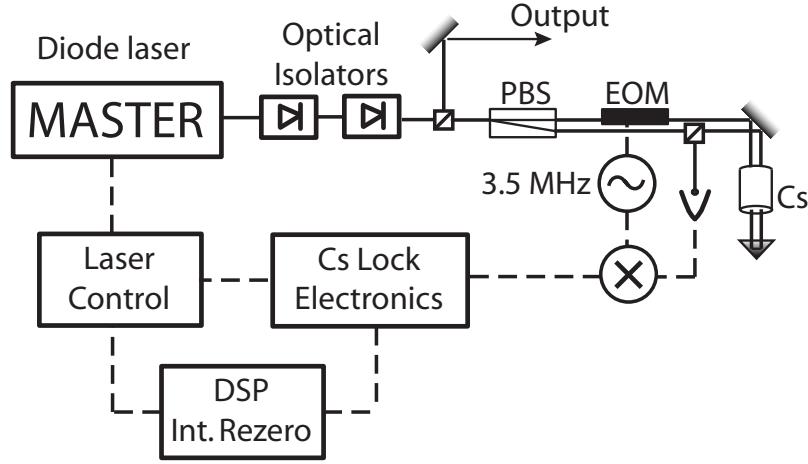


Figure 4.6: Schematic of the Cesium spectroscopy laser lock.

the sensor heads via fiber optics. The trapping beam of each sensor utilizes a single amplifier channel for maximum power whereas the repump light is amplified once and divided among the sensors with a CIRL evanescent wave fiber splitter.

The mirror mounts are custom designed flexure stages based on parts available from Optics For Research. They use opposing screws to adjust and lock the base tilt and a turret with a clamp plate allows for rotation. These mounts are the weak link in the ruggedness of the overall channel alignment. The waveplates and polarizers are also custom designed hardware as are the laser housings. The fiber couplers and laser output lens holders are 5 axis positioners (Optics For Research PAF-X). These lens positioners are mechanically secured with a low shrink, thixotropic (shape holding) epoxy (Angstrom Bond 9001MT). All other mechanical interfaces in the optical path, including the laser diode housing assembly, are fixed in place with a low viscosity, wicking epoxy (Tracon 2115). This assembly procedure provides immunity to mechanical shocks upwards of 30 g with regard to the fiber and laser coupling (see Fig. 4.8). The other components require additional development, however, the alignment of these channels is typically good to within a few percent over many months of operation which represents a significant improvement in cold atom light sources.

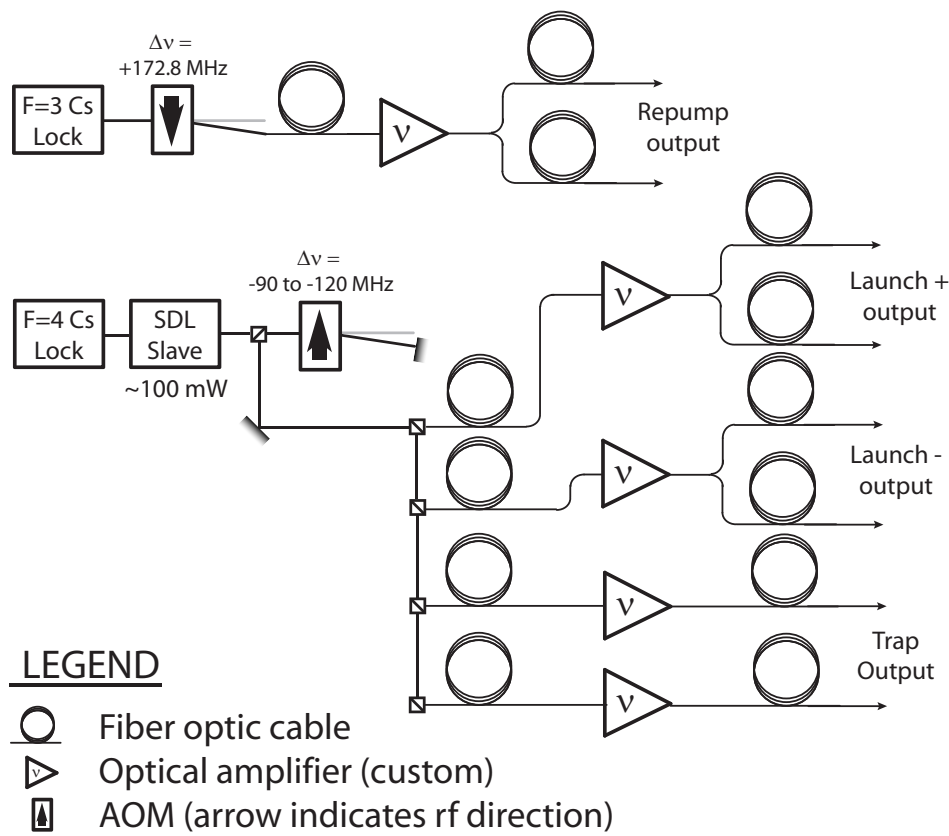


Figure 4.7: Schematic of the trap laser delivery scheme. All light is delivered to the sensors via polarization maintaining, single-mode fibers.

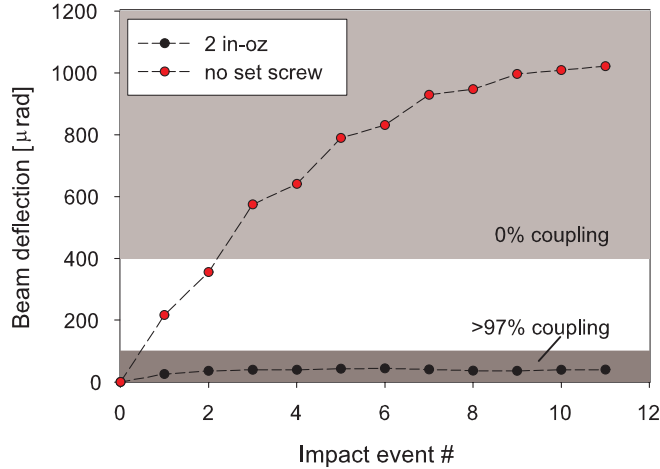


Figure 4.8: The fiber port securing scheme is designed to withstand more than 20 g's of mechanical shock. Shown here are the results from repeated impact testing at 23 g's of a fiber coupling. Two cases are compared, one without a set screw and one with a set screw torqued to 2 in-oz. The majority of the fiber couplings have required no adjustment for more than 18 months.

Amplifier layer

The system is designed to operate up to three amplifier frames. The amplifier laser frames are built as 8 independent amplifier channels which are fiber coupled. Each channel requires 0.5 mW input and can deliver up to 60 mW of fiber coupled, switched light with frequency control (see Fig 4.9). The extinction ratio of the optical switching is typically 65 dB. Pictures of the amplifier frame and the associated electronics are shown in Appendix B. The amplifier laser diode is an SDL 5411G1 with an AR coated output facet, fitted with a circularizing micro-lens by Blue Sky Research. This diode requires 0.5 mW to injection lock and has an output capability of 150 mW. The advantage of AR coating is an enhanced injection lock range typically spanning several mA of diode current and 0.2 °K in temperature.

The optical fibers are polarization maintaining with typical intensity fluctuations less than 1% due to polarization errors . Optical isolators are used to couple the seed light into the injection lock and control optical feedback. The acousto-optic modulators are NEOS 15180 operating at 180 MHz and provide optical switching as

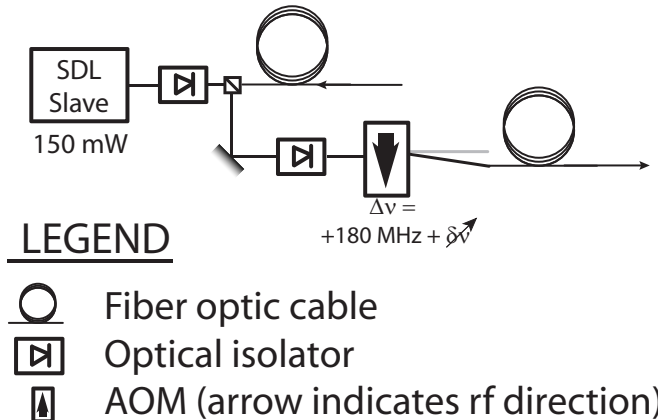


Figure 4.9: Optical amplifier channel in amplifier laser frame.

well as frequency control. The other components are identical to those used in the master laser frame.

4.2.2 Inertial sensor

The inertial sensor consists of an optomechanical system built around a predominantly glass vacuum chamber in which the measurement occurs (see Fig. 4.10). The atoms are sourced from a chilled ($12\text{ }^{\circ}\text{C}$) Cs reservoir which creates an atomic vapor that is transversely cooled by a 2D-MOT. This cold atom flux loads a 3D-MOT which is then launched vertically into a fountain trajectory where the measurement is performed. An optomechanics structure surrounding the cell serves as a mechanically stable delivery system for the trapping and detection light. The entire structure is enclosed in a partial vacuum chamber to isolate the measurement from index of refraction perturbations. A detailed description of these features follows.

Science Vacuum Cell

A photograph of the vacuum chamber is shown in Fig 4.11. The cell is constructed of Zerodur, a low expansion, low He permeability, ceramic glass. Hydroxide catalyzed bonding is used to construct the cells which are vacuum ready after several weeks of curing time. The surface flatness requirements are less than one micron over the

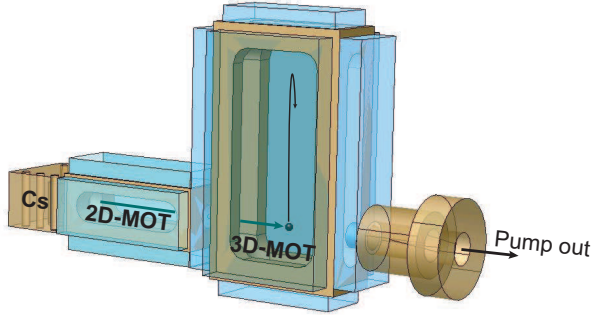


Figure 4.10: Diagram of atom fountain implementation. The atoms begin in a chilled Cs reservoir which creates an atomic vapor that is laterally cooled by the 2D MOT. This cold atom flux loads a 3D MOT which is then launched vertically into a fountain trajectory where the measurement is performed.

bonding area. This technique has several advantages: both sides of the glass may be AR coated, improved optical access in a compact design, and lack of magnetic or conductive materials which support eddy currents. The disadvantage of this approach is cost, glass to metal vacuum interfaces which are inherently difficult due to differing thermal expansion rates and the brittle nature of glass which increases the difficulty in mounting the cell.

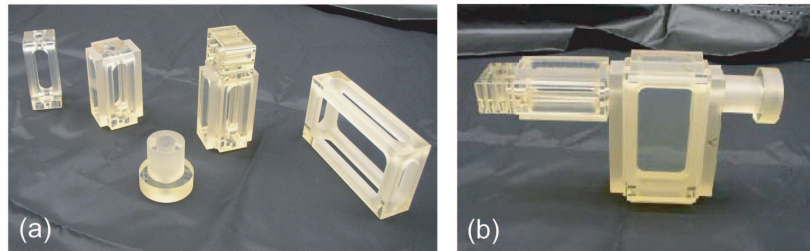


Figure 4.11: a) Depicts several of the prefabricated building blocks for the cell assembly. Zerodur is machined to shape the bonding surfaces are polished to sub-micron flatness. b) Depicts an assembled vacuum cell. Hydroxide catalyzed bonding enables the construction of vacuum tight, robust bonds.

Our vacuum system is attached to a Heatwave 2 l/s ion pump via an indium gasket. Great care is taken with mounting to constrain the chamber in only one place to avoid breaking vacuum. At the same time the Cs reservoir must be temperature

controlled to adjust the Cs vapor pressure in the 2D-MOT region. This places great demands on the mechanical design since heat removal from the cooling unit must be performed with a non-rigid attachment. Demonstrated solutions include customized heat pipes, water cooling with flexible tubing and copper braid attachments. Cs vapor management in the science region is accomplished with Poco graphite blocks which acts as a Cs getter [71]. The ultimate goal of this design is to take advantage of the low He permeability of the glass and operate an all-glass cell with only an activated getter as a pump.

The vacuum configuration is simply a 2D-MOT which sources a 3D-MOT. There is a 1 mm diameter hole between these two regions which acts as a differential pump to reduce the Cs vapor background in the science region. The 2D-MOT flux is aligned to pass through this hole and fluxes of 10^{10} atoms/s are routine. This flux is captured in a 3D-MOT and then launched vertically through the science region.

To prepare the vacuum cell, it is heated to 110 °C for 2 days while attached to a turbo pump. The temperature of the cell is kept below 150 °C to avoid melting the In gaskets. After baking, a pressure below 10^{-9} Torr is obtained. Next, Cs is transferred from an attached source to the cell. The Cs source is heated to 200 °C while the Cs reservoir is maintained at 20 °C with a refrigerated cold finger. After one day the cell is loaded with a visible amount of Cs. Very little is required since one mole of Cs would last much longer than several decades at a flux of 10^{10} atoms/s. Once these two operations are complete, the cell is detached from the turbo pump and the Cs source via copper pinch tubes. More than ten cells have been successfully prepared using this process. The cell is then fitted with magnetic coils for the MOT and clamped into the optomechanics box of the sensor head. The entire preparation and assembly can be completed in 4 days with pre-assembled parts.

Cell thermal profile

As discussed in Chapter 3, the parallelism of \mathbf{k}_{eff} at all three pulse locations is essential for obtaining maximum contrast as well as avoiding systematic offsets and susceptibility to short term noise. The main source of deviation from parallelism in our system is the thermal profile of our vacuum cell windows. The index of refraction

of Zerodur has an absolute thermal sensitivity of $\frac{dn}{dT} \approx 10^{-5}/^{\circ}K$ which translates to a beam deflection of $6 \mu rad/^{\circ}K/cm$. Gradients this large are readily achievable with a small heat source due to the low thermal conductivity of the glass and the resulting large fraction of heat lost to convective and radiative cooling. A finite element thermal model for our vacuum cell is shown in figure 4.12. With the appropriate boundary conditions which include resistive heaters and convective losses, this model closely simulates the temperature profile measured on our cell³. From this model it is evident that contrast reducing temperature profiles are present which must be accommodated in our apparatus.

Sensor head

The sensor consists of an optomechanics box which houses the vacuum cell, optical delivery components, magnetic field control and detection electronics. Miniature, flexure-based optical mounts with one inch apertures are mounted on the interior surfaces of the box to shape and deliver the light used for trapping, launching and detecting the atoms. This box is enclosed by two layers of magnetic shielding to isolate the Cs atoms from ambient magnetic fields.

The initial sensor design allowed for the simplified technique of dropping the atoms. This requires less frequency control and ensures repeatable cloud velocity conditions. Unforeseen limitations in detection SNR limited our sensitivity to $1500 E/\sqrt{Hz}$ in this configuration. As the sensitivity scales with the interrogation time squared, we redesigned the sensor head to allow for atom launching, thus quadrupling the sensitivity. Figure 4.13 compares the Raman beam configuration for the two cases employing the same vacuum cell design. The symmetry of the fountain further simplifies the Raman beam delivery, requiring only 2 levels. However, the launch requires a modification of the trap laser frequency control and electronics to facilitate the required frequency ramp. Furthermore, additional cloud expansion from the longer fountain must be accommodated in the detection scheme by enlarging the

³To be accurate, the resistive heaters are no longer necessary due to improved Cs gettering. However, the magnetic coils contribute a similar load. The point is not to precisely model the effect, but rather to recognize its existence such that it can be mitigated or avoided completely

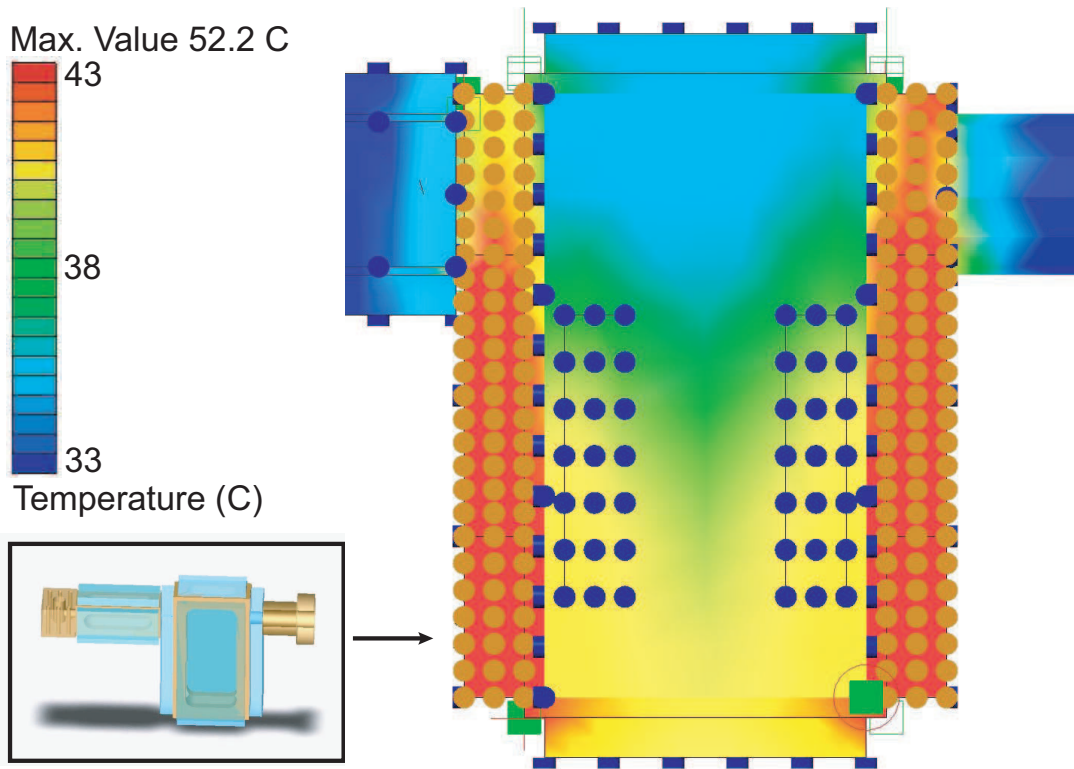


Figure 4.12: Finite element model for the temperature profile of our Zerodur vacuum cell. Heat sources placed vertically along the sides (red dots) decrease the presence of Cs vapor in the science chamber. Convective losses result in the thermal profile on the large window through which the Raman beams pass. This thermal profile affects the index of refraction according to $\frac{dn}{dT} \approx 10^{-5}/^{\circ}K$ which steers the Raman beams through the resulting gradient in the index of refraction. An appropriate redesign of the vacuum cell can eliminate these problems.

vertical beams (see Fig. 5.1).

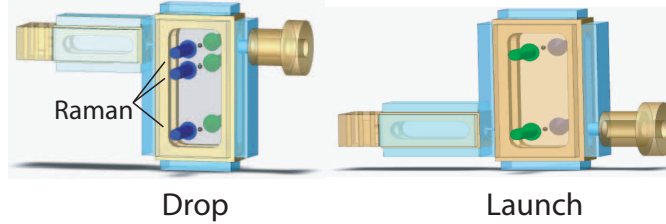


Figure 4.13: Raman beam configurations for the drop and launch interferometer are shown. The launch simplifies the Raman beam delivery, requiring only 2 levels instead of 3 and at the same time quadruples the sensitivity.

A drawback of the Aluminum enclosure is the eddy currents associated with the low resistivity. During magnetic field shutoff sequences after the initial MOT loading, the eddy currents delay the extinction by 30 ms. This may account for the large size of our MOT and furthermore, it inhibits bias field switching necessary to achieve colder temperatures. The use of stainless steel as in [58] would greatly improve this situation though the resulting in a heavier sensor.

Partial vacuum enclosure

Experimentation with the gradiometer system revealed index of refraction perturbations to be a dominant source of phase noise. To eliminate this noise, the gradiometer was retrofitted with a partial vacuum enclosure. The vacuum enclosure is designed to be modular with the sensor head and evacuates to 10 - 100 mTorr. The enclosure shown in figure 4.1 consists of a heavy base structure to mount the sensor and Raman beam optics with a cubic top which is lowered to seal the system similar to a bell jar design. The material was chosen to be Aluminum for greater strength to weight ratio, an important parameter for the mobile platform. The biggest design challenge for the enclosure is reducing the effects of box deformation during evacuation. The enormous atmospheric force causes visible deformation which produces unacceptable alignment errors with a simple design.

Finite-element-analysis was used to test design ideas to arrive at a base structure which minimized beam deflection. The basic design principle is to support an internal

breadboard by four corner blocks in the base. This locates the breadboard anchor points at the most stationary points in the structure. Furthermore, the forces on the corner blocks from the deforming sides balance one another to minimize the deviation of the breadboard attachment points. Modeling showed that this structure is not perfectly balanced and other structures were added along with a steel bottom plate to further constrain the base and achieve acceptable performance. In practice, it is found that the Raman beams still deflect by $100 \mu\text{rad}$ during evacuation and motorized mirror mounts were installed to compensate after pump down. The addition of other struts may mitigate this deflection. The strongest impact is systematic which can be corrected. This deflection should increase the sensitivity to angular beam jitter, however, it remains to be seen at what level this will occur.

The vacuum feedthrough requirements for each sensor are many. Several optical fibers, high-voltage cabling, chilled water, microwave cabling and dozens of electrical lines are accommodated by the enclosure design. All feedthroughs pass through the base such that the tops may be easily removed without disturbing the cabling. Of particular concern are the optical fiber connections and high voltage cabling. The optical fibers are not generally interchangeable between ports and in practice each fiber is dedicated to its particular frame output alignment. Therefore the existing fibers are retrofitted for feedthrough. To do this we open the fiber jacket, remove all local Kevlar strands and backfill the local region with epoxy (Tracon F118). This region was then potted within a metal cylinder which mates with a standard vacuum barrel fitting. The strain of this epoxy was found to have negligible effects on the fiber performance, in particular, the polarization maintaining performance.

Second, the high voltage for the ion pumps present a significant problem as the pressure regime is nearly at the most susceptible point on the Paschen curve which describes the breakdown voltage as a function of pressure [72]. Qualitatively, this occurs because the susceptibility of the air to breakdown is a trade off between carrier density and mean free path. At low pressures, there are not any available carriers to support conduction whereas at high pressure, the mean free path is too short to allow the charged particles to obtain the energy needed for impact ionization. With our conditions, arcs of 10 cm were observed which eliminates the use of standard

connectors. We were able to circumvent this problem by enclosing the entire cable in plastic tubing which maintains a pressure close to atmospheric.

4.2.3 Ground vehicle platform

We demonstrate that this gradiometer system successfully operates aboard a ground vehicle. Early tests with the system in this vehicle showed that this concept is possible provided that care is taken with regard to magnetic field variations and the gradiometer tilt sensitivity as described in section 6.4. Using this platform, the gravitational anomaly from underground voids will be mapped to validate the use of our compact system for experiments at remote locations. It is interesting to note that atom interferometry techniques are especially suited to dynamic environments [73]. Since the sensors rely on position measurements of the Cs atom at discrete instances in time, the technique automatically filters high frequency disturbances in contrast to classic analog sensors with high bandwidth.

Our mobile platform is a Ford E-Super Duty box truck which accommodates the entire gradiometer system. An engineering team developed a custom leveling platform based on a 3-axis gimbal on which to mount the gradiometer. The platform is large enough to accommodate a 1.8 m gradiometer baseline. This platform is actively stabilized with a low frequency servo loop using an LN250 inertial motion unit as a platform reference and another identical unit as a feedforward sensor on the truck floor. For proper gradiometer operation, the platform must exhibit linear accelerations much less than 1 m/s^2 to avoid Doppler shifts which tune the Raman beams off resonance. This is largely accomplished with controlled vehicle motion which is achieved by an after market electric motor linked to the drive shaft which maintains steady velocities less than 1 mph. Furthermore, angular rotations create spurious phase shifts through centrifugal accelerations as described in section 3.3.3. The gimbal system addresses these requirements with an angular drift of less than $100 \mu\text{rad}$ in 100 ms.

4.3 Low-noise Raman interrogation system

A major source of interferometer phase noise for a gradiometer system is due to the frequency instability of the Raman laser. We have mitigated this problem with an extended cavity diode laser locked to an optical cavity. This section presents the Raman interrogation system based on this laser which is used to achieve our current performance.

4.3.1 Raman laser system

The Raman laser system shown in figure 4.14 is a New Focus Vortex 6017 laser locked to an optical cavity via the Pound-Drever-Hall technique [74, 75]. The cavity is built from low-expansion Zerodur in a hemispherical mirror geometry with a finesse of 8000. Care is taken to vibrationally isolate the cavity lock breadboard from acoustic disturbance by placing the system on lead-foam stand offs from a floating optical table and surrounding it with a sound reduction enclosure. This system delivers a laser linewidth < 25 kHz which is below the resolution of our 3 km delayed self heterodyne linewidth analyzer. The cavity length and therefore resonance frequency is piezo controlled and in this manner locked to a Cs resonance to eliminate drift and reduce low frequency acoustic noise. A 1 GHz frequency offset is inserted between the cavity and the Cs lock via a fiber modulator. This enables a large single-photon Raman detuning from the $6^2P_{3/2}$ excited state reducing spontaneous emission. Using this setup we have demonstrated an improvement in gradiometer phase noise from 38 mrad/ \sqrt{Hz} with a $\delta\nu = 1$ MHz linewidth DBR diode master to 4.4 mrad/ \sqrt{Hz} .

The scrubbed output from the cavity is fiber coupled and amplified with an AR-coated SDL diode injection lock, then split for further amplification and frequency control. At this point a small quantity of power is extracted (not shown) to beat with the F=3 master light in order to determine the single-photon Raman detuning. The split light is delivered to two amplifier channels to create the two Raman frequencies Raman A and Raman B (as shown in figure 4.14). The amplified outputs are then coupled into two Photline NIR-MPX50-LN08 fiber modulators operating at 9.2 GHz with the modulation depth set to maximize the first order sideband. The technique used to excite the Raman transition is depicted in figure 4.15. Modulating one beam at

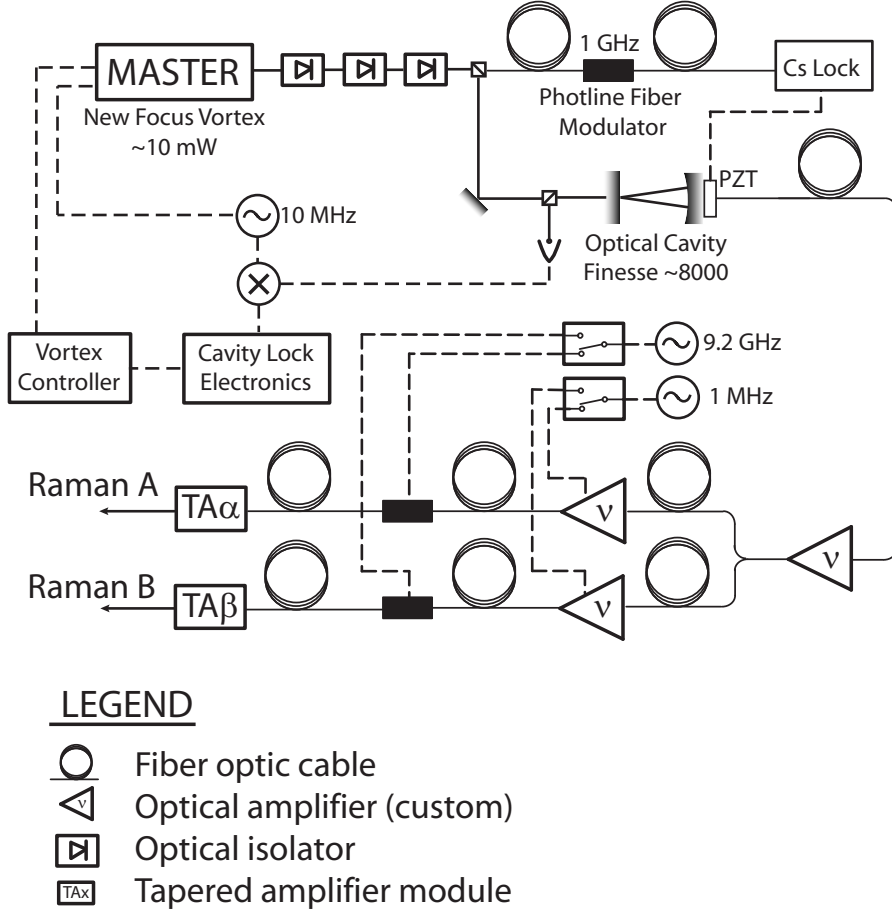


Figure 4.14: Schematic of the Raman laser system.

a frequency δ from the hyperfine frequency allows the atoms to discriminate between the carrier of the modulated beam and the counterpropagating beam. Toggling the modulation between the two beams allows reversal of \mathbf{k}_{eff} .

The fiber modulator output is coupled into a tapered amplifier module inside the vacuum enclosure which delivers more than 300 mW. This module consists of an Eagleyard tapered amplifier chip, alignment optics, and a spatial filter which serves an auxiliary purpose of avoiding catastrophic back-coupling. This output is then collimated and delivered to the atoms.

The beams are collimated to an $r_{1/e} = 6$ mm beam waist and routed through a periscope to the two-level Raman beam configuration (see Fig 4.16). A crossed linear

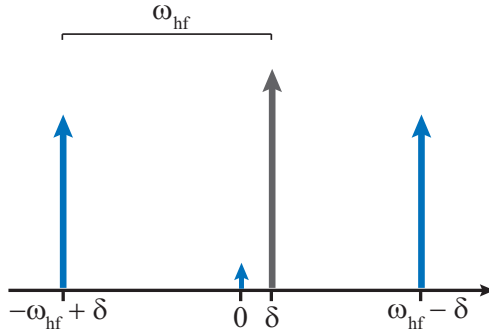


Figure 4.15: Frequency spectrum of Raman laser implementation. One beam is modulated at an offset δ from the ground state hyperfine splitting frequency. Properly configuring the frequency of the counterpropagating beam makes the atom resonant with only the sideband of one beam and the carrier of the other.

polarization scheme is used since it is less susceptible to parasitic reflections giving rise to standing wave AC Stark noise. A PLX HM-25-1G corner cube reflector guarantees the parallelism of the the two beam levels to within $5 \mu\text{rad}$ which is essential for good interferometer contrast.

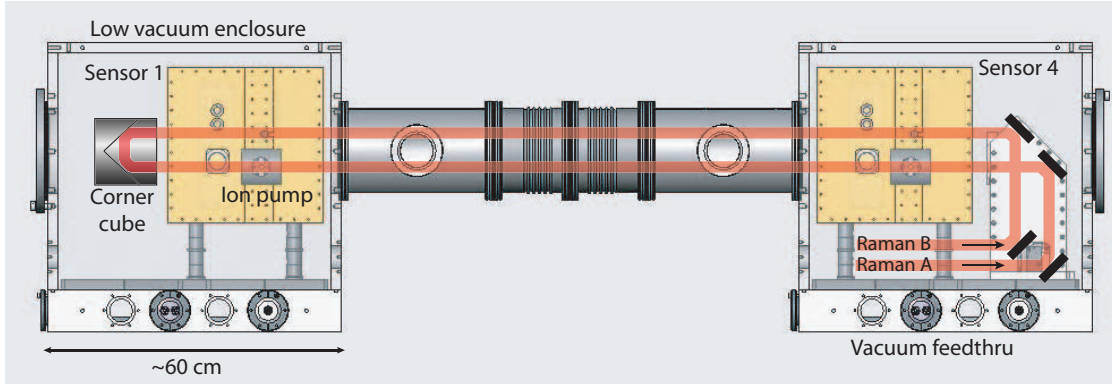


Figure 4.16: Schematic of the Raman laser delivery.

4.3.2 High contrast requirements

To obtain high contrast it is necessary that the Raman beam size, quality and power be sufficient to accommodate the atom cloud size and velocity profile. The cornerstone of these quantities is the velocity profile of the atom cloud which dictates the Raman

beam intensity in two ways. Consider first that the Raman transition has a resonance condition that is Doppler sensitive which simply means that unless the pulse is short enough such that its Fourier transform spans the entire Doppler frequency profile, atoms outside this transform will not undergo a transition and therefore will not participate in the interferometer. This results in a reduction in interferometer contrast and therefore SNR. Recall that the pulse length required to complete a transition is inversely proportional to the two beam intensities according to:

$$\tau_\pi \propto \frac{1}{(I_a I_b)^{1/2}}. \quad (4.5)$$

Second, the velocity profile drives the cloud expansion during the fountain (see Fig. 4.17). This in turn drives beam size selection in that it is necessary to have the entire cloud see a uniform intensity such that the Rabi frequency is uniform among all atoms. For a given beam power, the intensity and therefore Rabi frequency fall off as the square of the beam size. Therefore, it is extremely favorable to have a cold ensemble not only to reduce the Raman size requirements, but also to reduce the required beam power. Lastly, it is necessary to have a homogeneous optical wavefront since the atoms explore different parts of the beam during the interferometer which requires a flatness of less than 1 mrad over the spatial extent of the cloud.

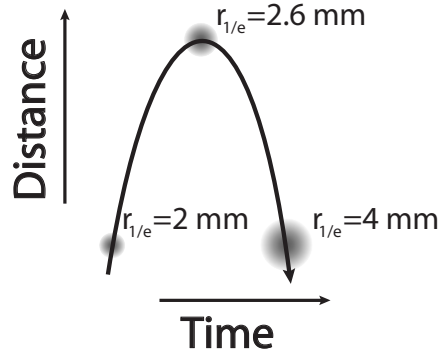


Figure 4.17: Cloud expansion during fountain due to finite cloud temperature.

In our system, the cloud temperature and lack of optical power have limited the transfer efficiency of our pulses to 80% which leads to interferometer fringe visibilities

of 55%. Composite pulse techniques may improve this transfer efficiency as demonstrated by [76] but take longer to complete which increases spontaneous emission. Figure 4.18 shows a typical pulse frequency scan demonstrating transform limited signatures (see section 6.5 for further discussion). Enhancements to beam size and power offer straightforward improvements to the pulse efficiency.

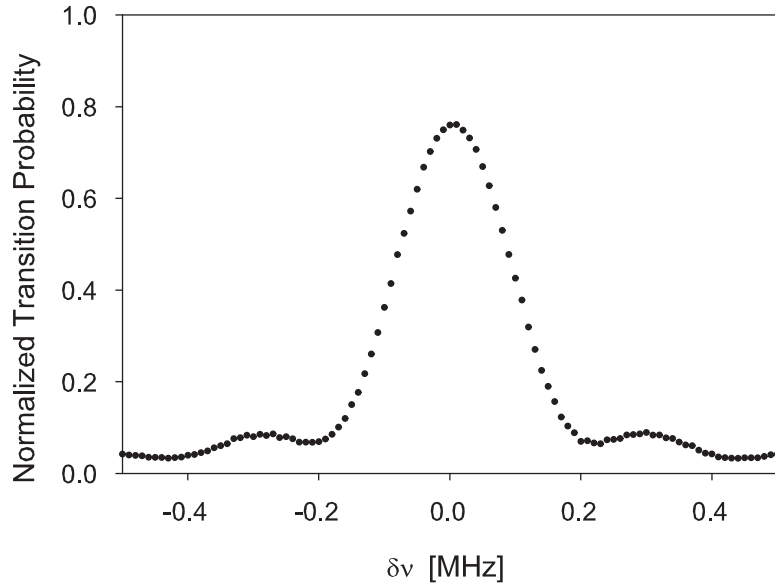


Figure 4.18: π -pulse frequency scan showing typical transfer efficiency and Sinc function features indicating operation in the transform-limited regime. With $\Omega_R \gg \delta\nu_{thermal}^{FWHM}$, all atoms see nearly identical Rabi frequencies which allows for better pulse transfer efficiency. In this case, $\Omega_R/2\pi \approx 100$ kHz and $\delta\nu_{thermal}^{FWHM} \approx 75$ kHz.

Chapter 5

Data Extraction

5.1 Low-noise detection technique

Laser cooled atoms are used in a variety of instruments of scientific and technological importance, including cold atom clocks [62], gravimeters [77], gyroscopes [25] and gravity gradiometers [24]. The overall performance of each of these instruments hinges on precise measurement of atomic transition probabilities for atomic ground-state hyperfine transitions. These probabilities are inferred from low-noise state-selective detection of the participating atomic states. If populations in both states are detected, the transition probability can be determined from these measurements in a way which is immune to atom number fluctuations in the atom source (normalized detection). This is important because, for laser cooled atom sources, these fluctuations are typically on the 1% level and otherwise limit the measurement sensitivity. On the other hand, the quantum projection noise limit [78] for ensembles of 10^8 atoms is 0.01%.

We describe here a normalized detection method suitable for determination of the transition probabilities at signal-to-noise (SNR) levels approaching 10⁴:1 per shot using atomic resonance fluorescence. Our approach blends methods previously used for implementing normalized detection in atomic clocks [62] and atom interferometers [79]. It combines the basic fluorescence detection approach of [62] with simultaneous state detection introduced in [79]. In principle, this combination eases constraints on detection laser frequency and amplitude noise during the detection process, enabling

quantum projection noise limited performance for large ($> 10^7$) numbers of atoms.

In [62], the atomic states are detected sequentially at different times as they fall through two spatially separated detection regions. Consequently, frequency or amplitude noise on the detection laser affects the scattering rate of the atoms and can be a limitation to achieving high SNR. Stabilization of the detection laser is required to overcome this limit. On the other hand, in [79], the two states are detected simultaneously to suppress the sensitivity to detection laser noise. Radiation pressure is applied to spatially separate the two states to enable simultaneous measurements of the populations of the two states at two different spatial locations, and pump-probe modulation transfer spectroscopy is used to discriminate background vapor atoms from cold atoms.

In the work described below, we use a similar technique to spatially separate the atomic clouds, but use fluorescence, rather than modulation transfer, to read-out the populations (we have improved the vacuum cells to eliminate the large background vapor of [79]). This has the advantage of simplifying the optics paths and enforcing a high level of common-mode rejection of correlated noise sources. In particular, the fluorescence is imaged simultaneously onto opposite quadrants of a quadrant photodiode (see Fig. 5.1) which suppresses common-mode technical noise arising from detection laser amplitude and frequency noise. Using this technique with an ensemble of $\sim 10^8$ atoms, we demonstrate a nearly quantum projection noise limited SNR of 7830:1 per shot and 14400:1 in one second.

5.1.1 Detection scheme

The details of the detection scheme characterization are as follows. Using standard atomic fountain techniques, we prepare a $2 \mu\text{K}$, $3 \text{ mm } 1/e^2$ radius cloud of $\sim 10^8$ Cesium atoms in the $6^2S_{1/2} F = 3, m_f = 0$ hyperfine state moving upward at 1 m/s . Next, we drive a microwave $\pi/2 - \pi/2$ clock using the Ramsey separated oscillatory field method [80], to create an equal superposition of the two hyperfine ground states¹ (see Fig. 5.2). The time between pulses is $50 \mu\text{s}$ and the Ramsey phase is set to $\pi/2$

¹This technique suppresses the influence of microwave power fluctuations during the clock sequence.

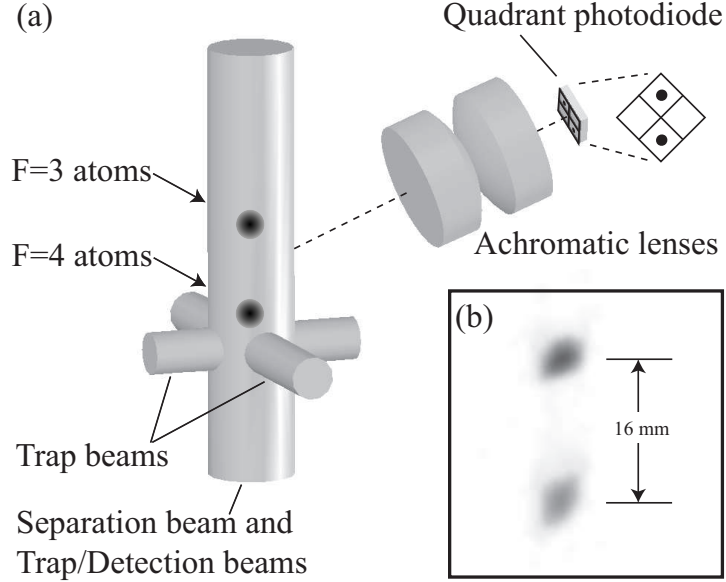


Figure 5.1: (a) Depiction of the setup. An inverted image of the $F = 4$ and $F = 3$ atoms is projected onto opposite quadrants of the detector. (b) A negative CCD image of the spatially separated $F = 3$ and $F = 4$ atoms.

by shifting the phase of the 9.2 GHz microwave oscillator between the pulses. With the atoms still moving upward at 1 m/s, radiation pressure resonant only with the $F = 4$ hyperfine level is applied to collapse the superposition and redirect the $F = 4$ atoms to spatially separate the two states. The populations of the two states are then measured by imaging the light induced fluorescence onto opposite quadrants of a quadrant photodiode. The experiment is carried out with a repetition rate ranging from 5 Hz to 12 Hz.

We spatially separate the two hyperfine states with a vertically oriented downward propagating beam affecting only atoms in the $F = 4$ state which is turned on for 65 μ s. The separation beam is derived from an Eagleyard DFB diode laser with a 500 kHz full-width at half-maximum instantaneous linewidth that is locked to the appropriate transition using frequency modulation transfer spectroscopy [68]. This 6 mm $1/e^2$ radius beam is resonant with the $F = 4 \rightarrow F' = 5$ transition and has an intensity of 6 mW/cm². This resonant laser projects the coherent superposition into a statistical mixture of atoms in each atomic state and redirects atoms projected into

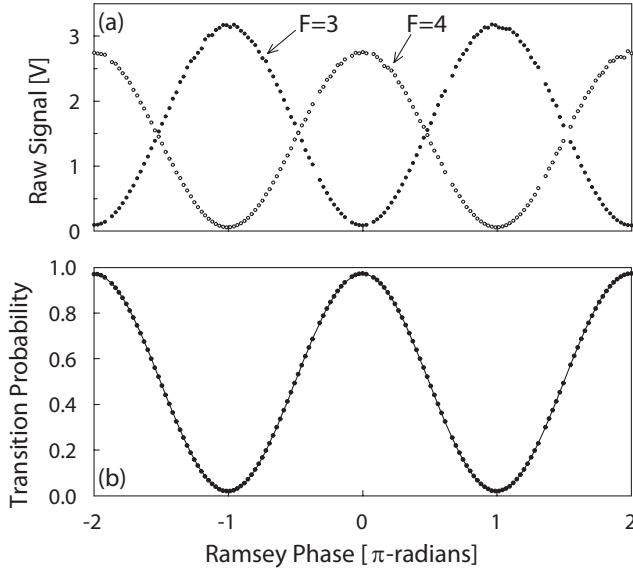


Figure 5.2: (a) Raw clock fringe signals from a typical $\pi/2 - \pi/2$ Ramsey sequence with $T = 50 \mu\text{s}$. (b) Normalized transition probability from $F = 3$ to $F = 4$ state. Normalization removes shot-to-shot atom number fluctuations and reveals that cross-contamination due to optical pumping during the separation pulse is less than 1%.

the $F = 4$ state downward to the image location of the upper detection quadrant (see Fig. 5.1). Meanwhile the atoms in the $F = 3$ state continue to propagate upward to the image location of the lower detection quadrant, resulting in a spatial separation of the two ensembles. Immediately following the separation pulse, repumping light resonant with $F = 3 \rightarrow F' = 4$ is turned on for $500 \mu\text{s}$ to optically pump the $F = 3$ atoms into the $F = 4$ state for detection. Each atom cloud then propagates for 6 ms to achieve a total separation of 16 mm at detection.

The size of the separation beam is critical to achieve good contrast in the fringe resolution. As the scattering rate is a function of intensity, the nonuniform profile of the beam maps onto the total velocity recoil imparted to the $F = 4$ atoms. To overcome this effect, one may increase the intensity well beyond the saturation intensity at the cost of a greater ratio of atoms lost to depumping through the off-resonant $F = 4 \rightarrow F' = 4$ transition. Furthermore this may not be practical given design constraints. We explored the affect of separation beam size on state resolution. Figure 5.3 shows two theoretical calculations for the atom cloud distribution after separation.

We found that a beam size 50% larger than the cloud size is sufficient which agrees with our measurements.

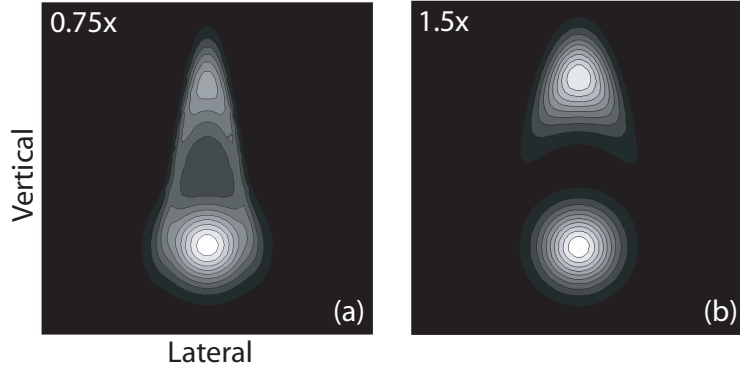


Figure 5.3: A comparison of separation beam size with respect to atom cloud size and the resulting affect on cloud distribution of the $F = 4$ atoms (upper cloud). A beam 50% larger than the cloud size is sufficient for good detection (i.e. contrast).

For detection, two counter-propagating vertical beams resonant with the $F = 4 \rightarrow F' = 5$ transition are applied to the atoms for $150 \mu\text{s}$ (detection beam parameters are identical to the separation beam described above). Figure 5.4 shows the spatial distribution of the atoms during the detection stage as a function of interferometer phase. The resulting fluorescence from each spatially separated atom cloud is imaged onto separate quadrants of a $10 \text{ mm} \times 10 \text{ mm}$ quadrant photodiode (Hamamatsu S5981) through two stacked 30 mm focal length achromatic lenses arranged for $2\times$ demagnification (Fig. 5.1). The imaging system collects 1.3% of the fluorescence or ~ 20 photons per atom. Each quadrant photocurrent output is independently integrated over the detection time. Johnson and photodetector dark current noise are negligible.

We use the quadrant detector outputs to calculate the normalized transition probability to the $F = 4$ state, $P_4 = V_4/(\epsilon V_3 + V_4)$. In this expression, V_3 is the integrated voltage from the $F = 3$ lower quadrant after accounting for scattered background light, V_4 is the corresponding $F = 4$ upper quadrant signal, and ϵ is a coefficient accounting for the difference in detection efficiencies for the $F = 3$ and $F = 4$ atoms. This coefficient is experimentally determined by scanning the phase of the Ramsey

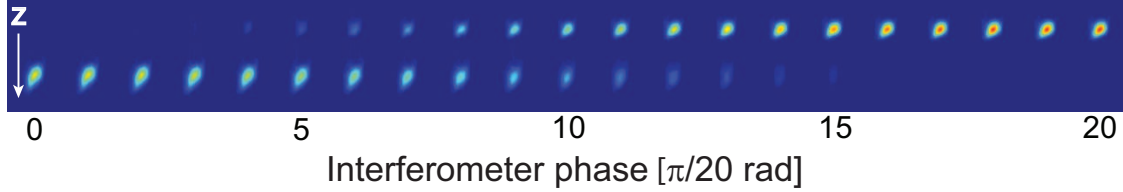


Figure 5.4: A sequence of CCD images showing the population transfer between the hyperfine ground state levels by scanning a microwave interferometer.

fringe to systematically vary the internal atomic state of the atoms between $F = 3$ and $F = 4$ and is typically near 0.8 (see Fig. 5.2). The slight difference in the overall detection efficiency for the two states arises from the fact that one state is subject to the separation pulse, while the other is not. The SNR testifies to the shot-to-shot stability of $F = 3$ and $F = 4$ detection efficiencies.

5.1.2 System performance

Phase noise in the microwave source produces fluctuations in P_4 which limit the measurement of the SNR of the detection system in a single clock to $\sim 1400:1$. Therefore, we characterize the SNR by comparing the observed transition probabilities of two nearly identical clocks driven by a common local oscillator as in [81]. The difference $\Delta P_4 = P_4^a - P_4^b$ between the two clocks (clock a and clock b) rejects this common mode RF phase noise (see Figs. 5.5a and 5.5b). The standard deviation of the shot-to-shot difference between the normalized outputs of the clocks, $\sigma_{\Delta P}$, is therefore used to measure the noise limit of the detection system. The standard deviation $\sigma_{\Delta P}$ is determined by averaging the standard deviation from successive bins of ΔP_4 time records or from the Allan deviation of these records (see Fig. 5.5c). We infer the single clock SNR performance by assuming the residual noise arises from uncorrelated noise processes in each clock, so that $\text{SNR} = (\sigma_{\Delta P}/\sqrt{2})^{-1}$ following the convention of [33]. Using this method we infer a single clock SNR of 7830:1 per shot and 14400:1 in one second.

In order to identify the noise limit of the system as atomic shot noise, we measure the SNR as a function of atom number (Fig. 5.6). We accomplish this by changing the atom loading time for each clock. Since the number of atoms loaded in the two traps is

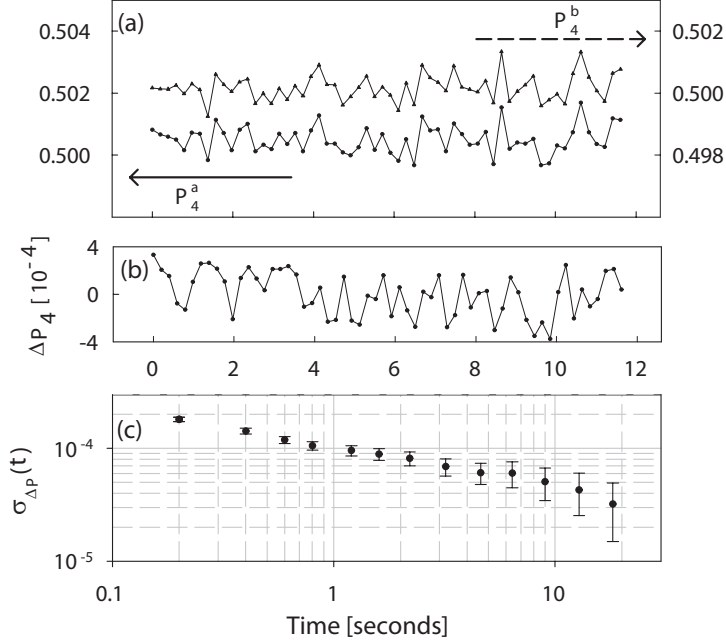


Figure 5.5: (a) Segment of normalized $F = 4$ signals from each clock recorded with a 5.1 Hz repetition rate. The difference between the normalized signals ΔP_4 is shown in (b). The 2-Sample Allan Deviation for this set (c) gives $\sigma_{\Delta P}=1.81 \times 10^{-4}$ rms deviation per shot, corresponding to a cross-clock SNR of 5540:1 or 7830:1 per clock. The present $\sim 10^2$ sec limit to the long term stability may be increased by improving the current microwave delivery system which imposes uncommon noise in the two clocks.

not generally the same, we calculate an effective atom number $\tilde{N} = 2N_a N_b / (N_a + N_b)$, where N_a and N_b are the atom numbers for clocks a and b , respectively. We infer the atom numbers N_a and N_b from the photodiode fluorescence signals, photodetector quantum efficiency, detection solid angle, and calculated atom-photon scattering rate. Uncertainties in the latter quantities result in a factor of ~ 2 uncertainty in the absolute atom number calibration. We observe an $\tilde{N}^{1/2}$ scaling of the SNR consistent with that expected from atom shot noise limited detection.

Finally, it is interesting to compare the measured SNR with the calculated limits for a sequential detection technique. For example, consider the impact of uncorrelated laser frequency fluctuations $\sigma_\nu \sim 200$ kHz between detection events for an intensity roughly 2 times saturation intensity. Assuming the laser is tuned to linecenter, the

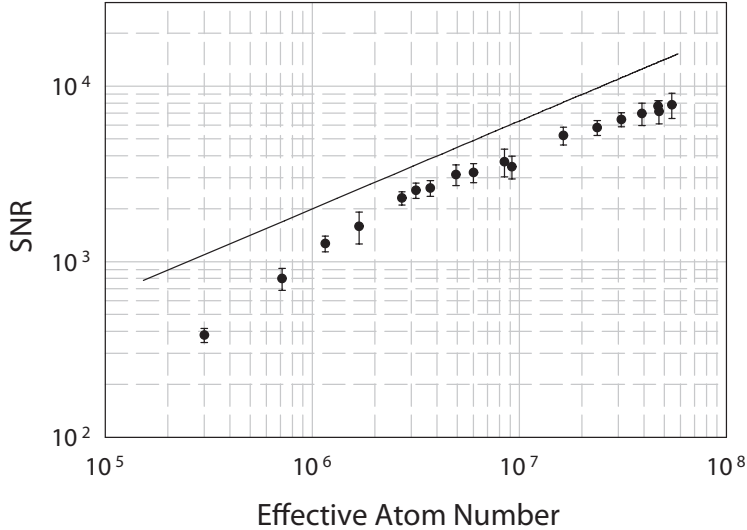


Figure 5.6: SNR is measured as a function of atom number by varying the trap loading time. The measured $\tilde{N}^{1/2}$ dependence suggests that the detection system is limited by atom shot noise scaling. Background noise dominates below 10^6 atoms. The line is an estimate of the quantum projection noise limited SNR ($2\tilde{N}^{1/2}$).

frequency fluctuations result in 0.3% fluctuations in the scattering rate, which in turn result in fluctuations at the same level in the inferred number of atoms detected in each state, and an SNR limit of just 1000:1. In practice, frequency immunity can be limited by the separation pulse. As an illustration, consider a change in the separation velocity of the $F = 4$ atoms which is a product of the change in scattering rate. The resulting jitter in the cloud position at detection degrades the SNR due to the spatial dependence of the detection efficiency. This sensitivity can be mitigated by increasing the ratio of the photodiode size to that of the imaged atom cloud.

5.2 Gradiometer sensitivity

The differential acceleration sensitivity of this interferometer is approaching atom shot noise limited phase resolution. In fact, we have demonstrated the lowest phase noise gradiometer of this type. This is the result of two key discoveries, the limiting effects of index of refraction perturbations between the atomic ensembles as well as Raman laser frequency stability. In this section, we present the current performance

capability of the gradiometer including an illustration of short and long term noise performance, followed by a discussion of noise sources and how they manifest in the signal.

5.2.1 Current performance

As previously discussed, each accelerometer output is dominated by acceleration noise due to vibrations of the optical delivery system. Due to the equivalence principle, it is impossible to distinguish between acceleration of the atoms and the reference mirror. In our setup, this noise completely randomizes the phase at levels larger than π -radians (see Fig. 5.7). This noise can be largely reduced as was demonstrated previously [77]. Since our system shares this noise between two interferometers, the difference phase is preserved with high fidelity. Therefore, to extract the differential phase between the interferometers we plot these two signals parametrically and fit an ellipse to the result which removes the common mode phase noise by nearly three orders of magnitude [82]. This technique also takes advantage of the common mode noise to scan the phase of the ellipse (see Fig. 5.8) and typically produces a good fit in 20 shots.

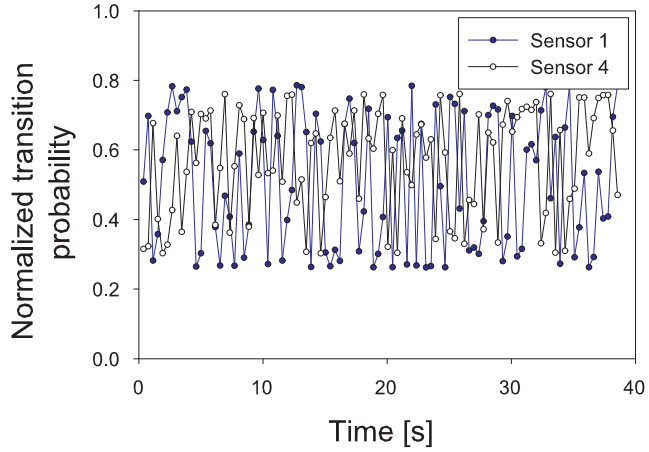


Figure 5.7: An example of normalized transition probabilities from the two interferometers which comprise the gradiometer. Common-mode noise in the optical delivery system masks the phase information in the individual sensors while the difference phase is preserved (see Fig. 5.8).

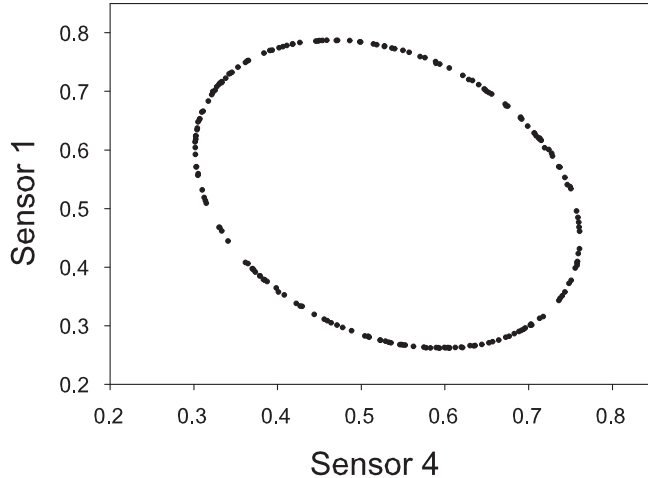


Figure 5.8: Common mode acceleration noise is suppressed when the accelerometer outputs are plotted parametrically. 200 data points form this example of a low phase noise ellipse. The shot-to-shot fluctuations of the phase readout indicate a noise of 1.6 mrad per 20 point ellipse.

However, it also gains a susceptibility to slight drifts in detection offsets and interferometer phase during the collection of the ellipse points which typically takes 8 seconds for the 20 points. Figure 5.9 shows an analysis of measured phase noise as a function of ellipse points. It is clear that more than ten points are needed to achieve a good fit and at long times, system drifts also degrade the ellipse fit performance. Recent work on this problem has shown that Bayesian techniques can be applied to the ellipse phase estimation to reduce the number of points required and also reduce the noise and systematic offset associated with simple ellipse fitting [83].

To determine the short term sensitivity of the interferometer we log a time record of the ellipse phase values and perform a double 3 sigma outlier cut on a dedrifted version of this record (see Fig. 5.10). To avoid erroneous results, we dedrift according to 20 ellipse phase averages. We then calculate root-mean-square values of successive windows of 20 dedrifted phase points. We remove 3 sigma outliers from this record according to the average rms value, then dedrift the data a second time and remove 3 sigma outliers again. This protects the dedrift routine from the effects of very large outliers and the second cut typically removes much fewer points than the first.

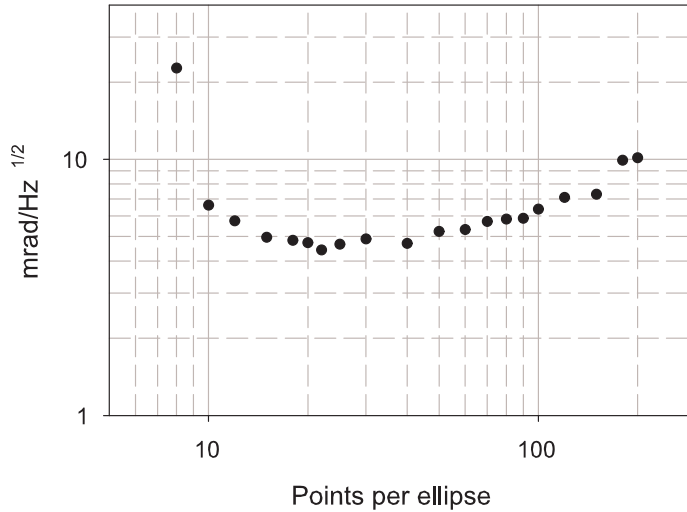


Figure 5.9: An analysis of phase noise per unit time as a function of ellipse points. At least 10 points are needed to produce a good fit whereas large numbers are limited by slow system drifts. A quantity near 20 points per ellipse is found to be optimal.

Using this technique we observe continuous time records with a short term noise of 1.6 mrad per ellipse (See fig 5.10). In this case $T = 85$ ms and our repetition rate was 2.55 Hz giving a differential acceleration sensitivity of $4.2 \text{ ng}/\sqrt{\text{Hz}}$. The long term performance shows white noise averaging for 2×10^3 sec (See fig. 5.11). It is very likely that drifts beyond this time will correlate well with system temperatures.

5.2.2 Noise Discussion

It is useful to divide the gradiometer noise sources into two classes: readout noise, and interferometer phase-noise. Readout noise includes fixed noise sources such as electronic noise and detection noise. In our system this is typically less than 10^{-3} of the interferometer signal size and is therefore negligible. Also embedded in readout noise is atom shot-noise which represents a fundamental limit to the atom interferometer sensitivity. Both of these noise sources can be reduced with enhancements to the atom number and contrast.

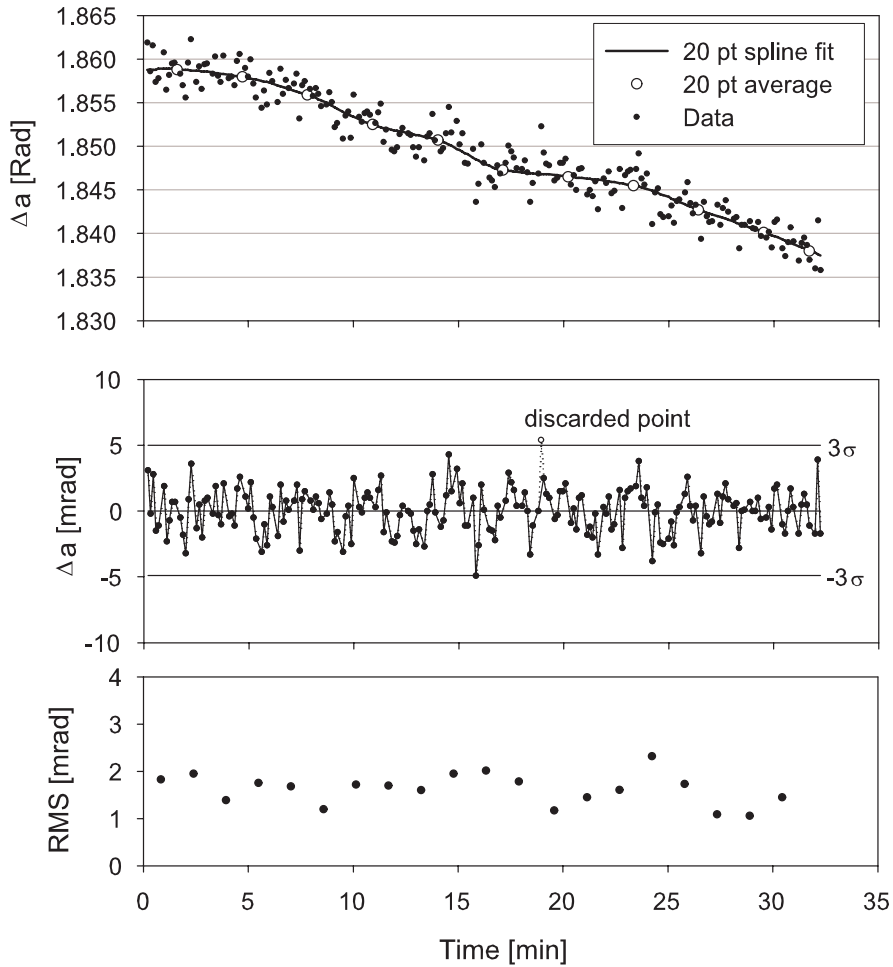


Figure 5.10: Method for determining the short term noise of the gradiometer. The analysis indicates 1.6 mrad/ellipse or $4.2 \text{ ng}/\sqrt{\text{Hz}}$.

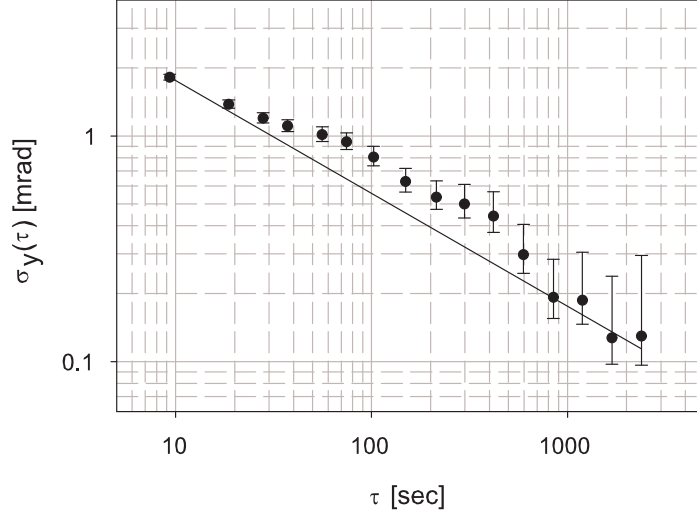


Figure 5.11: An Allan deviation analysis of the phase stability from the gradiometer shows that the system can integrate as white noise for periods of 2.5×10^3 seconds. Here 0.1 mrad corresponds to ≈ 2 E. No attempt is made to correlate the data with system environmental parameters—the likely culprit of long term drifts.

On the other hand, fixed interferometer phase-noise cannot be reduced with enhanced atom number and contrast. This category of noise has a clearly identifiable signature. Consider first a sinusoid with phase noise: the amplitude fluctuations of the signal is always the quietest near the peaks. Likewise, differential phase noise manifests itself in ellipse plots by similar narrowing of the ellipse thickness near the peaks of the two sinusoids (see Fig. 5.12(a)). Raman laser frequency noise and inter-sensor beam perturbations both manifest this quality.

It is interesting to note that the dominant noise in this system was initially index of refraction perturbations to the Raman beam between the sensors. Phase readout below 1 mrad is routinely achieved in optical interferometers [84], but the presence of heat sources in our system makes this impossible due to the resultant index of refraction driven beam perturbation effects. We therefore constructed a low vacuum enclosure resulting in the reduction of differential phase noise from greater than 190 mrad/ \sqrt{Hz} to 38 mrad/ \sqrt{Hz} . At this level, the differential phase noise is limited by the Raman laser frequency stability. As demonstrated in section 6.3, a discrete

laser frequency change during the interferometer results in a phase error of order $\delta\phi \approx \delta k_{eff}L$ where $\delta k_{eff} = 4\pi\delta\nu/c$. This was first discussed in [24] and later in [85] where it was shown that the interferometer phase noise is a strong function of the laser frequency noise spectrum up to a cutoff frequency defined by the Rabi frequency. The $\delta\nu = 1$ MHz linewidth of the previously used Raman seed laser (DBR diode) limits the interferometer sensitivity (Fig. 5.12(b)). By replacing this source with the $\delta\nu \approx 25$ kHz linewidth cavity-locked laser in section 4.3.1 the noise drops to 4.4 mrad/ \sqrt{Hz} (Fig. 5.12(c)). This succession of improvements is captured in the ellipse data shown in figure 5.12. Although many parameters were explored to achieve this performance, the two key factors of removing the air from between the sensors and stabilizing the Raman laser frequency proved to be the most important.

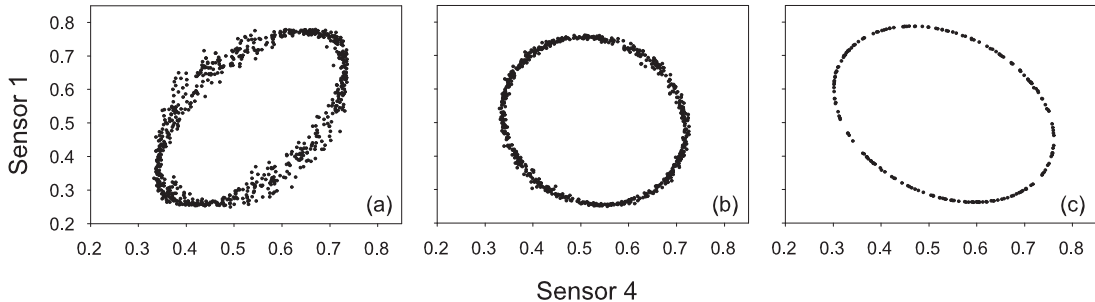


Figure 5.12: Successive ellipse plots representing key noise limits. (a) shows typical data with air between the sensors revealing 190 mrad/ \sqrt{Hz} . (b) shows typical data after evacuating the air but still generating the Raman beams with a DBR diode laser giving 38 mrad/ \sqrt{Hz} . (c) shows the improvement after implementing the cavity locked laser discussed in section 4.3 giving 4.4 mrad/ \sqrt{Hz} .

Chapter 6

Gravity tests

The remarkable success of light-pulse atom interferometer techniques has motivated competitive research in precision metrology [26, 25]. Using our compact gravity gradiometer system we have performed several proof of concept tests of Newtonian gravity. We perform a measurement of the gravitational constant with a precision of 3×10^{-4} , which is competitive with the present limit of 1×10^{-4} . Straightforward improvements can enable uncertainties falling below 10^{-5} . This experiment can also be interpreted as a test of the inverse square law which statistically constrains a putative Yukawa type fifth force to 8×10^{-3} near the poorly known length scale of 20 cm. Limits exceeding 10^{-4} appear to be feasible. We also perform an experiment which tests the atom interferometer in the context of a time-dependent gravity potential. Additional work is also presented which tests the atom interferometer in the context of a time-dependent gravity potential with time scales less than the interrogation time T. Other measurements which support the analysis and conclusions from this work are also shown.

6.1 Testing gravity with an atom interferometer

6.1.1 The gravitational constant

As discussed in section 1.2.2, the gravitational constant is a poorly known fundamental quantity. The 2006 CODATA adjustment determined G with a reduced precision

of 1×10^{-4} due in large part to the significant disagreement between measurements [35]. The accuracy of these measurements is also questionable due to a recently discovered systematic in conventional torsion techniques [40]. It is therefore paramount to measure G with independent methods. Atom interferometry offers a unique approach to compliment conventional methods and provide an independent system for determining G at levels exceeding 10^{-5} .

Configuration

In this experiment we take advantage of a symmetric source mass configuration to reduce sensitivity to the atom-source position (see Fig. 6.1). Relative positioning of the source mass and atoms is a significant error source in previous measurements of G using atom interferometry [26]. By placing the source mass symmetrically between the sensors we make second order the dependence of the field on source deviations in all directions including rotations. The limiting case suggested by this experiment is that of an infinite slab of thickness d having spatial extent much larger than either the atom-source separation or the fountain height. In this case, the field strength depends only on the source mass thickness according to $2\pi G\rho d$ and all other dimensional dependences are highly suppressed.

For technical reasons, our experiment is performed with a small asymmetry in the distance of the two sensors from the source masses. This is tolerated since accuracy is not the present aim of this demonstration. Furthermore, calculations show that our position repeatability of $< 5 \mu\text{m}$ is sufficient for precisions approaching 10 ppm and our Allan deviation analysis does not indicate the presence of any slow drifts.

Each of the two 540 kg source masses consists of 45 - 2" x 4" x 8" lead bricks which are stacked securely with shims and strapped tightly to a LinTech 174630 precision positioning table with a 16 mm pitch, ball-screw drive. The positioning system is designed to allow for fast relocation of the source mass between the two end points which translates into a 70 cm travel in less than 8 seconds with a $5 \mu\text{m}$ repeatability. The table, motors and drivers are specifically chosen to tolerate the torque and linear accelerations required for this motion profile. We use a LinEngineering 5718L-03P stepper motor with Intelligent Motion Systems IM805 step drivers for this purpose. The positioning is made repeatable with simple mechanical limit switches at either

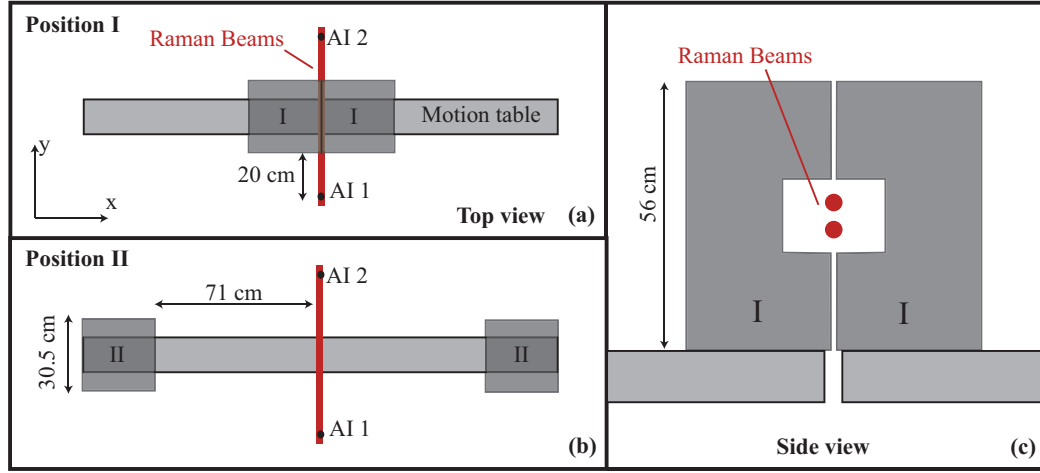


Figure 6.1: Mass-sensor configuration for gravity measurements. The source masses are chopped between positions I and II, (a) and (b) respectively. A side view is shown in (c) depicting the cutout to allow Raman beam propagation between the sensors.

end triggered by sloped flags. These switches must be approached slowly at ≈ 1 mm/s to avoid overshoot due to the large inertia of the system.

To modulate the field for the G measurement, the source masses are chopped between position I and position II (see Fig. 6.1). The signal at each position is averaged for 5 ellipse cycles or 40 s and then the mass is repositioned. These parameters were chosen to minimize the introduction of noise from slow drifts in the the gradiometer phase. The mass motion is triggered by the interferometer timing system to synchronize the motion with background scans in the data collection procedure.

Results

Using the technique described above, we measure the signal associated with modulating the gravity field between two values. A typical section of data is shown in figure 6.2.(a). To analyze the data, we use a local, linear dedrift algorithm according to:

$$\Delta\phi_i = \phi_i^{II} - \frac{1}{2} (\phi_i^I + \phi_{i+5}^I), \quad (6.1)$$

where I and II refer to the concatenated time records at the two positions. Simulations show that an Allan deviation of the results from this routine underestimates the short

term noise by 13 %. However, at long times, the Allan deviation calculates an accurate result since the dedrift is a localized function.

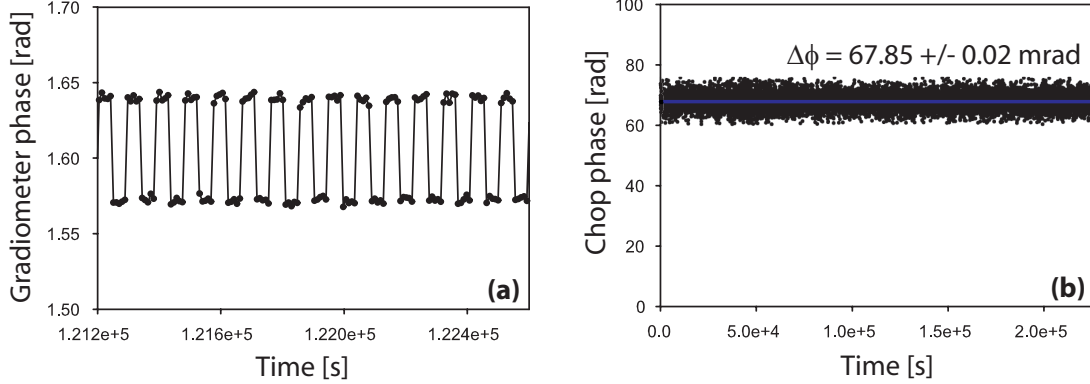


Figure 6.2: (a) The gravity potential is chopped between two values to remove the sensitivity to long term drifts in phase. A typical section of data shows that the SNR of the modulated signal is 34:1 and the repetition rate is 0.01 Hz. (b) Difference signal of the the chopped gradiometer phase. A local linear dedrift is used to remove drifts on the time scale of the signal modulation. The resulting phase is determined to be $\Delta\phi = 67.85 \pm 0.02 \text{ mrad}$.

Occasional sections of data are particularly noisy due to the loss of Raman laser cavity-lock and these sections are removed before analysis. The resulting time records are concatenated and the data shown in figure 6.2.(b) is obtained using the analysis routine defined above. An Allan deviation of this record (see Fig: 6.3) reveals that the brick chop signal integrates as $\tau^{-1/2}$ for at least 10^5 seconds. The bump between 10^2 and 10^4 seconds is an artifact of the short term dedrifting routine and does not affect the results at longer times. If we extrapolate the $\tau^{-1/2}$ trend to the full length of the data run, the phase shift is determined to be $\Delta\phi=67.85\pm0.03 \text{ mrad}$ which gives a precision of

$$\frac{\sigma_G}{G} = \frac{\sigma_\phi}{\Delta\phi} = 3 \times 10^{-4}. \quad (6.2)$$

This demonstrates that our system has the potential to produce a competitive measurement of the gravitational constant.

Improvements such as large momentum transfer atom optics and shot noise limited detection could very well result in more than an order of magnitude improvement thus

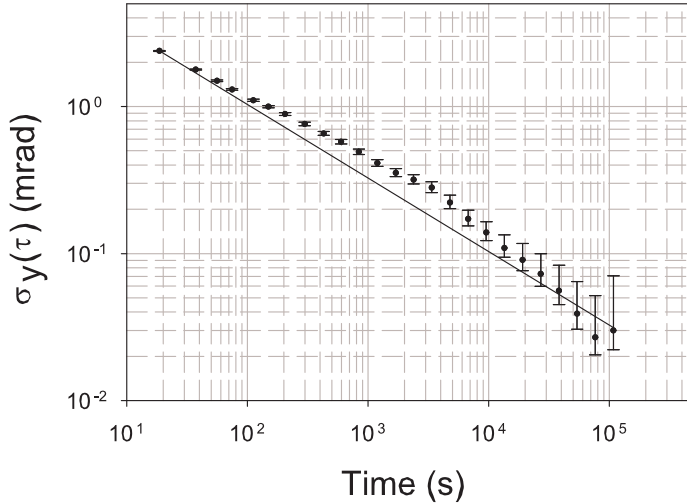


Figure 6.3: Allan deviation of the difference phase. The local dedrift algorithm results in a signature bump in the signal between 10^2 and 10^4 seconds. At longer times, the accuracy of the Allan deviation is restored.

exceeding the 10^5 level. For example, a $6 \hbar k$ multiple-pulse sequence gives a 3-fold increase in sensitivity [59]. Furthermore, the system has yet to realize a factor of 5 improvement in SNR to reach the atom shot-noise limit as discussed in section 6.5. These enhancements would combine to give a precision approaching 6×10^{-6} for 30 day averaging. It is notable that reconfiguring the sensors to bring the source mass to within one inch of the atoms results in only modest improvements roughly doubling the signal. However, the position of the sensors is adjustable such that additional mass may be used to further enhance the signal. Combining these modifications can result in a determination of G which exceeds 10^{-6} .

Sources of error

We identified and corrected the largest source of error in our system before the experiment. This systematic sensitivity was on the order of the mass signal itself, a result of an adjustable wedge in one of the two Raman beams. This optical wedge was used to

correct the interferometer contrast which was degraded due to inhomogeneous temperature profiles on the the vacuum cell windows. We found that this optic gave a large sensitivity to tilts in the gradiometer assembly due to floor deflections from the source mass positioning. We observe a sensor rotation about the Raman beam axis of $\approx 3 \mu\text{rad}$ between the mass positions using an Applied Geomechanics 755-series tiltmeter (see Fig. 6.4). Removing this wedge largely suppressed this sensitivity. We subsequently corrected the contrast by strategic positioning and tuning of resistive heaters on the cell window to compensate for the deleterious thermal profile discussed in section 4.2.2.

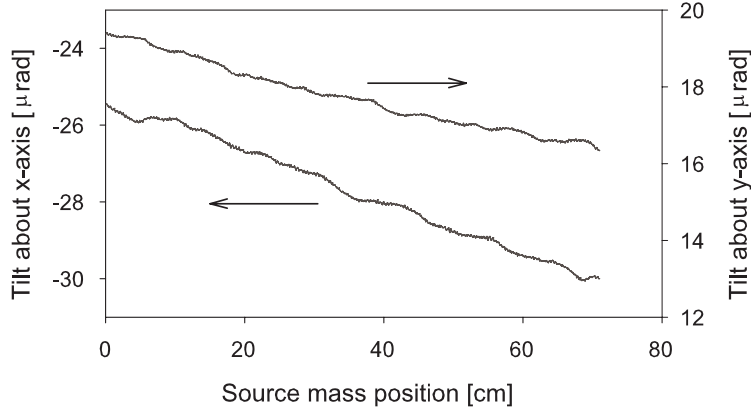


Figure 6.4: Floor tilts about the x and y-axis due to source mass position. The high frequency features are due to short term noise in the tiltmeter and limited averaging.

This experiment is designed to demonstrate only the precision capabilities of the gravity gradiometer and its usefulness for competitive measurements in gravitational physics. Nevertheless, we consider here the expected gravity signal from this source mass to facilitate future improvements. Due to the irregularity of the brick sizes and spacings we take the measured total mass as our given and distribute this evenly over the source mass dimensions. This is to be contrasted with the technique of integrating the source mass density over the source mass volume. We determine the average brick mass by weighing 30% of the bricks with a Pennsylvania Model 7500 scale calibrated with a NIST traceable proof mass. We model the source as a 3-dimensional array of point sources spaced by $\approx 1''$ with mass $m_0/64$ where m_0 is the average mass of one

lead brick. The calculation then becomes:

$$a_y = \sum_i \frac{Gm_i y_i}{(x_i^2 + y_i^2 + z_i^2)^{3/2}}, \quad (6.3)$$

since the sensor is only sensitive to projections of the force along the Raman beam axis. This is easily analyzed with a 3-dimensional matrix containing position and mass data entries. The advantage of this approach is the possibility to modify the matrix values to consider errors due to rotations of the mass block and departures from a rectilinear shape. We have compared the results with that for finer decimations and find no improvement within our accuracy tolerances of 1%.

The largest geometrical sensitivity in this arrangement is due to MOT position uncertainties along the Raman axis. Uncertainties along the two orthogonal axes show reduced sensitivities, 2 orders of magnitude smaller due to the large spatial extent of the source in these directions. The stringent atom-source positioning requirements along the Raman axis may be significantly reduced if one has precise knowledge of the separation between the two MOT clouds. This takes full advantage of the symmetrical source mass positioning. As a demonstration, we show in section 6.3 that modulating the single photon detuning of the Raman beams from the $6^2P_{3/2}$ excited state may be used to precisely measure the sensor spacing. If this relative distance is known, then the atom-source distance need only be measured to within 1 mm for a 10^{-5} measurement - a level already demonstrated in [26] and only a factor of 2 better than what is shown here.

Using this technique, simple mechanical measurements determine the calculated signal to be 64.9 ± 0.7 mrad, limited largely by the knowledge of the separation distance of the two brick stacks. This uncertainty can be easily overcome with well designed source masses. This value clearly disagrees with the measured value of 67.85 ± 0.02 mrad. However, this calculation relies on a regularity in both the density and rectangular shape of the source mass, neither of which are good assumptions. Therefore, systematic errors may exist in this calculation which have yet to be explored.

Figure 6.5 compares the calculated and measured gradient as a function of source mass position. The two signals abruptly depart from one another for positions close to the sensors. This could be explained by a scale-factor error due to an inaccurate density determination of the source. Further testing is needed to determine the exact

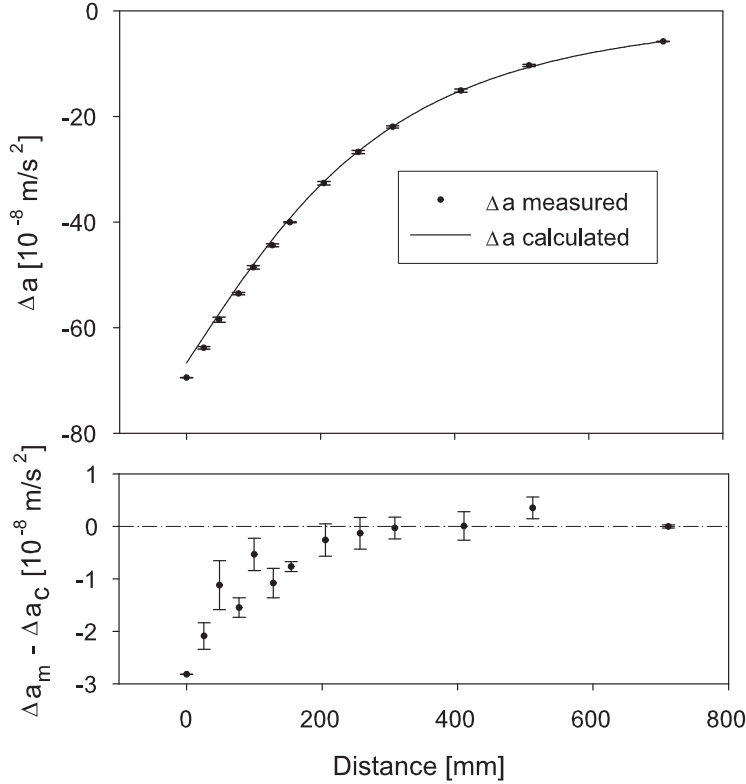


Figure 6.5: Gradiometer phase as a function of source mass position is shown in the upper graph. Comparing these measurements with the expected signal shows a pronounced departure for short distances shown in the lower graph. The two curves are forced to overlap at the distant point under the assumption that systematic shifts are largely diminished there.

systemic path of this error. Another source of error is a residual sensitivity to the aforementioned sensor tilt about the Raman axis which arises from differential projections onto \mathbf{g} from beam steering optics as described in section 3.5 and demonstrated in section 6.4. In this experiment the sensitivity is known to be $\delta_\phi^{gg}/\delta_\theta^{roll} \approx 150 \text{ rad/rad}$ which drives an important 0.5 mrad phase shift for the measured tilt. It is notable that we have previously demonstrated that these sensitivities can be reduced with corrective wedges. However, new Raman windows without wedges are preferred. On the other hand, the driver can be avoided altogether by mounting the source masses on an elevated rail system with anchor points far from the sensors.

We have also considered the effect of shot-to-shot fluctuations in launch angle but this falls well below the noise floor. Long term drifts of this angle may be monitored by the baseline measurement described in section 6.3. Other typical systematic effects remain which are associated with source mass density homogeneity and must be considered in the final measurement.

Last we consider accuracy in the scale factor of the measurement due to alignment errors. To suffer an error in scale factor in the interferometer, one must appreciably change k_{eff} . The actual value of k_{eff} is important since $\delta\phi = k_{eff}aT^2$. If there is a misalignment of the two counter-propagating beams (which comprise k_{eff}) by an angle α , then there is a scale factor error of $\frac{1}{2}\alpha^2k_{eff}aT^2$ so the requirement for a 10^{-6} measurement is $\alpha < 10^{-3}$ rad. This is easily attainable in practice. To complete the picture, T must also be known at the 10^{-6} level or 100 nsec in our case which is readily attainable.

6.1.2 Testing the inverse square law

This experiment may also be interpreted as a test of Newton's inverse square law (ISL). In this type of measurement, the spatial dependence of the gravitational field is directly measured to test for violations of the ISL. Violations are typically predicted to arise from the exchange of a massive particle with wavelength $\lambda = \hbar/m_\gamma c$ and give a well known Yukawa potential of the form:

$$U(r) = \frac{Gm}{r} \left(1 + \alpha e^{-r/\lambda} \right) \quad (6.4)$$

where α is the coupling strength of the particle and M is the mass of the source. Our experiment differs significantly from the work of [86] which has very little spatial variation or [26] which has none at all. Although well-suited for measuring G at a specific distance, these experiments must be compared with the value of G at other ranges to test for an ISL violation. The experiment demonstrated here is self-contained in that the signal measured is dependent on the value of G at two different distances.

To look for a violation of the ISL it is convenient to form ratio quantities in which the gravitational constant cancels leaving only the spatial dependence of the force

law [41]. This is because the value of G in Newton's law is not generally equivalent to that used in the Yukawa potential. This is clear when one considers the case of $\lambda \rightarrow \infty$ which results in a $(1+\alpha)$ scale factor for the Yukawa force which must behave like the Newtonian force at short distances. We therefore construct the quantity:

$$\Delta = \frac{a_1 - a_2}{a_2}, \quad (6.5)$$

where the subscripts indicate different positions. In the Newtonian case,

$$a_i = g_i \equiv \frac{GM}{r_i^2}, \quad (6.6)$$

whereas for the Yukawa force, $a_i = g_i + \alpha\tilde{\eta}_i$ where

$$\tilde{\eta}_i \equiv \frac{GM}{r_i^2} e^{-r_i/\lambda} (1 + r_i/\lambda). \quad (6.7)$$

We may then form the constraint

$$\Delta_Y - \Delta_N \ll \sigma_m, \quad (6.8)$$

where the subscripts N and Y refer to the Newtonian and Yukawa quantities respectively and σ_m is the standard measurement error. Solving for α we find:

$$\alpha(\lambda) = \frac{g_2^2 \sigma_m}{g_2 \tilde{\eta}_1 - \tilde{\eta}_2(g_1 + g_2 \sigma_m)}. \quad (6.9)$$

In our experiment we measure relative quantities to eliminate slow drifts in the interferometer phase. We therefore explicitly construct the quantity implied by equation 6.5

$$\Delta = \frac{a_1 - a_2}{a_2 - a_3}, \quad (6.10)$$

where the numerator and denominator quantities are the two measurements in our system. This may also be solved for α to determine an ISL constraint. However, due to the complicated source mass geometry we numerically evaluate the terms in equation 6.8 for comparison with the value of σ_m implied by our precision. Specifically,

in our experiment the Yukawa acceleration is given by:

$$a_y(x) = \sum_i \frac{G_Y m_i y_i}{r_i^3} \left(1 + \alpha e^{-r_i/\lambda} \left(1 + \frac{r_i}{\lambda} \right) \right), \quad (6.11)$$

where $r_i = (x_i^2 + y_i^2 + z_i^2)^{1/2}$ while the Newtonian acceleration is given by equation 6.3.

Figure 6.6 shows parametric curves for which equation 6.8 would be satisfied for our device, along with the present limits from [43, 42]. A 2σ statistical constraint of 8×10^{-3} suggests that this experiment is within a factor of five of improving the limits on α near $\lambda = 20$ cm. Note that in this calculation the demonstrated experimental precision of 0.02 mrad is reasonably assumed to hold at an intermediate point (i.e. a_2). The position of the intermediate point is chosen theoretically so as to minimize the attainable constraint on α . This amounts to locating the intermediate point at $x = 10$ cm which gives roughly one-half of the signal.

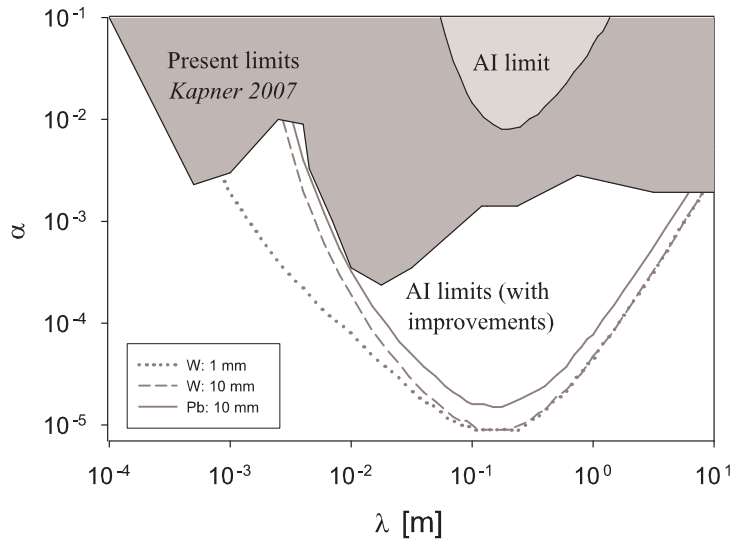


Figure 6.6: Statistical Yukawa constraint using 2σ confidence bounds is compared with the present limits from [42, 43]. Atom interferometry (AI) could be used to constrain α at the 8×10^{-3} level for λ near 20 cm. Limits exceeding the 10^{-5} level are feasible (see Fig. 6.7). Both Lead (Pb) and Tungsten (W) are considered.

The large discrepancy between the optimal 1.2×10^{-3} precision and the 8×10^{-3} constraint shown in 6.6 arises from the reduced resolution of the far points, a result of the reduced signal. This can be clearly seen with a simple example. For a point source we can consider the absolute field measurements at two mass positions such that

$$\begin{aligned} a_1 &= g_1(1 + \alpha), & \text{for } r_1 \ll \lambda \\ a_2 &= g_2, & \text{for } r_2 \gg \lambda. \end{aligned} \quad (6.12)$$

Then,

$$\Delta_Y - \Delta_N = \frac{\alpha g_1}{g_2} \leq \sigma_\Delta \quad (6.13)$$

This quantity is constrained by the absolute measurement precision σ_m which we consider for two cases:

$$\sigma_\Delta \approx \begin{cases} \frac{\sqrt{2}\sigma_m}{g}, & \text{for } g_1 \approx g_2 \\ \frac{\sigma_m g_1}{g_2^2}, & \text{for } g_1 \gg g_2 \end{cases} \quad (6.14)$$

This implies that:

$$\alpha \leq \begin{cases} \frac{\sqrt{2}\sigma_m}{g}, & \text{for } g_1 \approx g_2 \\ \frac{\sigma_m}{g_2}, & \text{for } g_1 \gg g_2, \end{cases} \quad (6.15)$$

which makes clear the fact that the constraint is limited by the weakest signal. The experiment discussed above operates at a point between these two extremes and is therefore not optimal. In fact, in an experiment of this type, it is common practice to increase the source mass with increasing position, such that the field from each position is the same [41]. Another approach is to construct the source as an approximation to an infinite half-space with thickness $d \approx \lambda$ [87]. In this case the Newtonian field is independent of distance from the mass according to $2\pi G\rho d$ but the putative Yukawa field still falls off according to:

$$\mathbf{F}(\mathbf{r}, \lambda) = \hat{z} 2\pi \rho \lambda G e^{-|z|/\lambda}, \quad (6.16)$$

as shown in [41].

We therefore analyze an improved experiment along these lines to determine the potential performance of our device. The proposed setup is shown in Figure 6.7 which essentially gives a comparable Newtonian signal for both mass configurations

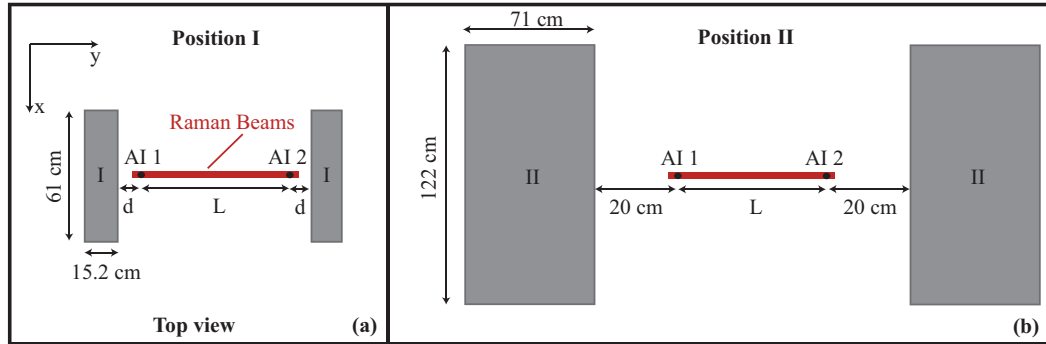


Figure 6.7: Proposed mass-sensor configuration for an improved ISL measurement. The source masses are chopped between a null position and configuration I or II, (a) and (b) respectively. The height (not shown) is chosen to be identical to the setup in Figure 6.1. The parameter d represents the distance of closest approach to the atoms and L is chosen to be much larger than the spatial extent of the source masses.

which in itself doubles the Yukawa constraint. Furthermore, the overall signal is enhanced due to the increased source mass size and proximity while sensitivity of the Newtonian signal to positioning is suppressed due to the large spatial extent of the masses orthogonal to the measurement axis. Figure 6.6 shows the statistical limits from this proposed configuration for several cases including $d=10$ mm for Lead (Pb) and Tungsten (W) and 1 mm for W. The density of W which is 70% larger than that of Pb effectively doubles the constraint on α by enhancing both the Newtonian and Yukawa signal. Bringing the source to a distance of 1 mm from the atoms represents a significant experimental challenge but also significantly improves the constraints at small λ . Improvements can promptly provide a significant measurement at the 10 cm length scale and may in fact exceed the 10^{-5} level.

At this proposed precision level, many sources of error can limit the accuracy. Possibilities include those discussed in section 6.1.1 as well as edge effects from the finite source mass extent, surface flatness and launch angle with respect to the source mass surface. Furthermore the extended baseline will place additional constraints on the frequency stability of the Raman laser which scale with baseline. Improvements to both the source mass and source mass modeling will be necessary for these measurements.

6.2 Time-dependent potential

An unexplored aspect of light pulse atom interferometry is the response of the interferometer to a time-dependent potential. As discussed in section 3.4, the phase response is largely dictated by the laser phase since no asymmetry is imposed between the two interferometer arms. Here we present the details of our experiment with a dynamic field.

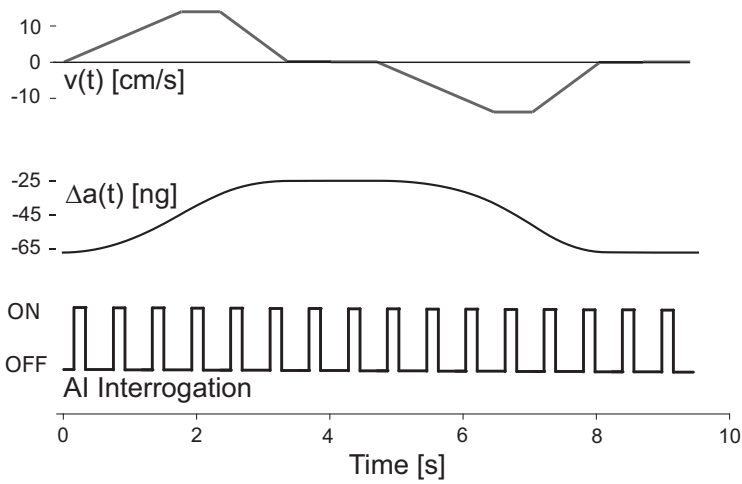


Figure 6.8: Timing diagram for the time-dependent potential showing the velocity profile of the source masses with the resultant differential gravity signal along with the timing of the 16 interrogation pulses. This sequence is repeated many times and points of identical conditions are binned to measure the phases.

Measuring the phase shift for a dynamic potential requires a carefully designed experiment. At present our system relies on ellipse fitting to extract the differential phase which requires several data points taken under identical conditions (see section 5.2.1). Therefore, we use a precisely controlled motion profile for the source mass which is synchronized with the gradiometer measurement cycle. An example of the source mass velocity profile along with the gradiometer measurement timing diagram is shown in Fig. 6.8. This sequence is repeated 10 times to give 10 points at each of 16 conditions from which to fit 16 ellipses. This is followed by a necessary rest period during which the motion system cools while a reference point is taken. The reference point serves to monitor slow drifts in the phase which we subtract from the

dynamic points. This entire sequence is repeated and the results at each condition are analyzed with an Allen standard deviation to determine the uncertainty of each point.

The results of the analysis are shown in Fig. 6.9. In this figure the measured phase is plotted versus the time rate of change of the gravity field. The points near the two extremes coincide with low velocity motion whereas the interior points are the most dynamic. Changes in the acceleration as large as 4 ng over the interferometer duration or 23.5 ng/s are imposed by this experiment. The expected signal is linear according to $\delta\phi \approx \partial_t(\Delta a) + \dots$ as shown in section 3.4. The measurements are in good agreement with the expected signals. Increased precision is required to resolve the nonlinear contributions.

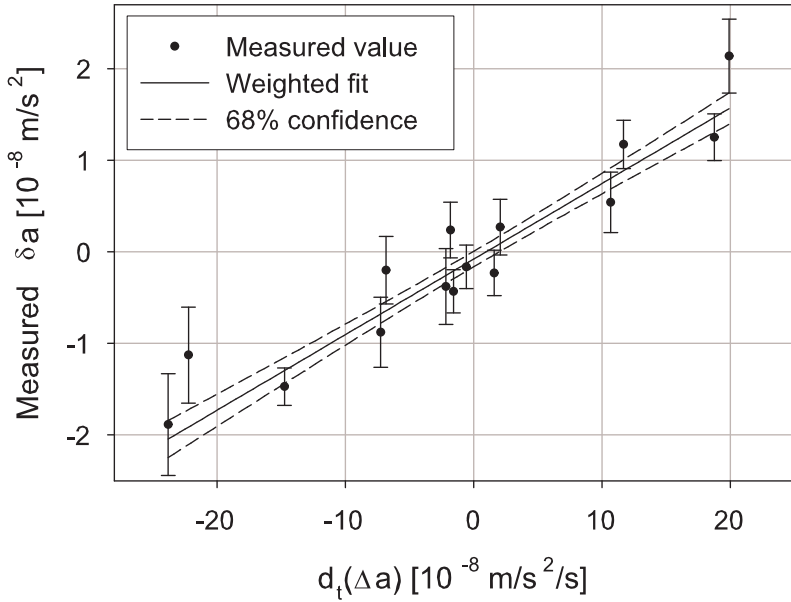


Figure 6.9: Gradiometer response to a time-dependent potential. The data represents only the effect of the dynamic field during the interferometer. The fit is shown with 68% confidence bounds demonstrating that the results agree with theory to within $1-\sigma$ for field changes as large as 23.5 ng/s.

6.3 Baseline measurement

As discussed first in [24] and later in more detail by [85], the interferometer phase is sensitive to the single photon Raman detuning dynamics during the interrogation (i.e. detuning of the Raman beam from the $6^2P_{3/2}$ excited state). This is often a limiting source of noise in light-pulse atom interferometers if the frequency noise of the Raman laser is too large. We present here the results of a test which clearly illustrate this point and show how this sensitivity may be used to precisely measure the distance between the interferometers – an important measurement in precision gravity tests.

In the case of the gradiometer, the relative acceleration or phase is measured by an optical ruler spanning the distance between the two sensors. Ideally, this wavelength is constant throughout the measurement. If the wavelength is time-dependent according to the detuning dynamics shown in figure 6.10, the differential phase will exhibit an additional shift proportional to the sensor baseline and the change in the single photon Raman detuning δ_R . More precisely, since the single interferometer phase shift is given by $\delta\phi = \phi_1 - 2\phi_2 + \phi_3$, the two gravimeters see a different change in the optical phase for the second pulse which appears in the difference phase according to $\Delta\phi = 2\delta k_{\text{eff}} L$ where $\delta k_{\text{eff}} = 4\pi\delta\nu/c$.

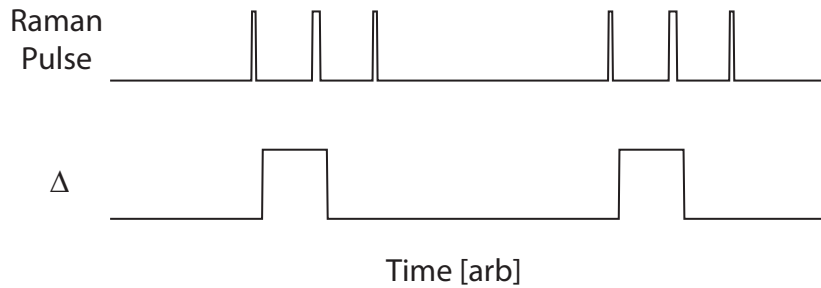


Figure 6.10: Raman laser frequency chop timing diagram. Dynamics in the Raman laser frequency during the interferometer lead to shot-to-shot gradiometer phase errors.

We follow this algorithm for $\delta_R=1.161$ MHz which gives a phase shift of 71.57 mrad (see Fig. 6.11). With several hours of averaging a measurement of $L = 73.56 \pm$

0.09 cm is obtained for the optical path length between the gravimeters. A subtlety exists in that one must consider the non-unity index of refraction of the vacuum cell windows between the sensors. Taking this into consideration, we determine a spatial MOT separation of $L = 72.29 \pm 0.09$ cm which agrees with our physical measurement of 72.39 ± 0.25 cm within uncertainty limits.

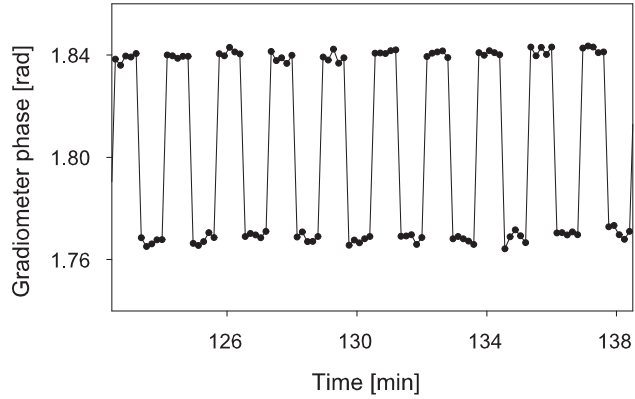


Figure 6.11: Resulting gradiometer phase when alternating between the detuning dynamics in figure 6.10 and the static case.

A secondary source of error arises from the windows. Each interferometer experiences a phase shift proportional to the Raman beatnote detuning due to the AC-Stark effect since the excited state couplings from the $F = 3$ and $F = 4$ levels are not identical for a given Δ . This shift is at the 1 mrad/MHz level and would normally cancel in a gradiometer. However, we find a rather large window attenuation between the sensors of $\approx 7\%$ due to poor AR-coatings. Therefore, the AC-Stark shifts in each sensor differ by 7×10^{-2} which results in a differential error of ≈ 0.07 mrad/MHz level. In the present case, this error is beneath our resolution but should be considered for future measurements.

It is interesting that this measurement can be significantly improved. Simply increasing the detuning and averaging duration can readily achieve a 10^{-5} level measurement. Furthermore, increasing the SNR or enhancing the sensitivity with large momentum transfer for precision gravity work will directly enhance this measurement as well.

6.4 Tilt sensitivity

An unexpected effect of static beam deviations between the two sensors is a proportional tilt sensitivity. In our system these static deviations are the result of wedged windows which provide the Raman beam access to the atoms. As mentioned above, this systematic shift is important for measurements of the gravitational constant, where the large source masses depress the floor and cause the gradiometer to tilt resulting in a differential phase shift proportional to the tilt. It is at first surprising that this sensitivity is most pronounced in platform roll rotations which we define as rotations about the Raman beam axis or \mathbf{k}_{eff} . However, consider the case where \mathbf{k}_{eff} deviates transversely by an angle α_{Dev} between the interferometers (here transverse is defined as orthogonal to both \mathbf{k}_{eff} and \mathbf{g}_z). Then a small roll θ_{Roll} of the supporting platform results in a first order projection of one sensor axis onto \mathbf{g} while the other remains unchanged. This then results in a differential phase shift that appears as a change in the measured gradient according to $\delta\phi_{Roll} = k_{eff}\theta_{Roll}\alpha_{Dev}gT^2$. On a moving platform this systematic is highly relevant and we have shown that this effect can be largely reduced by inserting a counteracting wedge in the beam path between the sensors.

Figure 6.12 shows the output of a $T = 43$ ms gradiometer as the platform is stepped to different angles about the Raman axis. This system demonstrates a 167 rad/rad sensitivity which is proportional to the transverse projection of the net optical wedge between the sensors. Therefore, this indicates a beam deviation between the interferometers of $600 \mu\text{rad}$ in the transverse direction. It is interesting to consider this system as a precision grade, high accuracy tilt sensor. For our current interrogation time of 85 ms, a slightly larger 1 mrad wedge would result in a sensitivity of 1100 rad/rad. With our current noise level of $4.3 \text{ mrad}/\sqrt{\text{Hz}}$, a tilt sensitivity of $4 \mu\text{rad}/\sqrt{\text{Hz}}$ could easily be realized. On the other hand this should be compared with the performance potentially available with a $20 \text{ ng}/\sqrt{\text{Hz}}$, horizontal gravimeter implementation of an atom interferometer. This instrument would be first order sensitive to deflections from vertical and giving $20 \text{ nrad}/\sqrt{\text{Hz}}$ which is far superior.

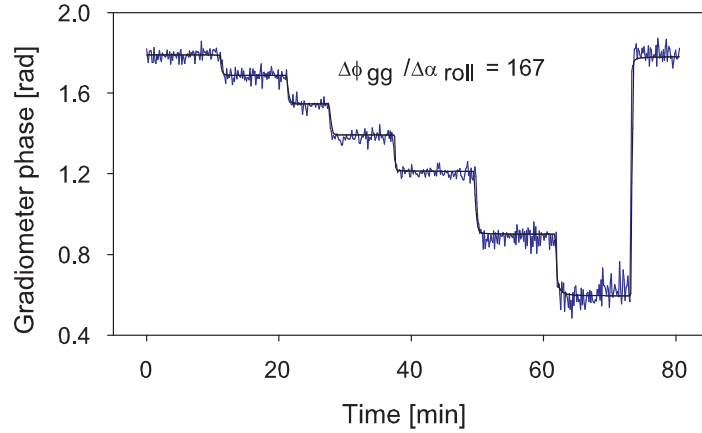


Figure 6.12: Gradiometer tilt sensitivity. Wedged optics between the interferometers allows differential projections of the sensor axes onto \mathbf{g} . Here, a $T = 43$ ms gradiometer demonstrates a sensitivity of 167 rad/rad as the platform is stepped to different roll angles about the Raman axis. The line is the scaled output of a calibrated tilt sensor demonstrating the linearity of the effect.

6.5 SNR discussion

Tests of the detection system indicate that a phase noise less than 1 mrad/shot is possible in the long fountain configuration. However, reductions in signal size due to Raman pulse efficiency cause additional noise and linearly reduce the fidelity of the system. Furthermore, the use of ellipse-specific phase extraction techniques may introduce additional noise due to slow phase drifts in the gradiometer output. In fact, our current noise floor of $3.1 \text{ mrad}/\sqrt{\text{Hz}}$ corresponds to only 5 mrad/shot or 200:1. As in section 5.1.2 the scaling of SNR with atom number can determine limiting mechanisms. However, this technique does not reveal the shot-noise limited performance when other noise sources dominate. To directly characterize the optimal performance of the gradiometer we compare two interferometers with vastly different interrogation times, yet comparable contrast. Reducing the interrogation time removes the sensitivity to noise sources in addition to those associated with reduced contrast. This sets a relevant benchmark for the shot-noise limited performance of the long T interferometer.

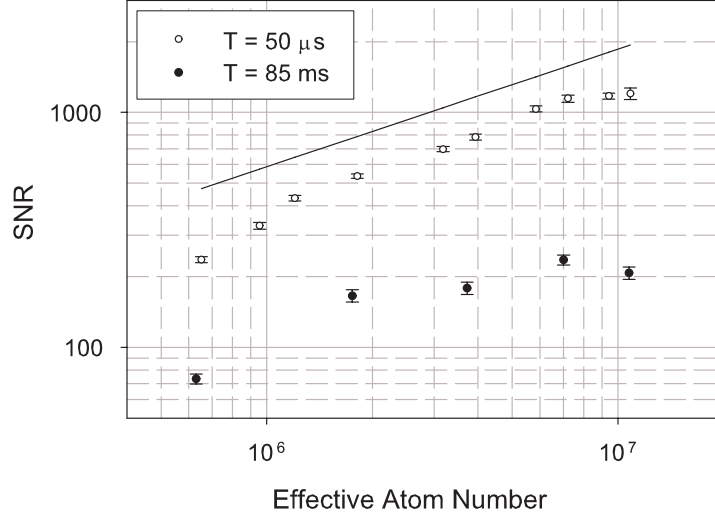


Figure 6.13: Comparison of SNR for $T = 85$ ms and $T = 50\ \mu\text{s}$ interferometer. The short T interferometer indicates that the gradiometer can be improved before reaching atom shot noise limits. The line indicates the expected atom shot-noise limited SNR based on the measured atom number with a 60% contrast.

In figure 6.13, the phase noise of two interferometers is measured as a function of atom number. The $T = 0.05$ ms interferometer has a 4×10^{-7} reduced sensitivity to inertial noise compared to the $T = 85$ ms. This allows direct phase extraction in the same manner described in section 5.1 which avoids noise sources associated with ellipse fitting such as contrast noise. It is clear that the $T = 85$ ms interferometer is not shot noise limited as the SNR is roughly constant above 10^6 atoms. On the other hand, the $T = 0.05$ ms interferometer demonstrates a $N^{1/2}$ dependence on atom number characteristic of quantum projection noise [78]. From this analysis it is clear that a 5-fold SNR increase is possible with current atom numbers.

The above results also suggest that additional SNR improvements will come from enhanced contrast once the atom shot noise limit is attained. We therefore investigate the current contrast limits of the interferometer. We consider first the Rabi frequency by analyzing the contrast envelope size as a function of Raman pulse length.

An interesting facet of light pulse interferometers is the fact that the atoms in the two interferometer arms separate well outside their coherence length. This is due to

the large recoil velocity imparted to the atoms via the 2-photon optical transition. Probably the most compelling evidence of this is a test in which one scans the starting time of the last pulse in a three-pulse sequence. This pulse is responsible for combining the wavepackets or closing the interferometer loop. The timing of this pulse sets the overlap of the wavepackets from the two interferometer arms. The wavepacket separation is given by $\delta\mathbf{x} = \frac{\hbar\mathbf{k}_{\text{eff}}}{m}\delta t$.

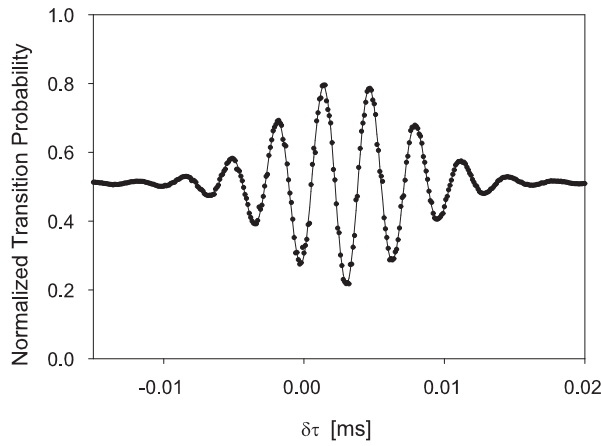


Figure 6.14: Scan showing the interferometer contrast envelope as a function of interferometer timing asymmetry. The line is a fit to the data using a sinusoid with a Gaussian envelope. The offset of the maximum along δt is an artifact of the timing system.

A typical scan of the timing of the last pulse is shown in figure 6.14. The fringe pattern within the contrast envelope is due to a 1 MHz detuning of the Raman oscillator during the dark time between the last two pulses. This feature ensures an accurate determination of the envelope width. This test reveals a characteristic length associated with the interferometer parameters. Two concerted phenomena determine this length: the atomic coherence length and a velocity-driven inhomogeneous dephasing of the ensemble. In the limit of Rabi frequencies which are much larger than the Doppler profile, this coherence length is set by the atom temperature after launching. At the opposite end, the small Rabi frequency addresses only a narrow velocity class of the atoms resulting in a temperature selection and thus an increase in the coherence length. A secondary effect contributes as follows. As the delay of the last pulse

is scanned, each atom obtains an additional laser phase shift according to its velocity or $\delta\phi = \mathbf{k}_{\text{eff}} v_{\text{atom}} \delta t$. This arises from $\Delta\phi_{\text{atom}} = \phi_1 - 2\phi_2 + \phi_3$ in which a constant atom velocity cancels only if the pulses are equally spaced in time. This results in a velocity-dependent phase shift which is not uniform across the ensemble and results in a decrease in contrast. The magnitude of this effect is comparable to that of the coherence length.

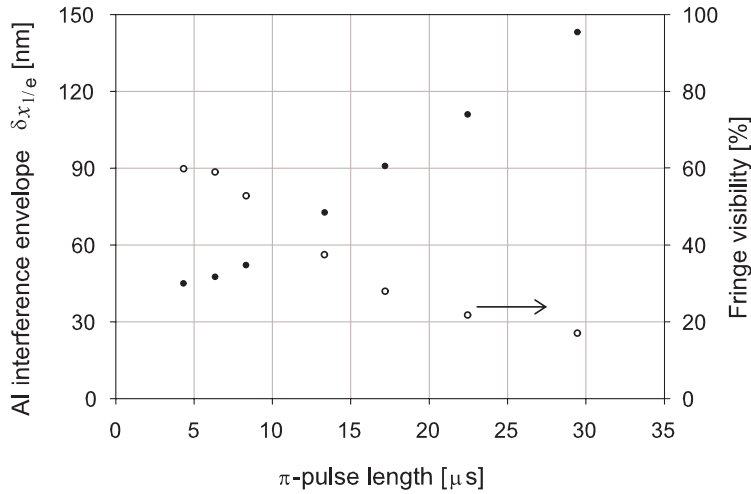


Figure 6.15: Interferometer contrast envelope and fringe visibility as a function of interferometer pulse length. The contrast envelope size is determined by the $1/e$ radius of the Gaussian envelope fit (see Fig 6.14) and the 2-photon recoil velocity. The envelope size approaches a short pulse limit near 45 nm and indicates that with typical pulse lengths $< 5 \mu\text{s}$, the pulses are transform limited.

To characterize our interferometer, this contrast envelope is studied as a function of interferometer pulse length (see Fig 6.15). The contrast envelope size is determined by the $1/e$ radius of the Gaussian envelope fit and the 2-photon recoil velocity. The contrast is determined by the peak-to-peak fringe size at maximum visibility. The envelope size approaches a short pulse limit near 45 nm and indicates that with typical pulse lengths $< 5 \mu\text{s}$, the pulses are sufficiently transform limited. Therefore, possible enhancements to the contrast include increased beam size which offers greater intensity homogeneity and larger single-photon Raman detunings which will decrease losses via spontaneous emission. Both improvements will require increased Raman

beam power.

The aforementioned beam parameters are a function of atom temperature. In our apparatus, the apparent temperature decreases with increased fountain duration. This is due to a finite detection volume which effectively apertures the velocity profile by preferentially detecting cold (slow moving) atoms. This points to a deficiency in the sub-Doppler cooling stage which remains to be investigated. Alleviation of this problem will naturally enhance the atom number and correspondingly increase the SNR. It is interesting that the aforementioned effects behave differently in the context of a detection aperture. The coherence length is a strict function of the position uncertainty due to either the Raman pulses or momentum uncertainty after sub-Doppler cooling. This represents a true indicator of the de Broglie wavelength of the atom regardless of the effective cloud temperature due to a detection aperture. However, the ensemble dephasing will appear to subside in the presence of restrictive detection and gives a better indicator of the atom interferometer performance in terms of contrast and SNR. More investigation is required to delineate the exact contributions of both effects in our system.

Chapter 7

Zero-dead-time technique

The need for accurate time/frequency standards has existed for many centuries. The development of atomic frequency standards in the 1950's revolutionized the field of precision time-keeping by providing a new absolute frequency reference (the atom). Since then, many technical and scientific advances have improved the sensitivity of atomic frequency standards, from the first Cs clock with a sensitivity of 1 part in 10^{10} (Essen) [88] to the current time standard NIST F-1 operating at 1 part in 10^{15} [89]. Atomic frequency standards are now commonplace in the most demanding scientific and commercial applications. Accurate frequency measurements form the basis for tests of scientific theories including quantum mechanics, QED, and general relativity [33].

In general, the sensitivity of these atomic clocks scales with the interrogation time. The first atomic frequency standards were atomic clocks based on thermal atomic beams, for which the interrogation time is limited by technical issues such as the high velocity of the atoms and vacuum chamber size. The development of laser cooling and trapping techniques for cold atoms enabled atomic fountains characterized by long interrogation times, greatly improving the sensitivity of atomic frequency standards. To further improve sensitivity, optical clocks based on trapped ions and atoms have been developed to take advantage of higher frequency optical transitions.

7.1 Dick effect

These atomic clocks all rely on locking a local oscillator (LO) to an atomic reference. To do so they make discrete measurements of the atomic phase, and correct the LO accordingly. Due to technical issues such as atom loading time and detection, there is some dead time between consecutive measurements. If phase noise is present in the LO, the system does not track it during the dead time and the associated temporal knowledge is lost. This noise accumulates over time, leading to phase drifts in the LO relative to the stable atom reference. This inter-modulation error is known as the Dick effect.

The Dick effect manifests itself in a microwave atomic clock through phase noise in the microwave source. In optical atomic clocks, phase noise due to laser linewidth and optical delivery contribute to the Dick effect [90]. Noise in the optical delivery is problematic if not properly controlled [91]. Mechanical jitter in the optical components as well as index of refraction noise in the delivery system create spurious phase shifts of the light driving the transition analogous to phase noise in the LO [92]. Periodic sampling of this noise not only introduces unnecessary error into the accuracy of the clock, but also diminishes the averaging performance against the benchmark of the 2-sample Allan standard deviation.

No LO is perfectly stable over even a short amount of dead time; the only way to entirely avoid long-term drifts due to the Dick effect is to track the LO phase relative to the reference (atom) continuously. To this end, groups have suggested continuous phase measurements through the use of a continuous fountain [93]. In contrast, we demonstrate an uninterrupted sampling technique in a conventional microwave fountain clock which mitigates errors due to phase noise in the LO. This technique alternately monitors two atomic clocks using the same LO.

In atomic clocks, a unit of time is defined by a prescribed number of cycles in an LO which is frequency locked to an atomic resonance. For example, in a Cesium fountain clock, a microwave oscillator is tuned to the $|F = 3, m_F = 0\rangle \rightarrow |F = 4, m_F = 0\rangle$ hyperfine resonance at 9.192 GHz. In principle, the measurement differences the phase of the LO with that of itself a time T earlier by referencing the atom's pristine

internal oscillator [80]. The atomic transition probability serves as the frequency discriminator for corrective feedback to the LO, and is given by $P = \frac{1}{2}[1 + \cos(\Delta\phi)]$ where

$$\begin{aligned}\Delta\phi &= \phi^{LO}(t+T) - \phi^{LO}(t) - \omega_0 T \\ &= \int_t^{t+T} (\omega(t') - \omega_0) dt'.\end{aligned}\quad (7.1)$$

In this expression ω_0 is the atomic resonance frequency, and $\omega(t')$ is the frequency of the LO at time t' .

During the dead time between these measurements the LO phase is unmonitored by the atoms and thus free to wander. This dead time consists primarily of technical processes such as atom sample preparation and detection. The effect this has on measurement accuracy can be seen in the cumulative phase knowledge which reveals the missing phase information. Equation 7.2 gives the cumulative phase error resulting from the Dick effect.

$$\Phi = \sum_{n=1}^{N-1} (\phi_{2n+1}^{LO} - \phi_{2n}^{LO}) + \sum_{n=1}^N \delta\phi_n^m \quad (7.2)$$

In this equation $\phi_{2n+1}^{LO} - \phi_{2n}^{LO}$ is the phase error accumulated during the dead time following the n^{th} clock measurement, $\delta\phi_n^m$ represents the noise in the n th measurement, and $N \equiv \tau/T_c$ is the total number of measurements, where τ is the time duration of the data set and T_c is the cycle time. The error accumulated during these open windows of time is a ubiquitous problem for current time standards and the subject of much discussion [94, 95].

Efforts to fight this effect in atomic clocks include minimizing the cycle dead time, using LO's with outstanding short term stability and, in the context of optical clocks, actively canceling the delivery noise [93, 96]. Several labs have demonstrated unparalleled performance by careful attention to these parameters [62, 97, 92]. Continuous fountains have also been shown to reduce errors due to the Dick effect for specific modulation frequencies [98, 99].

7.2 Interleaved clock

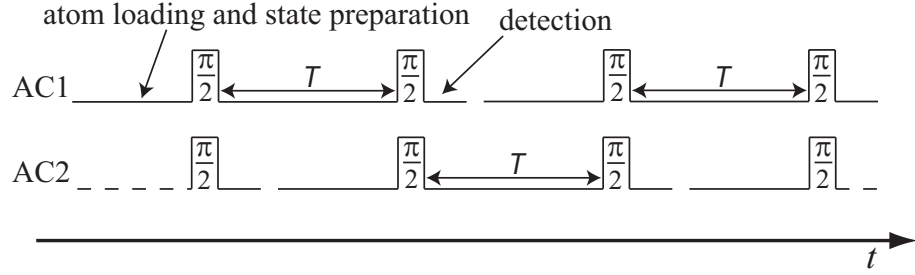


Figure 7.1: Pulse sequence timing diagram of a ZDT implementation. Two atomic clocks (AC1 and AC2) interrogate a common LO in an alternating fashion to eliminate measurement dead time.

In contrast to these approaches, Dick et. al. proposed a scheme involving two interleaved clocks to obtain uniform coverage of the time axis [100]. Here, we demonstrate this zero-dead-time (ZDT) technique which employs two identical clocks to alternately monitor the LO in a relay manner and eliminate the Dick effect (Fig. 7.1). The clock outputs form an unbroken chain of measurements linked by common interrogation pulses. The staggered measurements are linked in time by sharing the second $\pi/2$ -pulse of one clock with the first $\pi/2$ -pulse of the following clock.

In this case the two clocks track the spurious shifts due to the LO. In fact, the sum of consecutive measurements cancel contributions from phase noise in the shared pulses, such that the accumulated clock phase inherits only the noise from the first and last $\pi/2$ -pulse in the data run. The cumulative phase error reduces to:

$$\Phi = (\delta\phi_{2N}^{LO} - \delta\phi_1^{LO}) + \sum_{n=1}^{2N} \delta\phi_n^m. \quad (7.3)$$

An important distinction here is the temporal behavior of equations (7.2) and (7.3). In general the 2-sample Allan standard deviation for an oscillator frequency measurement can be written as:

$$\sigma_y(\tau) = \frac{\delta\phi(\tau)}{2\pi\nu_0} \frac{1}{\tau\eta}. \quad (7.4)$$

In this equation, ν_0 is the resonance frequency of the atomic system, τ is the integration time, $\eta = T/T_c$ is the duty cycle, and $\delta\phi(\tau)$ is the time dependent random walk phase error.

In the case of a single clock with dead-time, the shot-to-shot phase noise from the oscillator as well as white measurement noise average as $\tau^{-1/2}$ since $\delta\phi(\tau) \propto \sqrt{\tau}$. With ZDT, in the limit where $\sigma_{\Delta\phi} \gg \sigma_m \equiv \langle (\delta\phi^m)^2 \rangle^{1/2}$, $\delta\phi(\tau) \sim 0$ and the phase noise averages faster as $1/\tau$.

$$\delta\phi(\tau) = \begin{cases} \left[N\sigma_{\Delta\phi}^2 + N\sigma_m^2 \right]^{1/2} & \text{One Clock} \\ \left[\sigma_{\Delta\phi}^2 + 2N\sigma_m^2 \right]^{1/2} & \text{ZDT} \end{cases} \quad (7.5)$$

In this equation, $\sigma_{\Delta\phi}$ is the shot-to-shot noise in the clock measurement due to phase noise on the LO while σ_m is the RMS measurement noise, which is limited by atom shot noise.

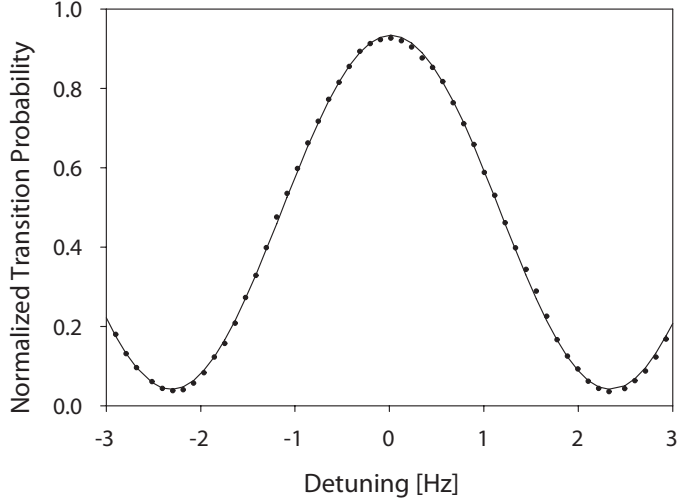


Figure 7.2: Microwave clock fringe with $T=215$ ms in the absence of additive phase noise. The detection system has been validated to perform at 1.2 mrad per shot in this experiment, however the noise in the microwave frequency chain limits the performance to 33 mrad per shot. At a 2.3 Hz repetition rate this corresponds to a frequency stability of $1.8 \times 10^{-12}/\tau^{1/2}$.

7.3 Demonstration

As a demonstration, we operate two independent compact Cesium fountain clocks in the ZDT mode described above. Each clock references a common LO (Oscilloquartz OCXO 8607-BGE) but possesses its own fountain control hardware. Each clock sequence proceeds as follows. We prepare a $2 \mu\text{K}$, 3 mm $1/\text{e}^2$ radius cloud of $\sim 10^7$ Cesium atoms in the $6^2S_{1/2} |F = 3, m_F = 0\rangle$ hyperfine ground-state moving upward at 1 m/s using standard atom fountain techniques. The cloud follows a 6.5 cm vertical fountain trajectory in vacuum during which a microwave $\pi/2 - \pi/2$ Ramsey sequence on the $|F = 3, m_F = 0\rangle \rightarrow |F = 4, m_F = 0\rangle$ clock transition is applied to the atoms with an interrogation time of $T = 215$ msec. We ensure the link between two consecutive clock measurements by gating the microwave excitation of both clocks with a common switch. After the final pulse, the atoms fall into the detection region near their point of origin. We employ a normalized fluorescence detection technique to determine the clock transition probability regardless of atom number by simultaneously detecting the number of atoms in both states which reduces sensitivity to detection laser noise [48]. This method is capable of atom shot noise limited signal to noise ratios approaching 8000:1 per shot. The interferometer is operated with a repetition rate of 2.3 Hz, with the sequence timed such that the dead time matches the interrogation time T .

The LO is tuned to the side of the fringe to maximize sensitivity to phase fluctuations (Fig. 7.2). The contrast of the fringe is limited by inhomogeneous microwave fields in the delivery geometry. A systematic offset of ≈ 200 mrad exists between the two atomic clock fringes due to a larger bias field in one clock and the aforementioned inhomogeneities in the microwave delivery geometry. We set the frequency of the LO to be the average of the fringe centers of the two clocks and post-process the data to correct the resulting DC offset. The transition probability represents the phase accrual of the LO with respect to the atoms over time T . Phase noise in the fringe is due primarily to noise from the microwave electronics at the $1.8 \times 10^{-12}/\tau^{1/2}$ level which corresponds to 33 mrad per shot. The detection noise of each clock is negligible in this experiment. The clocks are designed specifically to be used as light pulse

atom-interferometry based accelerometers and are therefore not intended to approach the accuracy capabilities of current time standards.

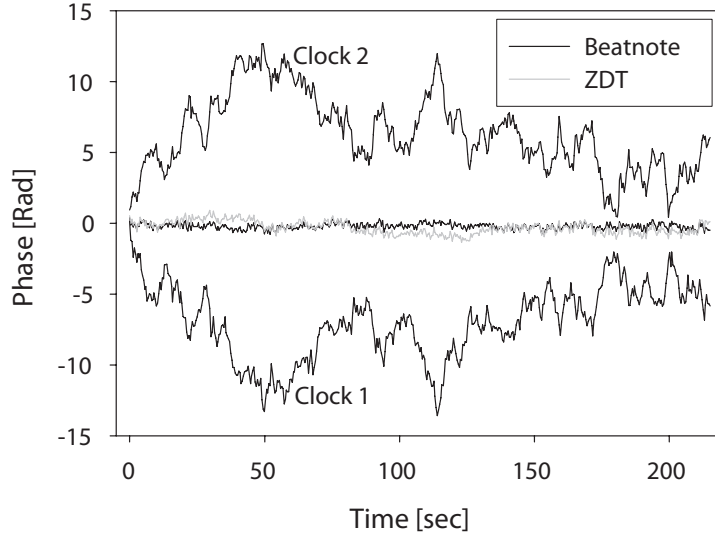


Figure 7.3: Cumulative phase accrual of the two clocks demonstrating perceived phase drift of the LO due to incomplete sampling of the phase noise. The sum of the two clocks represents the ZDT quantity which largely removes the random walk drift and closely approximates the beatnote-predicted behavior. The ZDT method demonstrates only 440 mrad RMS total phase drift over the entire data set.

To demonstrate the features of this method, we overwhelm the intrinsic LO noise by adding $\sigma_{\Delta\phi} = 300$ mrad RMS phase noise to the precision oscillator with a single-sideband mixer. The precision oscillator provides a reference against which we measure the phase accrual of each independent clock in the presence of this large noise. We track the phase of the field witnessed by the atoms by comparing the perturbed signal to that of the quiet LO. To accomplish this, we add a 1 kHz frequency offset to the LO and analyze the beatnote in the time domain by digitally sampling the signal at 20 kHz and tracking the zero crossings to determine the phase [101]. Figure 7.3 shows the phase accrual of each clock as well as the beatnote prediction and ZDT output, which is simply the sum of the two clocks. For this comparison, the aforementioned phase offset between the two clocks must be managed with the addition of a constant value to one clock output which is determined by linear regression of the

cumulative phase. Secondly, another constant value is added to the ZDT quantity to match the slope of the beatnote cumulative phase. Both fits are only for illustration purposes and do not represent a fundamental limit for the utility of the technique.

The partial sampling of the LO phase noise by the individual clocks results in a random walk of the accrued phase at the rate of $\approx 0.5 \text{ rad/s}^{1/2}$ which conforms to the expected value. The ZDT behavior closely mimics the beatnote predicted shot-to-shot phase behavior at the level of 50 mrad RMS. In contrast to the random walk exhibited by the independent clocks, the cumulative ZDT phase is limited to 440 mrad RMS over the entire data run; a factor of 15 reduction in the Dick effect error. The residual drift of the ZDT output is driven primarily by uncorrelated noise between the two clocks at the 50 mrad per shot level which is introduced by the microwave delivery system.

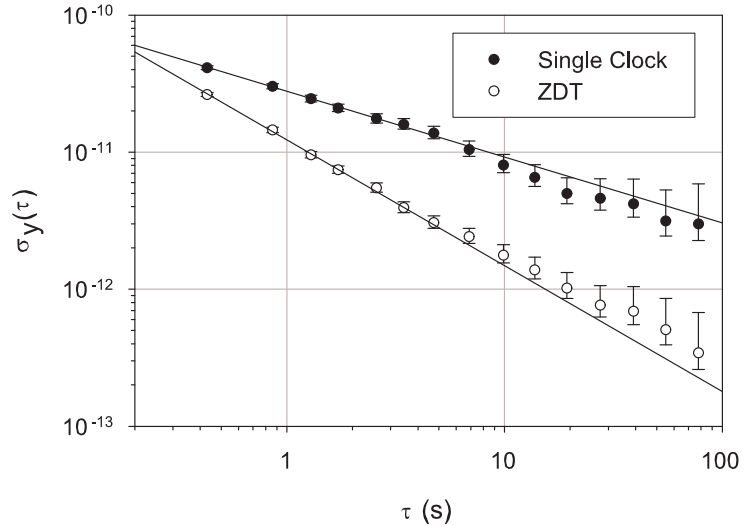


Figure 7.4: Two-Sample Allan standard deviation of individual and ZDT clock behavior in the presence of additive phase noise. The ZDT phase fluctuations integrate as $1.2 \times 10^{-11}/\tau^{0.92}$ characteristic of phase noise while the single clock integrates as $2.8 \times 10^{-11}/\tau^{0.48}$. Uncorrelated noise between the two clocks limits the noise floor at 8×10^{-13} for times less than 100 seconds. For longer times, the noise floor is dominated by the microwave frequency chain.

We further characterize the ZDT implementation with an Allan deviation of both

the single clock and the ZDT clock. The single clock averages at $2.8 \times 10^{-11}/\tau^{0.48}$ which is characteristic of white frequency noise due to the Dick effect (Fig. 7.4). In contrast, the ZDT averages nearly linearly as $1.2 \times 10^{-11}/\tau^{0.92}$ due to the complete knowledge of the phase noise. The ZDT output quickly integrates to the noise floor of the delivery system of 8×10^{-13} . This characteristic will enable new application in microwave and optical clocks. Systems with significant short term phase noise can be used to achieve the same long term performance of pristine clocks. For example, in an optical clock, phase noise due to the delivery will average as $1/\tau$, eventually overtaking the long term performance of a system with a phase compensated delivery. Similarly, a microwave clock using this technique may use a more cost-effective, lower quality LO.

Chapter 8

Conclusion

We have shown here the progress toward a compact gravity gradiometer for precision gravitational tests. We have identified and overcome two significant noise sources including laser frequency noise and differential projections onto g which can limit the device sensitivity. The latter is the result of beam steering effects from index of refraction perturbations in the air between the sensors. With these improvements we have achieved a differential acceleration sensitivity of $4.2 \times 10^{-9} g/\sqrt{Hz}$ over a 70 cm baseline. This corresponds to a phase noise of $3.1 \text{ mrad}/\sqrt{Hz}$ inferred per interferometer which is the best performance achieved in such a system. Using this device, we have demonstrated a proof-of-concept measurement of the gravitational constant with a precision of 3×10^{-4} , which is competitive with the present limit of 1×10^{-4} . Improvements can enable uncertainties falling below 10^{-5} . This experiment is also interpreted as a test of the inverse square law which statistically constrains a putative Yukawa type fifth force to 8×10^{-3} near the poorly known length scale of 20 cm. Limits exceeding 10^{-4} appear to be feasible. We have also performed an experiment which tests the atom interferometer in the context of a time-dependent gravity potential. Furthermore, we have demonstrated a technique by which one may temporally link interferometer measurements together to provide continuous sampling. This can be used to eliminate the inertial sensor analog of the Dick effect and has important applications in the fields of optical and atomic clocks.

Appendix A

Characteristic data

Quantity	Symbol	Value (SI)	Ref
Speed of light	c	$2.997\ 924\ 58 \times 10^8$ m/s (exact)	[102]
Planck's constant	h	$6.626\ 0693(11) \times 10^{-34}$ J s	
Boltzmann's constant	k_B	$1.380\ 6505(24) \times 10^{-23}$ J/K	
Cs melting point	T_M	28.44 °C	[103]
Atomic mass	m	$2.206\ 946\ 50 (17) \times 10^{-25}$ kg	[47]
Frequency	ω	$2\pi \cdot 351\ 725\ 718.4744(51)$ MHz	[104]
Wavelength (vacuum)	λ	852.347 275 884(12) nm	
Lifetime	τ	30.499(70) ns	[105]
Natural linewidth	γ	$2\pi \cdot 5.2152(98)$ MHz	
Hyperfine splitting ($6^2S_{1/2}$)	ω_{HF}	9.192 631 770 0 GHz (exact)	
Doppler temperature	T_D	$124.39\ \mu\text{K}$	[63]
Doppler velocity	v_D	8.82 cm/s	
Recoil temperature	T_{rec}	198 nK	
Recoil velocity	v_r	3.52 mm/s	
Saturation intensity	I_{sat}	1.10 mW/cm ²	

Table A.1: Useful constants and relevant Cs D2 properties for the $6^2S_{1/2} \rightarrow 6^2P_{3/2}$ on the $F=4 \rightarrow F'=5$ cooling transition.

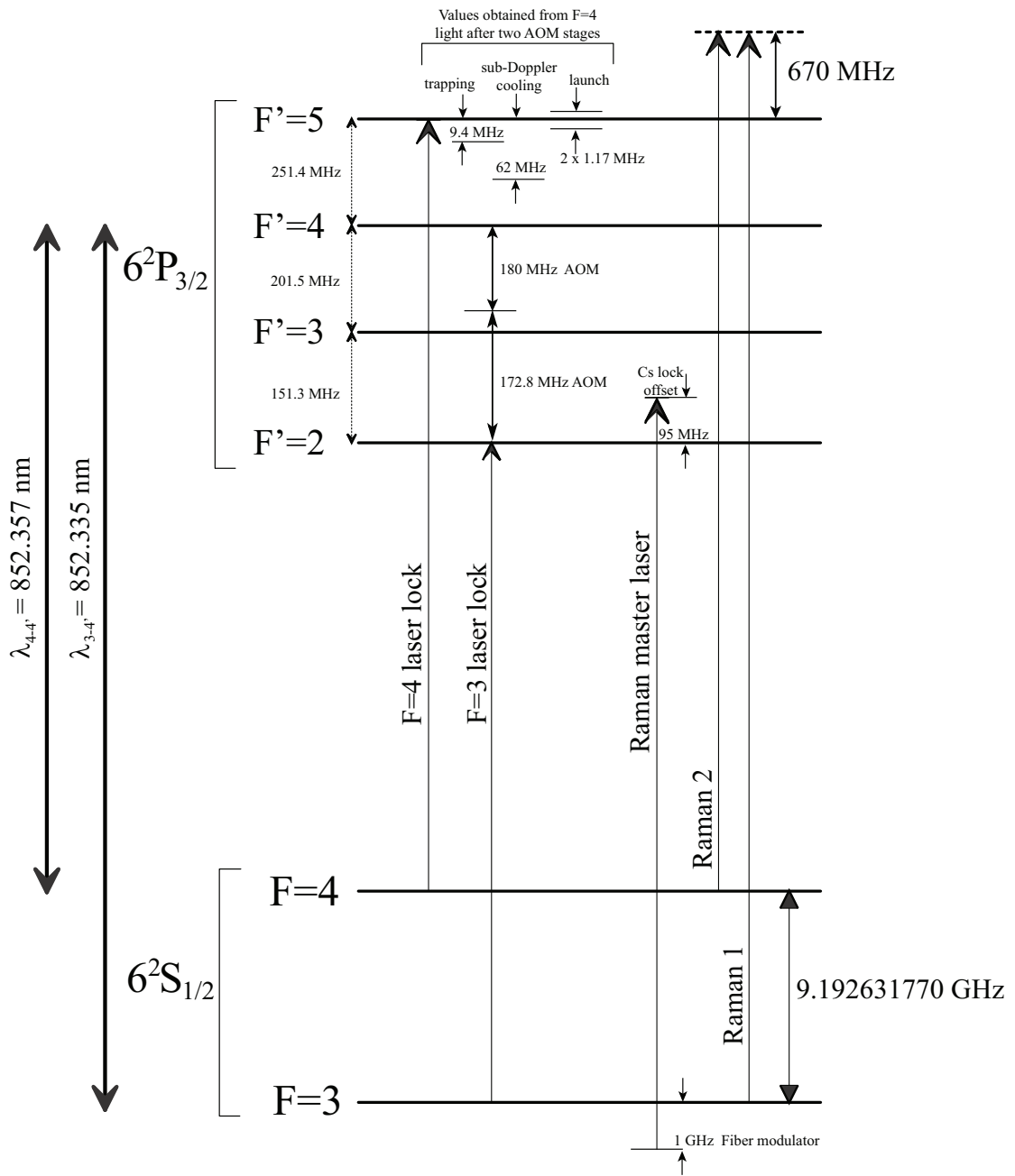


Figure A.1: Cs D2 level diagram and frequency detunings used within the gradiometer apparatus.

Appendix B

Control system photographs

In this appendix the six distinct laser system frames are shown unstacked. The DSP frame controls the measurement cycle while the Sensor frame interfaces with the accelerometers for both control and data acquisition purposes. The Master lasers and electronics generate source light for atom trapping and detection while the Amplifier lasers and electronics provide bright, switchable power.

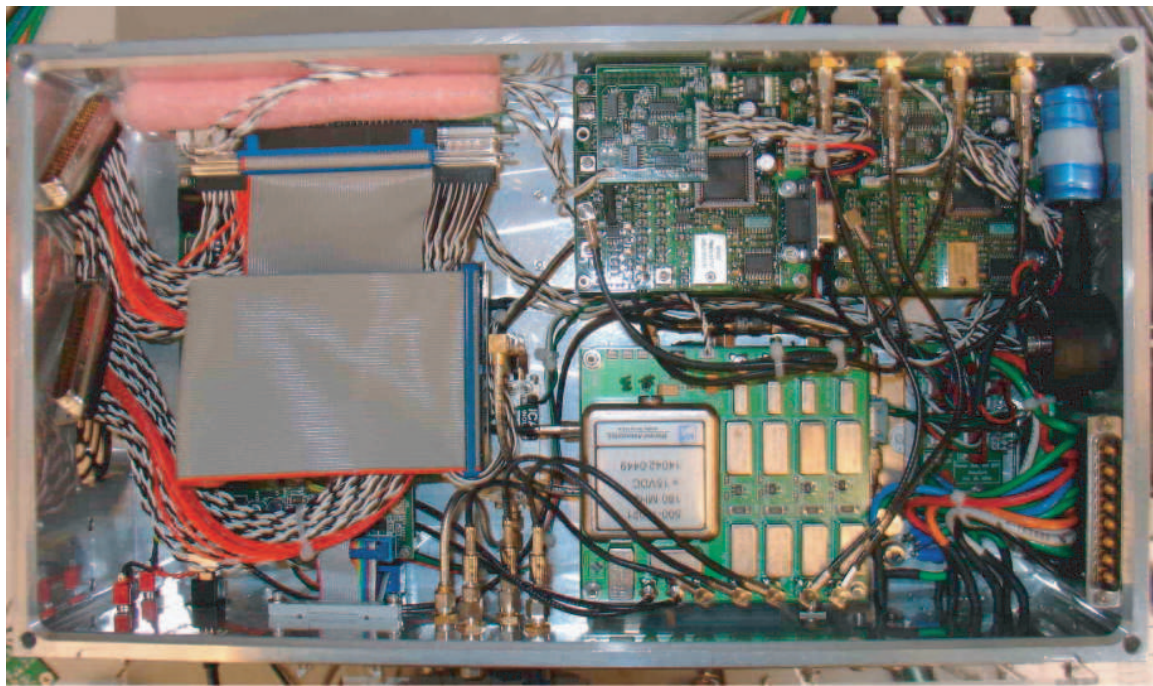


Figure B.1: DSP frame.

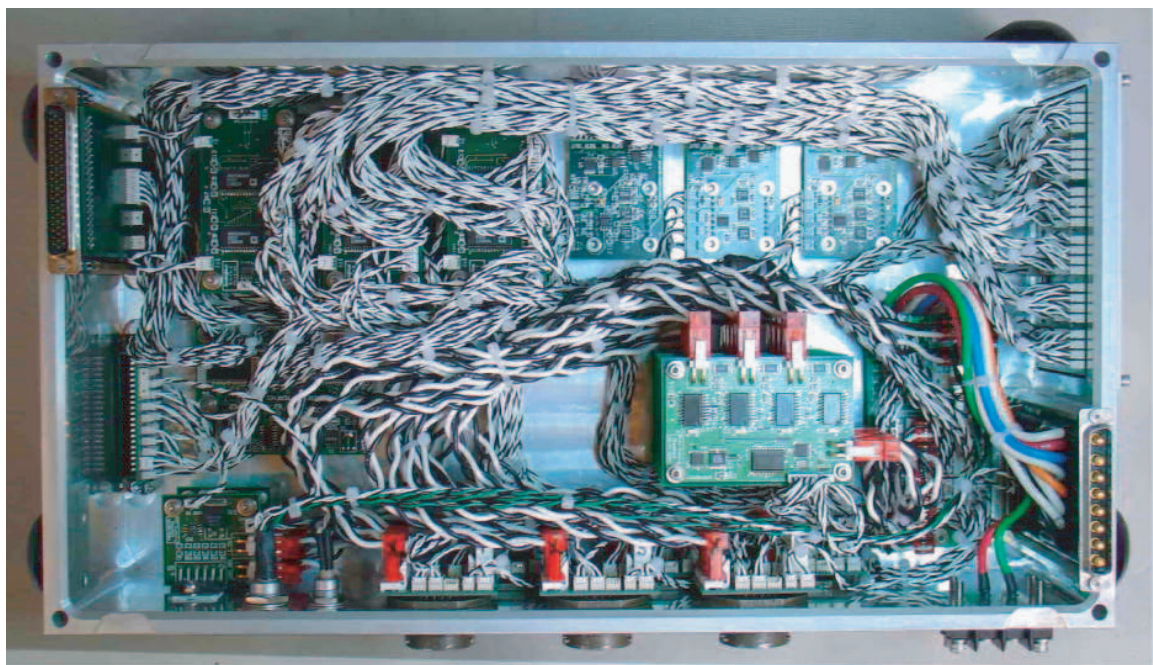


Figure B.2: Sensor frame

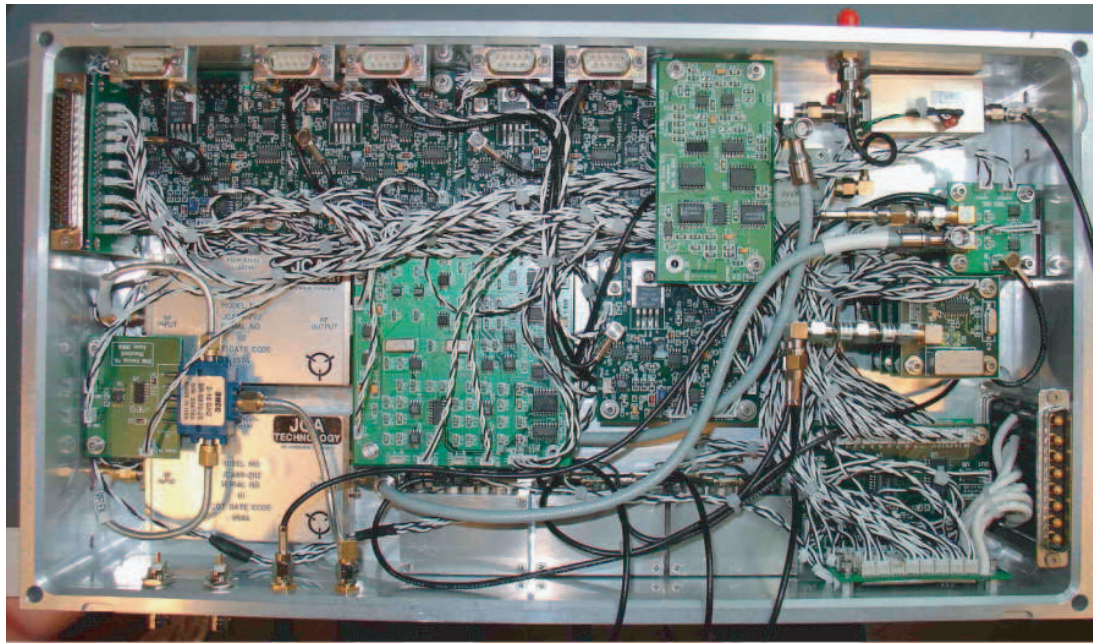


Figure B.3: Master electronics frame

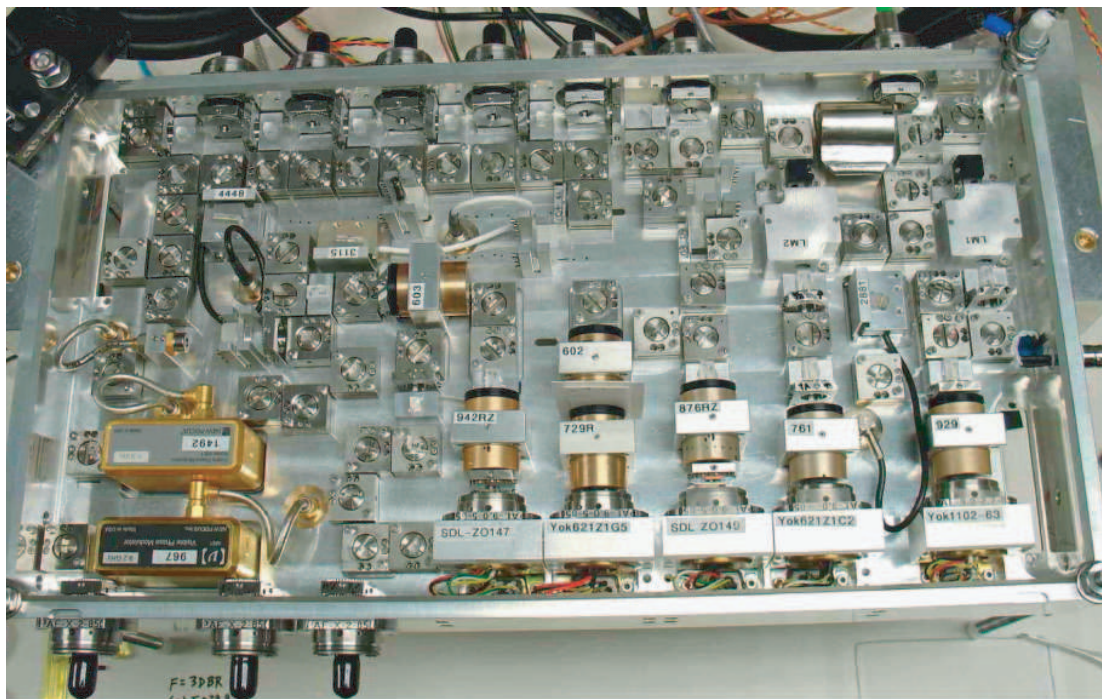


Figure B.4: Master laser frame

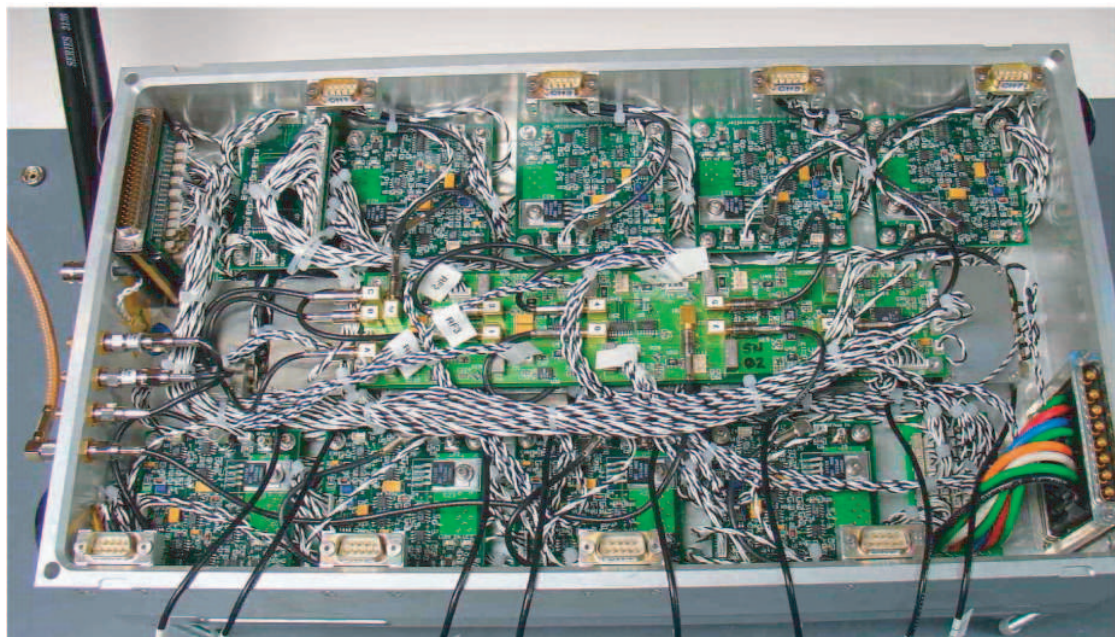


Figure B.5: Amplifier electronics frame

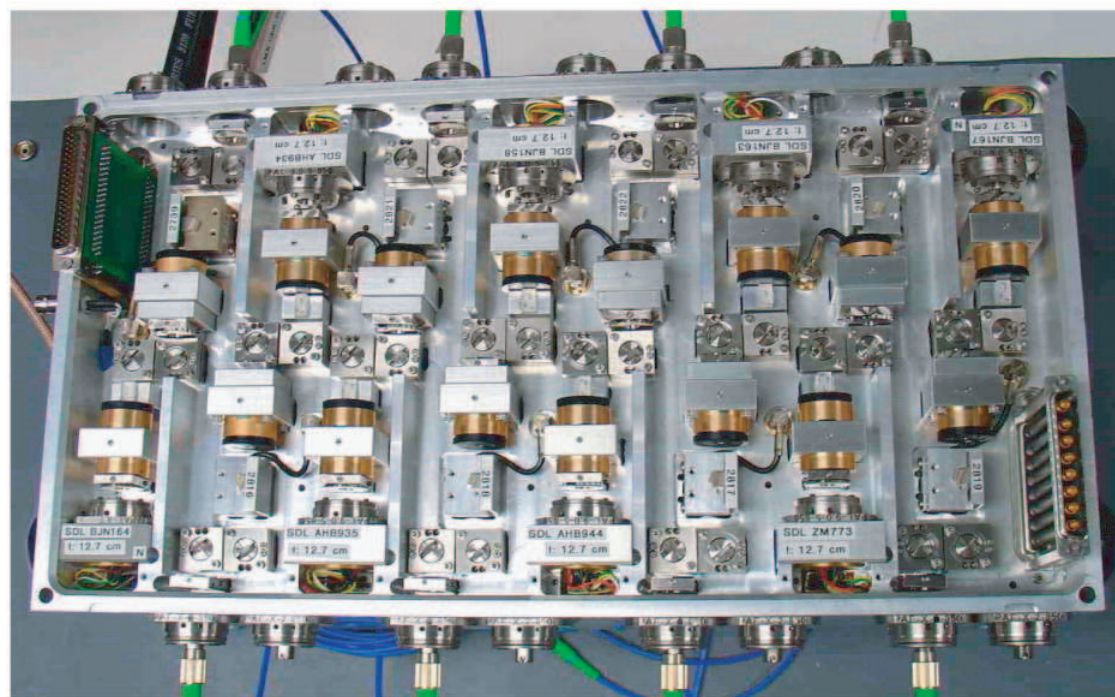


Figure B.6: Amplifier laser frame

Bibliography

- [1] Christopher Jekeli. *Inertial Navigation Systems with Geodetic Applications*. Walter de Gruyter, New York, 2000.
- [2] L. L. Nettleton. *Geophysical prospecting for oil*. New York and London, McGraw-Hill book company, inc., 1940.
- [3] G. B. Arfken and H. J. Weber. *Mathematical Methods for Physicists*. Academic Press, 4th edition, 1995.
- [4] A. H. Zorn. A merging of system technologies: All-accelerometer inertial navigation and gravity gradiometry. *IEEE Position Location and Navigation Symposium (PLANS)*, 2002.
- [5] Donald C. Barton. Eötvös torsion balance. *Physics*, 3(1):29–38, 1932.
- [6] R. V. Eötvös. *Mathematische und naturwissenschaftliche berichte und ungarn*, 8:65, 1891.
- [7] R. v. Eötvös, D. Pekár, and E. Fekete. *Annalen der Physik (Leipzig)*, 68:11–66, 1922.
- [8] Ephraim Fischbach, Daniel Sudarsky, Aaron Szafer, Carrick Talmadge, and S. H. Aronson. Reanalysis of the Eötvös experiment. *Phys. Rev. Lett.*, 56(1):3–6, Jan 1986.
- [9] R. E. Bell and R. O. Hansen. The rise and fall of early oil field technology: The torsion balance gradiometer. *The Leading Edge*, 17:81, 1998.

- [10] CIA – *The World FactBook*. <https://www.cia.gov/library/publications/the-world-factbook>, 2007.
- [11] E. W. Shaw. Possibility of using gravity anomalies in the search for salt-dome oil and gas pools. *Science*, 46:553, 1917.
- [12] A. J. Romaides, J. C. Battis, R. W. Sands, A. Zorn, D. O. Benson, and D. J. DiFrancesco. A comparison of gravimetric techniques for measuring subsurface void signals. *Journal of Physics D-Applied Physics*, 34(3):433–443, 2001.
- [13] J B Lee, D B Boggs, M A Downey, R A M Maddever, R J Turner, and M H Dransfield. First test survey results from the FALCON helicopter-borne air-borne gravity gradiometer system. In *Australian Earth Sciences Convention*, Melbourne, Australia, 2006.
- [14] C. Jekeli. Precision free-inertial navigation with gravity compensation by an onboard gradiometer. *Journal of Guidance Control and Dynamics*, 29(3):704–713, 2006.
- [15] C. Jekeli. A review of gravity gradiometer survey system data analyses. *Geophysics*, 58:508–514, 1993.
- [16] M. Ryan. Memphis uses gravity to reach new navigational heights. *Undersea Warfare*, 1:22–3, 1998.
- [17] H. J. Paik, V. Prieto, and M. V. Moody. Probing extra dimensions using a superconducting accelerometer. *Journal of the Korean Physical Society*, 45:S104–S109, 2004.
- [18] M.V. Moody and H.J. Paik. Gauss's law test of gravity at short range. *Phys. Rev. Lett.*, 70:1195–8, 1993.
- [19] H.J. Paik. Superconducting accelerometry: its principles and applications. *Class. Quantum Grav.*, 11:A133–A144, 1994.

- [20] J. M. Goodkind. The superconducting gravimeter. *Review of Scientific Instruments*, 70(11):4131–4152, 1999.
- [21] F. J. Vankann, M. J. Buckingham, C. Edwards, and R. Matthews. Performance of a superconducting gravity gradiometer. *Physica B*, 194:61–62, 1994.
- [22] T. M. Niebauer, G. S. Sasagawa, J. E. Faller, R. Hilt, and F. Klopping. A new generation of absolute gravimeters. *Metrologia*, 32(3):159–180, 1995.
- [23] J. M. Brown, T. M. Niebauer, F. J. Klopping, and A. T. Herring. A new fiber optic gradiometer for 4-D absolute differential gravity. *Geophysical Research Letters*, 27(1):33–36, 2000.
- [24] J. M. McGuirk, G. T. Foster, J. B. Fixler, M. J. Snadden, and M. A. Kasevich. Sensitive absolute-gravity gradiometry using atom interferometry. *Physical Review A*, 65(3):14, 2002.
- [25] D. S. Durfee, Y. K. Shaham, and M. A. Kasevich. Long-term stability of an area-reversible atom-interferometer Sagnac gyroscope. *Physical Review Letters*, 97(24):4, 2006.
- [26] J. B. Fixler, G. T. Foster, J. M. McGuirk, and M. A. Kasevich. Atom interferometer measurement of the Newtonian constant of gravity. *Science*, 315(5808):74–77, 2007.
- [27] S. Dimopoulos, P. W. Graham, J. M. Hogan, and M. A. Kasevich. Testing general relativity with atom interferometry. *Physical Review Letters*, 98(11):4, 2007.
- [28] D. Kleppner. A short history of atomic physics in the twentieth century. *Reviews of Modern Physics*, 71(2):S78–S84, 1999.
- [29] J. P. Gordon, H. J. Zeiger, and C. H. Townes. Molecular microwave oscillator and new hyperfine structure in the microwave spectrum of NH₃. *Physical Review*, 95(1):282–284, 1954.

- [30] N. F. Ramsey. A molecular beam resonance method with separated oscillating fields. *Physical Review*, 78(6):695–699, 1950.
- [31] E. L. Raab, M. Prentiss, A. Cable, S. Chu, and D. E. Pritchard. Trapping of neutral Sodium atoms with radiation pressure. *Physical Review Letters*, 59(23):2631–2634, 1987.
- [32] M. H. Anderson, J. R. Ensher, M. R. Matthews, C. E. Wieman, and E. A. Cornell. Observation of bose-einstein condensation in a dilute atomic vapor. *Science*, 269(5221):198–201, 1995.
- [33] S. Bize, P. Laurent, M. Abgrall, H. Marion, I. Maksimovic, L. Cacciapuoti, J. Grunert, C. Vian, F. P. dos Santos, P. Rosenbusch, P. Lemonde, G. Santarelli, P. Wolf, A. Clairon, A. Luiten, M. Tobar, and C. Salomon. Cold atom clocks and applications. *Journal of Physics B-Atomic Molecular and Optical Physics*, 38(9):S449–S468, 2005.
- [34] J. J. Slosser and P. Meystre. Resource letter: CQO-1: Coherence in quantum optics. *American Journal of Physics*, 65(4):275–286, 1997.
- [35] P. J. Mohr, B. N. Taylor, and D. B. Newell. The fundamental physical constants. *Physics Today*, 60(7):52–55, 2007.
- [36] A. P. Mills. Proposed null experiment to test the inverse square nature of gravitation. *General Relativity and Gravitation*, 11(1):1–11, 1979.
- [37] G. T. Gillies. The newtonian gravitational constant: Recent measurements and related studies. *Reports on Progress in Physics*, 60(2):151–225, 1997.
- [38] P. J. Mohr and B. N. Taylor. CODATA recommended values of the fundamental physical constants: 1998. *Reviews of Modern Physics*, 72(2):351–495, 2000.
- [39] E. R. Cohen and B. N. Taylor. The 1986 CODATA recommended values of the fundamental physical constants. *Journal of Physical and Chemical Reference Data*, 17(4):1795–1803, 1988.

- [40] K. Kazuaki. Anelasticity in g experiments. *Meas. Sci. Technol.*, 10:435–438, 1999.
- [41] E. Fischbach and C.L. Talmadge. *The Search for Non-Newtonian Gravity*. Springer-Verlag, New York, 1999.
- [42] D. J. Kapner, T. S. Cook, E. G. Adelberger, J. H. Gundlach, B. R. Heckel, C. D. Hoyle, and H. E. Swanson. Tests of the gravitational inverse-square law below the dark-energy length scale. *Physical Review Letters*, 98(2):4, 2007.
- [43] E.G. Adelberger, B.R. Heckel, and A.E. Nelson. Tests of the gravitational inverse-square law. *Annual Review of Nuclear and Particle Science*, 53(1):77–121, 2003.
- [44] Private communication with Peter Graham.
- [45] S. Wajima, M. Kasai, and T. Futamase. Post-Newtonian effects of gravity on quantum interferometry. *Physical Review D*, 55(4):1964–1970, 1997.
- [46] C. J. Borda. Quantum theory of atom-wave beam splitters and application to multidimensional atomic gravito-inertial sensors. *General Relativity and Gravitation*, 36(3):475–502, 2004.
- [47] M. P. Bradley, J. V. Porto, S. Rainville, J. K. Thompson, and D. E. Pritchard. Penning trap measurements of the masses cog Cs-133, Rb-87, Rb-85, and Na-23 with uncertainties $\ll 0.2$ ppb. *Physical Review Letters*, 83(22):4510–4513, 1999.
- [48] G. W. Biedermann, X. Wu, L. Deslauriers, K. Takase, and M. A. Kasevich. Low-noise simultaneous fluorescence detection of two atomic states. *Optics Lett.*, submitted May 2007.
- [49] M. Kasevich and S. Chu. Measurement of the gravitational acceleration of an atom with a light-pulse atom interferometer. *Appl. Phys. B*, 54:321–332, 1992.
- [50] K. Moler, D. S. Weiss, M. Kasevich, and S. Chu. Theoretical analysis of velocity-selective Raman transitions. *Phys. Rev. A*, 45:342–348, 1992.

- [51] P. R. Berman, editor. *Atom Interferometry*. Academic Press, San Diego, CA, 1997.
- [52] M. Kasevich, D. S. Weiss, E. Riis, K. Moler, S. Kasapi, and S. Chu. Atomic velocity selection using stimulated Raman transitions. *Phys. Rev. Lett.*, 66:2297–2300, 1991.
- [53] K. Bongs, R. Launay, and M. A. Kasevich. High-order inertial phase shifts for time-domain atom interferometers. *Applied Physics B-Lasers and Optics*, 84(4):599–602, 2006.
- [54] R.P. Feynman. *Quantum Mechanics and Path Integrals*. McGraw-Hill, New York, 1965.
- [55] A.L. Fetter and J.D. Walecka. *Theoretical Mechanics of Particles and Continua*. Addison Wesley, 1980.
- [56] P. Storey and C. Cohenannoudji. The Feynman path-integral approach to atomic interferometry - a tutorial. *Journal De Physique Ii*, 4(11):1999–2027, 1994.
- [57] A. Peters. *High Precision Gravity Measurements using Atom Interferometry*. PhD thesis, Stanford University, 1998.
- [58] K. Takase. *Precision Rotation Measurements with a Mobile Atom Gyroscope*. PhD thesis, Stanford University, 2008.
- [59] J. M. McGuirk, M. J. Snadden, and M. A. Kasevich. Large area light-pulse atom interferometry. *Physical Review Letters*, 85(21):4498–4501, 2000.
- [60] Martin Weitz, Brenton C. Young, and Steven Chu. Atomic interferometer based on adiabatic population transfer. *Phys. Rev. Lett.*, 73(19):2563–2566, Nov 1994.
- [61] J H Denschlag, J E Simsarian, H Häffner, C McKenzie, A Browaeys, D Cho, K Helmerson, S L Rolston, and W D Phillips. A Bose-Einstein condensate in an optical lattice. *Journal of Physics B: Atomic, Molecular and Optical Physics*, 35(14):3095–3110, 2002.

- [62] G. Santarelli, Ph. Laurent, P. Lemonde, A. Clairon, A. G. Mann, S. Chang, A. N. Luiten, and C. Salomon. Quantum projection noise in an atomic fountain: a high stability Cesium frequency standard. *Phys. Rev. Lett.*, 82:4619, 1999.
- [63] H. J. Metcalf and P. van der Straten. *Laser Cooling and Trapping*. Springer-Verlag, New York, 1999.
- [64] C. S. Adams and E. Riis. Laser cooling and trapping of neutral atoms. *Progress in Quantum Electronics*, 21(1):1–79, 1997.
- [65] J. Schoser, A. Batar, R. Low, V. Schweikhard, A. Grabowski, Y. B. Ovchinnikov, and T. Pfau. Intense source of cold Rb atoms from a pure two-dimensional magneto-optical trap. *Physical Review A*, 66(2):10, 2002.
- [66] S. Chu, L. Hollberg, J. E. Bjorkholm, A. Cable, and A. Ashkin. 3-dimensional viscous confinement and cooling of atoms by resonance radiation pressure. *Physical Review Letters*, 55(1):48–51, 1985.
- [67] P. D. Lett, W. D. Phillips, S. L. Rolston, C. E. Tanner, R. N. Watts, and C. I. Westbrook. Optical molasses. *Journal of the Optical Society of America B-Optical Physics*, 6(11):2084–2107, 1989.
- [68] J. H. Shirley. Modulation transfer processes in optical heterodyne saturation spectroscopy. *Optics Letters*, 7(11):537–539, 1982.
- [69] M. A. Kasevich, E. Riis, S Chu, and R G DeVoe. rf spectroscopy in an atomic fountain. *Phys. Rev. Lett.*, 63(6):612–615, Aug 1989.
- [70] J. Dalibard and C. Cohen-annoudji. Laser cooling below the Doppler limit by polarization gradients - simple theoretical-models. *Journal of the Optical Society of America B-Optical Physics*, 6(11):2023–2045, 1989.
- [71] N. D. Bhaskar and C. M. Kahla. Cesium gettering by graphite - improvement in the gettering efficiency. *Ieee Transactions on Ultrasonics Ferroelectrics and Frequency Control*, 37(5):355–358, 1990.

- [72] A. E. Rodriguez, W. L. Morgan, K. J. Touryan, W. M. Moeny, and T. H. Martin. An air breakdown kinetic-model. *Journal of Applied Physics*, 70(4):2015–2022, 1991.
- [73] Private communication with Chetan Mahadeswaraswamy.
- [74] R. W. Fox, C. W. Oates, and L W Hollberg. *Cavity-Enhanced Spectroscopies: Experimental Methods in the Physical Sciences*, chapter Stabilizing diode lasers to high-finesse cavities, pages 1–46. Academic Press, 2002.
- [75] M. J. Lawrence, B. Willke, M. E. Husman, E. K. Gustafson, and R. L. Byer. Dynamic response of a Fabry-Perot interferometer. *Journal of the Optical Society of America B-Optical Physics*, 16(4):523–532, 1999.
- [76] J.M. McGuirk. *High Precision Absolutte Gravity Gradiometry with Atom Interferometry*. PhD thesis, Stanford University, 2001.
- [77] A. Peters, K. Y. Chung, and S. Chu. High-precision gravity measurements using atom interferometry. *Metrologia*, 38(1):25–61, 2001.
- [78] W. M. Itano, J. C. Bergquist, J. J. Bollinger, J. M. Gilligan, D. J. Heinzen, F. L. Moore, M. G. Raizen, and D. J. Wineland. Quantum projection noise - population fluctuations in 2-level systems. *Physical Review A*, 47(5):3554–3570, 1993.
- [79] J. M. McGuirk, G. T. Foster, J. B. Fixler, and M. A. Kasevich. Low-noise detection of ultracold atoms. *Optics Letters*, 26(6):364–366, 2001.
- [80] N. Ramsey. *Molecular Beam Spectroscopy*. The Clarendon Press, 1956.
- [81] S. Bize, Y. Sortais, P. Lemonde, S. Zhang, P. Laurent, G. Santarelli, C. Salomon, and A. Clairon. Interrogation oscillator noise rejection in the comparison of atomic fountains. *IEEE Trans. Ultrason., Ferroelect., Freq. Contr.*, 47:1253, 2000.

- [82] G. T. Foster, J. B. Fixler, J. M. McGuirk, and M. A. Kasevich. Method of phase extraction between coupled atom interferometers using ellipse-specific fitting. *Optics Letters*, 27(11):951–953, 2002.
- [83] John K. Stockton, Xianan Wu, and Mark A. Kasevich. Bayesian estimation of differential interferometer phase. *Physical Review A (Atomic, Molecular, and Optical Physics)*, 76(3):033613, 2007.
- [84] N. Bobroff. Recent advances in displacement measuring interferometry. *Meas. Sci. Technol.*, 4:907–926, 1993.
- [85] J. Le Gouet, P. Cheinet, J. Kim, D. Holleville, A. Clairon, A. Landragin, and F. P. Dos Santos. Influence of lasers propagation delay on the sensitivity of atom interferometers. *European Physical Journal D*, 44(3):419–425, 2007.
- [86] A. Bertoldi, G. Lamporesi, L. Cacciapuoti, M. de Angelis, M. Fattori, T. Petelski, A. Peters, M. Prevedelli, J. Stuhler, and G. M. Tino. Atom interferometry gravity-gradiometer for the determination of the Newtonian gravitational constant G. *European Physical Journal D*, 40(2):271–279, 2006.
- [87] P. W. Graham, M. Kasevich, and J. G. Whacker. Measuring sub-gravitational strength forces from 10 μm to 100 m with atom interferometry. 2007.
- [88] B. Guinot and E. F. Arias. Atomic time-keeping from 1955 to the present. *Metrologia*, 42(3):S20–S30, 2005.
- [89] T. P. Heavner, S. R. Jefferts, E. A. Donley, J. H. Shirley, and T. E. Parker. NIST-F1: recent improvements and accuracy evaluations. *Metrologia*, 42(5):411–422, 2005.
- [90] A. Quessada, R. P. Kovacich, I. Courtillot, A. Clairon, G. Santarelli, and P. Lemonde. The Dick effect for an optical frequency standard. *J. Opt. B: Quant. Semiclass. Opt.*, 5:S150, 2003.

- [91] L. Ma, P. Jungner, J. Ye, and J. L. Hall. Delivering the same optical frequency at two places: accurate cancellation of phase noise introduced by an optical fiber or other time-varying path. *Optics Lett.*, 19:1777, 1994.
- [92] U. Sterr, C. Degenhardt, H. Stoehr, Ch. Lisdat, H. Schnatza, J. Helmcke, F. Riehle, G. Wilpers, Ch. Oates, and L. Hollberg. The optical Calcium frequency standards of PTB and NIST. *C. R. Physique*, 5:845–855, 2004.
- [93] R. Wynands and S. Weyers. Atomic fountain clocks. *Metrologia*, 42(3):S64–S79, 2005.
- [94] G. J. Dick, J. D. Prestage, C. A. Greenhall, and L. Maleki. Local oscillator induced instabilities in trapped ion frequency standards. In *Proc. 19th Precise Time and Time Interval (PTTI) Applications and Planning Meeting*, pages 133–147, 1987.
- [95] G. Santarelli, C. Audoin, A. Makdissi, Ph. Laurent, G. J. Dick, and A. Clairon. Frequency stability degradation of an oscillator slaved to a periodically interrogated atomic resonator. *IEEE Trans Ultra. Ferro. Elec Freq. Contr.*, 45:887, 1998.
- [96] P. Gill. Optical frequency standards. *Metrologia*, 42(3):S125–S137, 2005.
- [97] W. H. Oskay, S. A. Diddams, E. A. Donley, T. M. Fortier, T. P. Heavner, L. Hollberg, W. M. Itano, S. R. Jefferts, M. J. Delaney, K. Kim, F. Levi, T. E. Parker, and J. C. Bergquist. Single-atom optical clock with high accuracy. *Physical Review Letters*, 97(2):4, 2006.
- [98] J. Guéna, G. Dudle, and P. Thomann. An experimental study of intermodulation effects in an atomic fountain frequency standard. *Eur. Phys. J. Appl. Phys.*, 38:183–189, 2007.
- [99] A. Joyet, G. Milet, G. Dudle, and P. Thomann. Theoretical study of the Dick effect in a continuously operated Ramsey resonator. *IEEE Trans. Instrum. Meas.*, 50:150–155, 2001.

- [100] G. J. Dick, J. D. Prestage, C. A. Greenhall, and L. Maleki. Local oscillator induced degradation of medium-term stability in passive atomic frequency standards. In *its The 22nd Annual Precise Time and Time Interval (PTTI) Applications and Planning Meeting p 487-508 (SEE N91-25755 17-70)*, pages 487–508, May 1990.
- [101] D.W. Allan, J.H. Shoaf, , and D. Halford. *Characterization of Frequency Stability*, chapter 8 ”Statistics of Time and Frequency Data Analysis”, pages 151–204. IEEE Trans. on Instrumentation and Measurement, 1973.
- [102] P. J. Mohr and B. N. Taylor. CODATA recommended values of the fundamental physical constants: 2002. *Reviews of Modern Physics*, 77(1):1–107, 2005.
- [103] *CRC Handbook of Chemistry and Physics*. CRC Press, Boca Raton, 78th edition, 1997.
- [104] V. Gerginov, C. E. Tanner, S. Diddams, A. Bartels, and L. Hollberg. Optical frequency measurements of 6s S-2(1/2)-6p P-2(3/2) transition in a Cs-133 atomic beam using a femtosecond laser frequency comb. *Physical Review A*, 70(4):8, 2004.
- [105] R. J. Rafac, C. E. Tanner, A. E. Livingston, K. W. Kukla, H. G. Berry, and C. A. Kurtz. Precision lifetime measurements of the 6p P-2(1/2,3/2) states in atomic Cesium. *Physical Review A*, 50(3):R1976–R1979, 1994.